MONTE CARLO/FOKKER-PLANCK SIMULATIONS OF ACCRETION PHENOMENA AND OPTICAL SPECTRA OF BL LACERTAE OBJECTS

A dissertation presented to
the faculty of
the College of Arts and Sciences

In partial fulfillment
of the requirements for the degree
Doctor of Philosophy

Justin D. Finke

August 2007

This dissertation entitled

MONTE CARLO/FOKKER-PLANCK SIMULATIONS OF ACCRETION PHENOMENA AND OPTICAL SPECTRA OF BL LACERTAE OBJECTS

by

JUSTIN D. FINKE

has been approved for
the Department of Physics and Astronomy
and the College of Arts and Sciences by

Markus Böttcher
Assistant Professor of Physics and Astronomy

Benjamin M. Ogles
Dean, College of Arts and Sciences

FINKE, JUSTIN, Ph.D., August 2007, Physics and Astronomy

Monte Carlo/Fokker-Planck simulations of Accretion Phenomena and Optical Spectra of BL Lacertae Objects (137 pp.)

Director of Dissertation: Markus Böttcher

A time-dependent two-dimensional Monte Carlo/Fokker-Planck (MC/FP) code, which uses a Monte Carlo technique for Compton scattering and radiative transport, and a Fokker-Planck technique for electron evolution, has been fully parallelized with the Message Passing Interface (MPI) to take advantage of computers with multiple processors and decrease running time. This code has been successfully applied to the following astrophysically relevant scenario: it was coupled with the line transfer program XSTAR to simulate multiple Compton reflections within photon bubbles, making predictions for their X-ray spectral features. Predictions include a spectral feature at ~ 9 keV and hard power-law tails similar to those observed in X-ray binaries in the very high state.

This dissertation also includes the results of an observational project to determine the redshifts of six BL Lac objects, (i.e., galaxies dominated by radiation from the jets emerging from their central black holes) with the 2.4 m Hiltner telescope at the MDM observatory on Kitt Peak, Arizona. The redshifts of these objects have been constrained in agreement with previous estimates in most cases; however, in one case (W Comae) the constraints and previous estimates were not in agreement.

Approved: ____

Markus Böttcher

Assistant Professor of Physics and Astronomy

Preface

§ 2.3.3 has been published in *Publications of the Astronomical Society of the Pacific* in a slightly different form (Finke and Böttcher 2005). Parts of Chapters 3 and 4 have been submitted for publication to the *Astrophysical Journal*. Chapter 5 will soon be submitted for publication to a refereed journal.

Acknowledgments

First and foremost I would like to thank Prof. Markus Böttcher, my dissertation advisor, for being a kind, wonderful and patient advisor, always willing to answer my questions, no matter how foolish. He has, of course, been a great deal of help at all stages of this project. Prof. Joe Shields has also helped me a great deal in many ways, in particular with the observing project described in Chapter 5, for which I am extremely grateful. I would like to thank my fellow Ohio University graduate students, in particular, Dr. Steven Diehl, Dr. Swati Gupta, and Manasvita Joshi, for their friendship and help on various astronomy– and computer–related problems. I greatly appreciate the help I have received from Don Roth for all things relating to computers and their smooth operation. I am grateful to all members of the dissertation committee: Markus Böttcher, Joe Shields, Brian McNamara and Keith Milam, for taking time out of their busy schedules. Prof. Brian McNamara, in particular, has traveled great distances from foreign lands to come to my defense.

This work was partially supported by an allocation of computing time from the Ohio Supercomputer Center (OSC) via grant PHS0256-1. Simulations were run on the OSC Pentium 4 Cluster in Columbus, Ohio, and the Cray X-1 machine in Springfield, Ohio. I have been funded by Research Assistantships from NASA through *XMM-Newton* GO grant no. NNG04GI50G and *INTEGRAL* theory grant NNG05GK59G, as well as NRL Contract No. N00173-07-P-2006. But mostly I have been supported through Teaching Assistantships from the Ohio University Department of Physics and Astronomy.

Table of Contents

Page

List of Figures

List of Tables

CHAPTER 1

Introduction

1.1 Accreting Black Holes

Black holes (BHs)—spherical regions of space where spacetime is curved to the extent that light cannot escape—may be viewed when matter is accreted onto these compact objects. Before the matter crosses the BH's event horizon it releases part of its gravitational potential energy as electromagnetic radiation. BHs may be formed as the remains of the collapse of massive stars which explode as supernovae. Such BHs have masses of typically a few $M_\odot$. If the object is part of a binary system, it may accrete matter from its companion star, leading to objects known as X-ray binaries (XRBs). Supermassive BHs—with masses greater than $\sim 10^6 M_\odot$—are found at the center of most, if not all, large galaxies, where they accrete matter from the surrounding galaxy. These objects are known as Active Galactic Nuclei (AGN). Accretion usually takes the form of an accretion disk around the black hole (Shakura and Sunyaev 1973), which, in XRBs, may be driven by one of two mechanisms: the stellar wind of the high mass companion star, or the companion star's outer layers overflowing its Roche lobe. According to General Relativity, stable orbits around black holes can only exist above a certain radius that is directly proportional to the black hole's mass. The disk emits thermal radiation with a temperature that gets cooler farther away from the central black hole; thus, supermassive black hole disks, which have an innermost stable circular orbit much farther from the compact object, accrete at cooler temperatures and emit thermal radiation in the ultraviolet, while XRB disks accrete at higher temperatures and emit thermal radiation in the soft X-rays. Both types of sources exhibit hard X-ray nonthermal power-law emission, the origin of which is not entirely clear, but might be due to Compton up-scattering of thermal disk radiation (see below).

Often, relativistic outflows (jets) are observed from accreting compact objects, which are presumably perpendicular to the accretion disk. AGN with jets are known as quasars, and, analogously, XRBs with jets are known as microquasars. An AGN with the jet pointing along our line of sight, so that its emission dominates over its host galaxy's, is known as a blazar. Blazars are sub-divided into two groups: BL Lacertae objects, which have weak, if any absorption and emission lines in their optical spectra; and Flat Spectrum Radio Quasars (FSRQs), which have stronger absorption and emission features. Both tend to radiate across the entire electromagnetic spectrum, from radio to gamma-ray, and exhibit many types of variability.

XRBs have been observed to have X-ray spectra consisting of two distinct components. One is a multicolor disk blackbody component (MCDBB) from a geometrically thin, optically thick accretion disk. Another is a hard power-law tail from a higher temperature, optically thin Comptonizing plasma (or corona). It is thought that the Comptonizing plasma Compton up-scatters photons from the disk to create the power-law component (see § 1.2). Sometimes a reflection component is also observed, usually in the form of an Fe Kα fluorescence feature at ~ 6 keV. This is believed to be created by nonthermal coronal emission reflected off the disk. The geometry of the system is a matter of some debate. XRBs have been observed in at least two spectral states (for a recent review of XRB spectral states, see Zdziarski and Gierliński 2004), distinguished by the relative strengths of the above-mentioned components. The "low/hard" state is distinguished by a lower luminosity and a spectrum dominated by the hard power-law component with a cut-off at ~ 100—200 keV. This state is also associated with jets. XRBs such as Cyg X-1 or GRS 1915+105 seem to spend most of their time in this state. The "high/soft" state is characterized by a higher luminosity and a stronger soft blackbody component relative to the hard power-law. As yet, no high-energy cutoff has been observed in this state. There are also several less well–defined, ambiguous states—e.g., the "intermediate state" and/or the "very high state". These are sometimes considered to be separate states and sometimes considered to be the same state, but in any case, they are observed in transitions between the low/hard and high/soft states and have a hardness in between the two.

The spectral properties of XRBs are usually explained in terms of the source's geometry. The high/soft state occurs when the disk extends down to the innermost stable circular orbit, and the tenuous Comptonizing corona sandwiches the disk. The low/hard state is thought to occur when the inner disk is truncated at a larger radius, and the inner radiatively inefficient accretion flow is the hot Comptonizing plasma

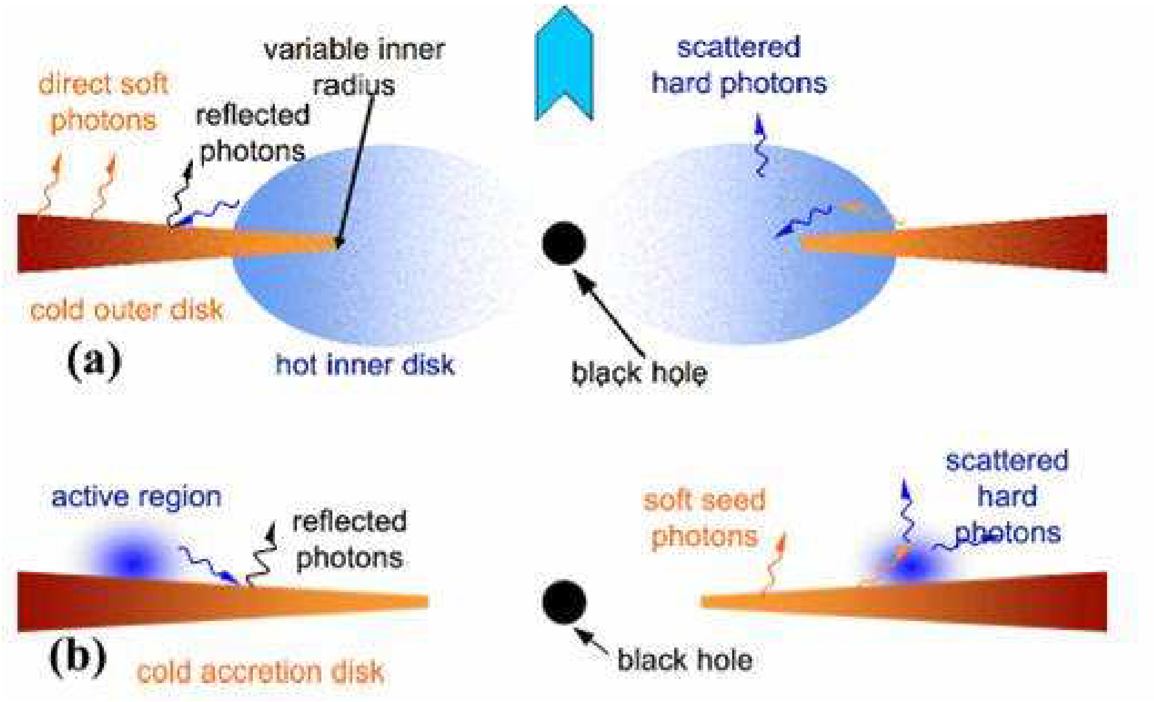

Figure 1.1: Illustration of (a) the low/hard state and (b) the high/soft state in XRBs. This figure was taken from Zdziarski and Gierliński (2004).

(e.g., an advection dominated accretion flow, or ADAF). The geometry of these states is illustrated in Fig. 1.1.

Ultraluminous X-ray Sources (ULXs) are thought to be XRBs with luminosities above the Eddington limit (see § 1.5) for a black hole of a few solar masses; they hence have luminosities in between those of XRBs and AGN. I describe ULXs in some detail in Chapter 3.

1.2 Compton Scattering

One of the most important radiation mechanisms for accreting black holes is that of Compton scattering. The full relativistic total cross-section for Compton scattering–where a photon is scattered off of an electron–was first found by Klein and Nishina (1929) to be (here, as everywhere in this dissertation, I use Gaussian units):

$$\sigma_{KN} = \frac{\pi e^4}{m_e^2 c^4 x} \left\{ \left[1 - \frac{2(x+1)}{x^2} \right] \ln(2x+1) + \frac{1}{2} + \frac{4}{x} - \frac{1}{2(2x+1)^2} \right\} \tag{1.1}$$

where e is the fundamental charge, m_e is the mass of the electron, c is the speed of light, and x is the incident photon energy in the electron's rest frame in terms of the electron rest energy ($x = E/m_e c^2$). For the nonrelativistic case ($x \ll 1$), this reduces to the Thomson cross section:

$$\sigma_T = \frac{8\pi e^4}{3 m_e^2 c^4}, \tag{1.2}$$

while in the ultrarelativistic limit ($x \gg 1$), the cross-section drops off as $\sigma_{KN} \propto x^{-1} ln(2x)$.

When the photon's energy is less than that of the electron, the photon gains energy from the electron. This is known as inverse Compton scattering or Compton up–scattering (because the photons are "scattered up" to higher energies). Inverse Compton Scattering occurs in many astrophysical objects. Scattering of photons from the cosmic microwave background by hot gas in galaxy clusters is known as the Sunyaev-Zel'dovich effect (Sunyaev and Zeldovich 1970), which can be used to measure the value of the Hubble parameter, H_0. Inverse Compton scattering of solar photosphere photons by the solar corona produces the majority of the light seen from the corona. Analogously, inverse Compton scattering by coronae sandwiching accretion disks have been proposed to explain the hard X-ray power-laws from XRBs and AGN.

Inverse Compton scattering by a nonrelativistic thermal electron distribution was studied by Kompaneets (1957), leading to the Kompaneets equation which cannot, in general, be solved analytically, especially for non-isotropic radiation sources. Alternatively, inverse Compton scattering off of a high temperature, relativistic plasma can be handled by a Monte Carlo numerical method developed by Pozdniakov et al. (1983) and Canfield et al. (1987), and described in § 2.3.1.

1.3 Radiation and Acceleration Mechanisms

Other radiation mechanisms important in relativistic plasmas include thermal synchrotron and cyclotron radiation and thermal Bremsstrahlung. Electrons in these plasmas may be accelerated by plasma wave turbulence, by interacting with the above-mentioned radiation mechanisms, or through Coulomb interactions. Of relevance to this dissertation are interactions between radiation and an electron distribution described by a thermal component (a relativistic Maxwell-Boltzmann distribution) and a nonthermal power-law tail. The relativistic Maxwell-Boltzmann distribution is:

$$n(\gamma) = \frac{n_e}{\Theta_e K_2(1/\Theta_e)} \beta\gamma^2 \exp[-\gamma/\Theta_e] \tag{1.3}$$

where n_e is the electron density, $\Theta_e = kT_e/m_e c^2$ is the electron temperature in units of the electron rest energy, and K_2 is the modified Bessel function of order 2.

Synchrotron radiation is created by relativistic electrons spiraling around magnetic field lines. If the electrons are described by a nonthermal power-law with index p ($n_e \propto \gamma^{-p}$), then the synchrotron radiation will have the form of a power-law with $F \propto \nu^{-(p-1)/2}$. However, some of the synchrotron radiation will be absorbed by the electrons revolving around the magnetic field lines (analogous to bound-bound absorption in atoms) in a process known as synchrotron self-absorption (SSA). In this case, there will often be a low-energy power-law $F \propto \nu^{5/2}$ (Rybicki and Lightman 1979).

Cyclotron radiation is the nonrelativistic analog to synchrotron radiation. For the purposes of this dissertation, cyclotron will be considered to be from a thermal particle distribution. Cyclotron radiation takes the form of several broadened delta functions, which have frequencies that are integer multiples of the cyclotron frequency,

$$\omega_c = \frac{eB}{m_e c}. \tag{1.4}$$

For a detailed discussion, see, e.g., Mahadevan et al. (1996).

Bremsstrahlung is radiation produced by inelastic scattering between free electrons and atomic nuclei (ions). Thermal Bremsstrahlung—where the electrons and ions make up a thermal distribution—leads to radiation of the form $F \propto g(\nu)\exp(-h\nu/kT_e)$ where $g(\nu)$ is the Gaunt factor, which is weakly dependent on photon frequency (Rybicki and Lightman 1979).

Coulomb interactions between electrons and atomic nuclei (e-p) and electrons and other electrons (e-e, also known as Møller scattering) are the primary way energy is exchanged between particles in dense plasmas.

Alfv́en waves are created by electromagnetic turbulence—i.e., time-varying perturbations to a electromagnetic field. They propagate in the direction of a magnetic field. Electrons are accelerated perpendicular to the magnetic field, accelerating particles to a nonthermal, high-energy power-law distribution.

1.4 X-ray Telescopes

This dissertation will deal primarily with X-ray and, to a lesser extent, γ-ray emission from accreting astrophysical objects. X-rays are observed, naturally enough, with X-ray telescopes. In this section, I will briefly discuss X-ray telescopes which I will mention throughout this dissertation. X-rays do not penetrate the Earth's atmosphere, and so all X-ray astronomy has been done with high-altitude instruments in balloons and early rockets at first, and with satellites orbiting the Earth more recently. Most of the following information is from the Goddard Space Flight Center website (`http://imagine.gsfc.nasa.gov/docs/sats_n_data/xray_missions.html`).

The *Advanced Satellite for Cosmology and Astrophysics (ASCA)* was launched by Japan in 1993, and was terminated in 2000. It could cover the energy range roughly 0.4 to 10 keV with millisecond timing resolution.

The *Rossi X-ray Timing Explorer* was launched by the US in 1995 and is still operating. It can see X-rays in the 2 to 250 keV range and has excellent timing resolution like ASCA, but also has an extremely high effective area. It also has an All Sky Monitor instrument, which allows it to view 80% of the sky every orbit.

In 1999, the US launched the *Chandra X-ray Observatory*, which observes X-rays in the 0.1 to 10 keV range. It has a high effective area and extremely good ($\sim 0.5''$) spatial resolution. Also in 1999, the European satellite *XMM-Newton* was launched. It is similar to *Chandra*, but has a larger effective area and worse spatial resolution ($\sim 1''$).

Japan launched *Suzaku* in 2005. This telescope was supposed to have unprecedented spectral resolution from its micro-calorimeter instrument; however, this instrument failed shortly after launch. *Suzaku*'s other instruments, the X-ray Imaging Spectrometer and Hard X-ray Detector still function, and can observe photons in the 0.2 to 600 keV range.

Other modern X/γ-ray telescopes which I do not mention in this dissertation include *Swift* and *INTEGRAL*.

1.5 The Eddington Limit

The Eddington Limit is usually considered the upper limit for accretion onto a compact object or star; later, it will be shown that it may be possible to violate this limit (Chapter 4). If an accreting object's luminosity exceeds the Eddington limit, the radiation pressure will blow away the accreting material.

To find the limit, one assumes spherical accretion and that the radiation pressure gradient is equal to the gravitational pressure gradient (see, e.g., Carroll and Ostlie 1996; Frank et al. 2002).

The radiation pressure gradient is given by

$$-\frac{dP}{dR} = \frac{\kappa\rho}{c}\frac{L}{4\pi R^2} \tag{1.5}$$

where ρ is the mass density of the accreting gas, L is the accretion luminosity, R is the distance from the central object, and κ is the opacity. This equation is derived in Appendix A. It will be assumed that the accreting gas is purely hydrogen and that energy is deposited in the gas only by Thomson scattering, so that $\kappa = 0.4\ \mathrm{cm}^2\ \mathrm{g}^{-1}$. The gravitational pressure gradient is given by:

$$\frac{dP}{dR} = \frac{GM\rho}{R^2} \tag{1.6}$$

where G is the gravitational constant and gas is accreting onto an object of mass M. Equating Eqns 1.5 and 1.6 and solving for L gives:

$$L_{Edd} = \frac{4\pi GMc}{\kappa} = 1.3 \cdot 10^{38} \left(\frac{M}{M_\odot}\right)\ \mathrm{erg\,s^{-1}} \tag{1.7}$$

which is known as the Eddington luminosity. The Eddington accretion rate is usually defined as

$$\dot{M}_{Edd} \equiv \frac{L_{Edd}}{c^2} = \frac{4\pi GM}{\kappa c}. \tag{1.8}$$

Luminosities from accreting sources are often expressed as fractions of the Eddington luminosity, and accretion rates are often expressed as fractions of the Eddington accretion rate ($\dot{m} \equiv \dot{M}/\dot{M}_{Edd}$). Note that while the luminosity is less than the Eddington limit, the accretion rate need not be by this definition, as not all of the energy from accretion is released as radiation. Luminosities from accretion have an accretion efficiency, η (which is usually taken to be ~ 0.1) such that

$$L = \eta \dot{M} c^2. \tag{1.9}$$

This implies then that the accretion rate can be written as:

$$\dot{m} = \frac{1}{\eta}\frac{L}{L_{Edd}}. \tag{1.10}$$

One can apply the Eddington accretion limit to the standard theory for accretion disks (Shakura and Sunyaev 1973). A local Eddington flux, the maximum flux that can be emitted from an annulus in the disk at radius R, can be defined as

$$F_{Edd} = \frac{L_{Edd}\delta}{4\pi R^2} = \frac{cGM\delta}{\kappa R^2} \tag{1.11}$$

where the factor $\delta \equiv h/R$ (h is the height of the disk) takes into account the fact that the accretion is non-spherical. According to the theory of Shakura and Sunyaev (1973), the flux radiated from an accretion disk at a certain radius is given by

$$F = \frac{3}{8\pi}\frac{GM\dot{M}D}{R^3}, \tag{1.12}$$

where $D \equiv 1 - (R_{in}/R)^{1/2}$ and $R_{in} = 6GM/c^2$ is the radius of the innermost stable circular orbit. The local Eddington ratio can then be defined as

$$l \equiv \frac{F}{F_{Edd}} = \frac{3}{2}\frac{\dot{m}D}{\delta r} \tag{1.13}$$

where $r \equiv c^2R/GM$. For normal accretion disks, l cannot exceed unity.

1.6 Overview

In this dissertation I describe research into accreting X-ray sources. Most of this research has made use of a Monte Carlo/Fokker-Planck code, which I have parallelized to take advantage of computers with multiple processors. I describe this code and my modifications in Chapter 2. I have then applied this code to a photon bubble model for ultraluminous X-ray sources. I describe these ultraluminous X-ray sources and their observational properties in Chapter 3, and the application of the code to them in Chapter 4. In addition to this theoretical work, I have undertaken an observational project to determine the redshifts of several blazars from their optical spectra. In doing so, I have taken advantage of Ohio University's recent purchase of a share of the MDM Observatory. This work is described in Chapter 5. Finally, I will conclude with some general statements on the future of research into accreting astrophysical objects in Chapter 6.

This dissertation has three appendices. The first is a simple derivation of eqn. 1.5. The second describes sample input files for the MC/FP code, which I hope will make it easier for others to use the code in the future. The last Appendix contains plots of all the simulated spectra I describe in Chapter 4.

Chapter 2

Monte Carlo/Fokker-Planck Code

2.1 Introduction

In this section, I describe the Monte Carlo/Fokker-Planck code which I have used in simulating photon bubbles in accretion disks. I discuss the history of the code and previous applications (§ 2.2), and a basic outline of how it works (§ 2.3). As the code is very computationally intensive, I have made changes to allow it to run on computers with multiple processors; I describe these changes in § 2.4.

2.2 History of MC/FP code

As an alternative to the Kompaneets equation (Kompaneets 1957), Compton scattering in a high temperature, relativistic plasma can be handled by a Monte Carlo numerical method as developed by, e.g., Pozdniakov et al. (1983) and Canfield et al. (1987), and described below in § 2.3.1. The code of Canfield et al. (1987) involved electrons drawn from three spatial dimensions rather than just one. Liang and Dermer (1988) added pair production and annihilation to the code and used it to simulate the gamma-ray bump in some Cygnus X-1 spectra. Böttcher et al. (1998) coupled this code with the photoionization and line-transfer code XSTAR to simulate XRB X-ray spectra. In their model, the Comptonized photons from the corona were Compton-reflected off of the optically thick disk and reprocessed through the corona. They found that the reflection component in XRB spectra is usually negligible. Böttcher and Liang (1998) improved the code so that it could handle spherical and slab geometries, and allowed the volume to be divided into a one-dimensional grid, with different parameters (e.g., temperatures, densities) in the different zones. They studied the power density spectra (PDS) and time lag spectra one would expect from black hole binaries. Their scenario involved a flaring in a soft photon source (representing the disk) located inside or outside of a Comptonizing region (representing a corona or advection dominated accretion flow). This scenario generally agrees with observations for unrealistically large Comptonizing regions; hence, Böttcher and Liang (1999) used the code to simulate PDS and time lags from an alternative scenario involving a cool blob moving inward through a hot disk or corona. They found it to be a viable model to explain some features of observed time lags in Cyg X-1 and GX 339-4.

Fokker (1914) [1] and Planck (1917) first used the Fokker-Planck equation to describe the Brownian motion of particles from collisions with a surrounding fluid. The equation describes the overall distribution of particles and their time evolution from random (i.e., stochastic) processes. Dermer and Liang (1989) used a Fokker-Planck equation to describe the evolution of the electrons in a thermal, Maxwell-Boltzmann plasma, in which the electrons and protons may have different temperatures, as may

---

[1] This paper is often incorrectly cited as being from volume 43 of *Annalen der Physik*. Also, in the Smithsonian/NASA Astrophysics Data System it is incorrectly cited as being published in 1913. It is correctly cited in this dissertation's bibliography.

be found in AGN or XRB accretion disks. In particular, they calculated contributions to the heating/cooling rate coefficient and dispersion coefficient (see § 2.3.2 below) from Coulomb interactions between the electrons and protons and electrons and electrons; inverse Compton scattering of photons off of electrons; thermal bremsstrahlung; and synchrotron/cyclotron emission. While Dermer and Liang (1989) assumed a completely thermal (Maxwell-Botzmann) plasma, Nayakshin and Melia (1998) derived expressions for the Fokker-Planck coefficients from an arbitrary electron distribution. They also provided an implicit finite difference numerical scheme and tests of its speed, numerical stability, and accuracy.

Böttcher and Liang (2001) coupled the implicit Fokker-Planck scheme of Nayakshin and Melia (1998) to their existing Monte Carlo code for Compton scattering. The code could now realistically handle the evolution of the electron spectrum. They also added stochastic acceleration by Alfvén waves, as well as effects of bremsstrahlung emission and absorption, and cyclotron and synchrotron emission and absorption. They used the code to treat radiative feedback and model a spherical accretion shell around a weakly magnetized neutron star.

Previous models for time lags in XRBs—a flaring disk and and inwardly drifting blob— were reevaluated with the improved code which allowed the electron temperature to evolve. Böttcher (2001) found that the radiative feedback from an evolving electron distribution significantly altered the light curves, PDS, and time lags for these scenarios. In fact, he found that, for a disk flare sandwiched by a Comptonizing corona, there is a dip in the hard X-ray light curve rather than a flare. The case of an outer disk flare impinging on an inner ADAF leads to time lags much smaller than any observed, and this scenario was ruled out. The inward drift blob scenario seemed to reproduce some of the alternating time lags observed in XRBs such as GRS 1915+105 and XTE J1550-564.

Böttcher et al. (2003) modified the code for a two-dimensional cylindrical geometry. They then used it in further simulations of soft disk flares sandwiched by hot coronae. This time, they did not find the dips found in the one dimensional case. Another flaring scenario, where a flare originates in the corona by a mechanism such as a magnetic reconnection event (Beloborodov 1999) was also simulated. The PDS were similar to the disk flare scenario, as were the time lags, although they were generally smaller.

2.3 Code Description

The current two dimensional Monte Carlo/Fokker-Planck code has been described by Böttcher et al. (2003), which is an extension of the one dimensional MC/FP code described by Böttcher and Liang (2001). The code uses Monte Carlo methods to determine the relativistic photon transport and scattering (see § 2.3.1 below), and a Fokker-Planck equation to determine electron evolution (as described in § 2.3.2). In the current two dimensional code, the simulated region is cylinder-shaped and divided into an arbitrary number of radial and vertical zones. Each zone has its own value for certain properties, i.e., electron and proton temperatures, electron densities, magnetic field strengths, and plasma-wave turbulence properties, which are assumed to be homogeneous within each zone. The MC/FP code is written in FORTRAN 77, and consists of approximately 40,000 lines of code.

Photons are represented by Monte Carlo (MC) particles; each MC particle corresponds to a certain number of photons, which depends on the arbitrary number of MC particles the user chooses. The MC particles can be injected into the simulated volume at any boundary. Each MC particle is created with a certain energy "weight"; that is, the sum of the energies of the photons the particle represents. As the simulation continues, photons may be lost through absorption, lowering the MC particle's "weight" accordingly. When an MC particle's "weight" drops below a certain user specified amount, it is removed from the simulation. Hereafter, I will refer to the MC particles themselves as the photons, even though they are meant to represent several photons.

In each photon time step, then, the particles make their way through the zones and interact with the plasma in each one by Compton scattering as well as cyclotron/synchrotron and bremsstrahlung processes. Once a photon leaves the simulation volume it is added to an event file, which can be used later to extract angle dependent light curves and time– and angle–dependent spectra. Each photon has a time stamp that indicates when it exited the simulation volume, so that light travel time is taken into account. The electron distribution evolves faster than the photon distribution, however, so during each time step in which an MC scheme is used to compute photon scatterings, there are several time steps in which an FP scheme is used to update the electron distribution.

2.3.1 Monte Carlo Scattering for Photons

In the current MC/FP code the photon transport properties are simulated using the MC technique described in Pozdniakov et al. (1983) and Canfield et al. (1987). As stated above, photons originate from a blackbody or other user-specified source outer boundary of the simulation volume, or from synchrotron or bremsstrahlung within a particular zone. At the beginning of each time step, for each MC particle, three major quantities are calculated: (1) the distance the photon will travel in this time step if it is unscattered (equal to the speed of light times the length of the time step); (2) the distance to the zone boundary; and (3) the distance the MC particle can travel until it is scattered (the free path). The free path is drawn randomly from a distribution based on the mean free path, $\lambda = -\ln(\xi)\bar{\lambda}$, where ξ is a random number between 0 and 1 (but not including 0). The mean free path is calculated by (Pozdniakov et al. 1983)

$$\bar{\lambda} = \frac{\int_0^\infty n_e(p) p^2 dp}{n_e \int_0^\infty n_e(p) \sigma_{eff}(p, E) p^2 dp} \tag{2.1}$$

where p is the momentum of the electron, and E is the energy of the incident photon. σ_{eff} is the effective scattering cross-section, which is the Klein-Nishina cross-section averaged over scattering angle.

What is done next depends on which of these three quantities is smallest. If (1) is smallest then the photon's new position at the end of the time step will be calculated and the photon will be stored in a census file until the next time step. If (2) is smallest then the photon's new position will be calculated and the simulation will resume in the adjacent zone. If (3) is smallest, then the scattering calculation will be performed. There is also a probability that the photon will be absorbed, by a process such as lepton pair production, free–free absorption, or synchrotron absorption. If the probability of absorption is P, then the MC particle's statistical weight w will be decreased by wP.

If the particle is scattered, the scattering calculation is performed after randomly drawing the electron's speed from the thermal/nonthermal electron distribution (which is determined by the Fokker-Planck equation; see § 2.3.2) and the direction of its travel. Angles are selected in such a way that head-on collisions are more likely. The electron's speed is selected from a distribution that favors higher values for the KN cross-section. The scattered photon's energy and direction are calculated as described in Pozdniakov et al. (1983).

2.3.2 Fokker-Planck Scheme for Electron Evolution

During each photon cycle where MC scatterings are calculated, the electron distribution is calculated based on the FP scheme described in Nayakshin and Melia (1998). The electron distribution in each zone is initially represented by a thermal

Maxwellian distribution with a nonthermal power law tail described by the parameters in each zone (i.e., electron temperature, particle density and fraction of electrons that are Maxwellian). The electron distribution, $n_e(\gamma, t)$ then evolves according to the FP equation for locally homogeneous and isotropic situations:

$$\frac{\partial n_e(\gamma,t)}{\partial t} = -\frac{\partial}{\partial \gamma}\left[n_e(\gamma,t)\frac{d\gamma}{dt}\right] + \frac{1}{2}\frac{\partial^2}{\partial \gamma^2}\left[n_e(\gamma,t)D(\gamma,t)\right] \tag{2.2}$$

where $d\gamma/dt$ is the heating/cooling rate and

$$D(\gamma,t) = \frac{d(\Delta\gamma^2)}{dt} \tag{2.3}$$

is the energy dispersion coefficient. The parameters $d\gamma/dt$ and $D(\gamma, t)$ are found by summing the contributions from Coulomb scattering, Compton scattering, Alfv́en turbulence, synchrotron and bremsstrahlung; see § 2.3.3 and § 2.3.4.

When Eqn. 2.2 is discretized, it can be represented as a tridiagonal system of linear equations. This system is then solved implicitly for the electron distribution at the next time step. The implicit scheme has been shown to be unconditionally numerically stable and faster than the explicit scheme (Böttcher and Liang 2001). We also make use of the following approximation: when computing $d\gamma/dt$ and $D(\gamma, t)$ for the next time step, it is assumed that the electron distribution will be completely thermal; the distribution is fit with a Maxwellian, giving a temperature for the distribution, and the electron distribution for the next time step is calculated based on this, from a simple energy balance calculation. Then the $d\gamma/dt$ and $D(\gamma, t)$ coefficients for elastic Coulomb (i.e., electron-proton) and Møller (i.e., electron-electron) scattering are used in the numerical Fokker-Planck equation to calculate the actual electron distribution for the next time step. $d\gamma/dt$ and $D(\gamma,t)$ for other sources (e.g., inverse Compton scattering, synchrotron, etc.) evolve slowly enough that their value at the beginning of the time step can be used. This technique should be valid if the distribution does not differ significantly from a Maxwellian.

2.3.3 Library of Fokker-Planck Coefficients

The $d\gamma/dt$ and $D(\gamma,t)$ coefficients for Coulomb (e-p)and Møller (e-e) scattering for Maxwellian distributions are given by (Nayakshin and Melia 1998):

$$\begin{aligned}
\left(\frac{d\gamma}{dt}\right)_{ee} &= \frac{2\pi r_e^2 c n_e \ln\Lambda}{\beta_e\gamma_e^2\Theta_e K_2(1/\Theta_e)}\int d\gamma_1 \exp[-\gamma_1/\Theta_e]\chi(\gamma_e,\gamma_1) \\
D_{ee} &= \frac{4\pi r_e^2 c n_e \ln\Lambda}{\beta_e\gamma_e^2\Theta_e K_2(1/\Theta_e)}\int d\gamma_1 \exp[-\gamma_1/\Theta_e]\left[\tfrac{1}{2}(\gamma_e-\gamma_1)^2\chi(\gamma_e,\gamma_1)+\xi(\gamma_e,\gamma_1)\right] \\
\left(\frac{d\gamma}{dt}\right)_{ep} &= \frac{2\pi r_e^2 c n_p \ln\Lambda m_e}{\beta_e\gamma_e^2\Theta_p K_2(1/\Theta_p)}\int d\gamma_p \exp[-\gamma_p/\Theta_p]\psi(\gamma_e,\gamma_p) \\
D_{ep} &= \frac{2\pi r_e^2 c n_p \ln\Lambda m_p m_e}{\beta_e\gamma_e^2\Theta_p K_2(1/\Theta_p)}\int d\gamma_p \exp[-\gamma_p/\Theta_p]\eta(\gamma_e,\gamma_p)
\end{aligned} \tag{2.4}$$

where the subscript ee refers to e-e elastic Coulomb scattering (i.e., Møller scattering) and the subscript ep refers to e-p elastic Coulomb scattering. Above, r_e is the classical electron radius ($r_e = e^2/m_ec^2$); γ_e (γ_p) is the Lorentz factor for the electron (proton); $\beta = \sqrt{1-1/\gamma^2}$; Θ_e (Θ_p) is the electron (proton) temperature in terms of the electron's (proton's) rest energy, i.e., $\Theta_e = kT_e/m_ec^2$ ($\Theta_p = kT_p/m_pc^2$); and K_2 is the modified Bessel function of order 2. $\ln\Lambda$ is the Coulomb logarithm, given by:

$$\ln\Lambda = \frac{1-\Psi_{max}}{1-\Psi_{min}}$$

where Ψ_{max} and Ψ_{min} are the maximum and minimum scattering angles in the center of momentum frame, respectively. The logarithm $\ln \Lambda$ is a slowly varying function of electron energy, and it was assumed to be constant. Eqns. 2.4 make use of the following functions:

$$\chi(\gamma_e, \gamma_1) = \int_{\gamma_1\gamma_e(1-\beta_e\beta_1)}^{\gamma_1\gamma_e(1+\beta_e\beta_1)} dx \frac{x^2}{\sqrt{(x+1)(x-1)^3}}$$

$$\xi(\gamma_e, \gamma_1) = \int_{\gamma_1\gamma_e(1-\beta_e\beta_1)}^{\gamma_1\gamma_e(1+\beta_e\beta_1)} dx \frac{x^2}{\sqrt{x^2-1}} \left[\frac{(\gamma_e+\gamma_1)^2}{2(1+x)} - 1\right]$$

$$\psi(\gamma_e, \gamma_p) = \int_{\gamma_p\gamma_e(1-\beta_e\beta_p)}^{\gamma_p\gamma_e(1+\beta_e\beta_1)} dx \frac{x^2}{S_p(x-1)^{3/2}} [(x-1)(m_p x - m_e\gamma_e) + (m_p + m_e)(x - \gamma_e)]$$

$$\eta(\gamma_e, \gamma_p) = \int_{\gamma_p\gamma_e(1-\beta_e\beta_p)}^{\gamma_p\gamma_e(1+\beta_e\beta_1)} dx \frac{x^2}{S_p(x-1)^{1/2}} \left\{ \frac{(m_p\gamma_p + m_e\gamma_e)^2}{S_p} - 1 \right.$$
$$\left. - \frac{[(x-1)(m_p\gamma_p - m_e\gamma_e) + (m_p+m_e)(\gamma_p - \gamma_e)]^2}{S_p(x^2-1)} \right\}$$

where $S_p = m_p^2 + m_e^2 + 2m_p m_e x$. Calculating the Coulomb scattering coefficients in particular is computationally intensive, and a library of them has been created which can be read in, rather than being calculated every time they are needed . As a service to the scientific community, this library has been made publicly available. Rate files can be downloaded through the world wide web at:

`http://www.phy.ohiou.edu/~finke/rates`.

The file dge.tar.gz, when unzipped and untarred, contains all the files for elastic electron-electron scattering. Each file has a name corresponding to the electron temperature of the plasma in keV (e.g., dge0148.dat corresponds to an electron temperature of 148 keV). The libraries for electron-proton scattering are contained in the files beginning with dgp. When unzipped and untarred, the libraries consist of numerous files with a name corresponding to the proton temperature of the plasma, in tens of keV (e.g., dgp1275 corresponds to a proton temperature of 12.750 MeV). For temperatures of $kT_p \geq 100$ MeV, the ”p” is replaced by the first digit of the number symbolizing the proton temperature (e.g., dg17899.dat contains data for scattering in a plasma with a proton temperature of 178.990 MeV).

Each library file, whether the scattering is incident on electrons or protons, contains three columns. The first is the Lorentz factor of the incident electron. The second column contains the energy exchange coefficient, $d\gamma/dt$, and the third the dispersion coefficient, D. The coefficients were calculated for small-angle scattering approximations using Eqns. 2.4 with integrals computed numerically. All rates are normalized to a background electron and proton density, respectively, of 1 cm^{-3}, and the actual rates will be linearly proportional to the density, as seen in Eqns. 2.4.

2.3.4 Other Fokker-Planck Coefficients

For synchrotron and bremsstrahlung, the dispersion coefficients are negligible compared to the other processes. For synchrotron, the energy exchange coefficient is:

$$\left(\frac{d\gamma}{dt}\right)_{sy} = \frac{4}{3} c\sigma_T \frac{B^2}{8\pi}(\gamma^2 - 1). \tag{2.5}$$

(Rybicki and Lightman 1979). For bremsstrahlung, the coefficient is given by:

$$\left(\frac{d\gamma}{dt}\right)_{br} = \langle\dot{\gamma}\rangle\gamma^{1.1} \tag{2.6}$$

(Haug 1985; Böttcher and Liang 2001) where $\langle\dot{\gamma}\rangle$ is the rate averaged over the electron distribution.

Alfv́en waves can accelerate particles with its electric fields through resonant interactions between the particles and electric fields that are perpendicular to the waves' direction of motion. The energy exchange and dispersion coefficients, respectively, for this acceleration are given by:

$$\left(\frac{d\gamma}{dt}\right)_A = \frac{\pi(q-1)}{q}\frac{\omega_c^q\ m_e}{8\pi n_e e^2}k_{min}^{q-1}\left(\frac{B_0}{\delta B}\right)^2 c^{q-3}(\gamma\beta)^{q-1}$$

$$D_A = \frac{\pi(q-1)}{4q(q+2)}\frac{\omega_c^q\ m_e}{4\pi n_e e^2}k_{min}^{q-1}\left(\frac{B_0}{\delta B}\right)^2 c^{q-3}\gamma^q\beta^{q+1} \tag{2.7}$$

(Schlickeiser 1985; Böttcher 1997) where q is the power-law from Kolmogorov Turbulence (usually, $q = 2.5$) and $\delta B/B_0$ is the time-dependent variation of the wave's magnetic field.

The total energy exchange coefficient and dispersion coefficient used in the FP equation (Eqn. 2.2) is the sum of the above coefficients, such that:

$$\frac{d\gamma}{dt} = \left(\frac{d\gamma}{dt}\right)_{ee} + \left(\frac{d\gamma}{dt}\right)_{ep} + \left(\frac{d\gamma}{dt}\right)_{sy} + \left(\frac{d\gamma}{dt}\right)_{br} + \left(\frac{d\gamma}{dt}\right)_A$$

$$D = D_{ee} + D_{ep} + D_A. \tag{2.8}$$

2.3.5 Assumptions and Limitations of the Code

The Coulomb FP coefficients are given by Eqns. 2.4. These contain $K_2(1/\Theta)$, the modified Bessel function of order 2. For $\Theta^{-1} \gg 1$, this function can be approximated as:

$$K_2(1/\Theta) \approx \sqrt{2\pi\Theta}\; e^{-1/\Theta} \left[1 + \frac{35\Theta}{8} + \frac{945\Theta^2}{128} + O\left(\Theta\right)\right] \tag{2.9}$$

As Wolfe and Melia (2006) have pointed out, as Θ goes to 0, the exponential in Eqn. 2.9 goes to 0, and thus the FP coefficients go to 0; here the calculation of the coefficients can suffer from significant underflow errors. If the limit is $\Theta \gtrsim 0.01$—where the coefficients of Nayakshin and Melia (1998) differ significantly from those in Wolfe and Melia (2006)— then the lower limits for the electron and proton temperatures, respectively, are ~ 5 keV and ~ 9 MeV.

The Comptonizing plasma is assumed to be fully ionized hydrogen. Thus, a constraint is found where bound-free or free-bound processes become substantial. The ratio of free to bound electrons is given by the Saha equation:

$$f = \frac{n_{free}}{n_{bound}} = \frac{2Z_{free}}{n_{free}Z_{bound}} \left(\frac{2\pi m_e kT}{h^2}\right)^{3/2} \exp\left(-\frac{\chi}{kT_e}\right) \tag{2.10}$$

where n_{free} and n_{bound} are the densities of the free and bound electrons, respectively, $Z_{free} = 1$ and $Z_{bound} = 2$ are the partition functions for the bound and free states, respectively, m_e is the mass of the electron, and $\chi = 13.6$ eV is the ionization energy for hydrogen. Note that $n_{free} + n_{bound} = n_e$, the total electron density. Requiring that $f \gtrsim 0.9$, and assuming that $\exp\left(-\frac{\chi}{kT_e}\right) \sim 1$, one gets the constraint:

$$n_e \lesssim 10^{26} \left(\frac{kT_e}{\mathrm{keV}}\right)^{3/2} \ \mathrm{cm}^{-3} \tag{2.11}$$

The Fokker-Planck equation assumes that the average energy exchanged in a collision is small; i.e., $\Delta E/E \ll 1$. For inverse Compton Scattering of photons by a thermal electron distribution, the average energy exchanged per scattering is given by (Rybicki and Lightman 1979):

$$\frac{\Delta E}{E} = \frac{4kT_e}{m_e c^2}. \tag{2.12}$$

This leads to a constraint on the electron temperature, $kT_e \ll 138$ keV.

Electron-positron pair production from interactions with protons is not taken into account by the code. So if an electron's kinetic energy is above the e^--e^+ threshold energy in the proton's rest frame– about 1 MeV–the code will not be correct. If we assume an electron energy of $\sim 50\,\mathrm{keV}$ this gives:

$$kT_p \lesssim 100 \ \mathrm{MeV}. \tag{2.13}$$

The Fokker-Planck equation also assumes the electron distribution is well-described by a statistical distribution function. If one expects this condition to be met by ~ 10 particles per bin, and noting that the code uses 100 bins for the electron distribution, then

$$n_e V \gtrsim 1000 \tag{2.14}$$

where V is the volume of the particular zone.

Note that all of the constraints above, except Eqns. 2.11 and 2.14 are due to the Fokker-Planck routine for electron evolution. If the code is used in constant-temperature mode, then these constraints do not apply.

2.4 Parallelization

A flowchart of the overall logic of the MC/FP code can be seen in Fig. 2.1. When it is run, the first subroutine it calls is READER. This routine reads in data from input files; an overall input file ("input.dat"; see Appendix B) that contains the number of zones, the size of the simulation volume, how long the simulation will run, the blackbody temperature of surface sources (if any), and other information. It also reads in separate input files for each zone (again, see Appendix B for more details), each one of which contains variables which are intrinsic to each zone. The next major subroutine called is SETUP. This does some basic overhead calculations that will be used in the routine. It calculates the dimensions, volumes, and surface areas of each zone, sets up probability distributions for Compton scattering, Compton reflection, and absorption, sets up an energy grid for the electron-positron distribution in each zone, and initializes various variables.

After this, begins the actual execution of the photon tracking and updating of the electron distribution (in the routine XEC). For each time step, the subroutines IMCGEN, IMCSURF, IMCVOL, IMCFIELD, and UPDATE are called, in that order. IMCGEN calculates how much energy is generated from volume sources (e.g.,

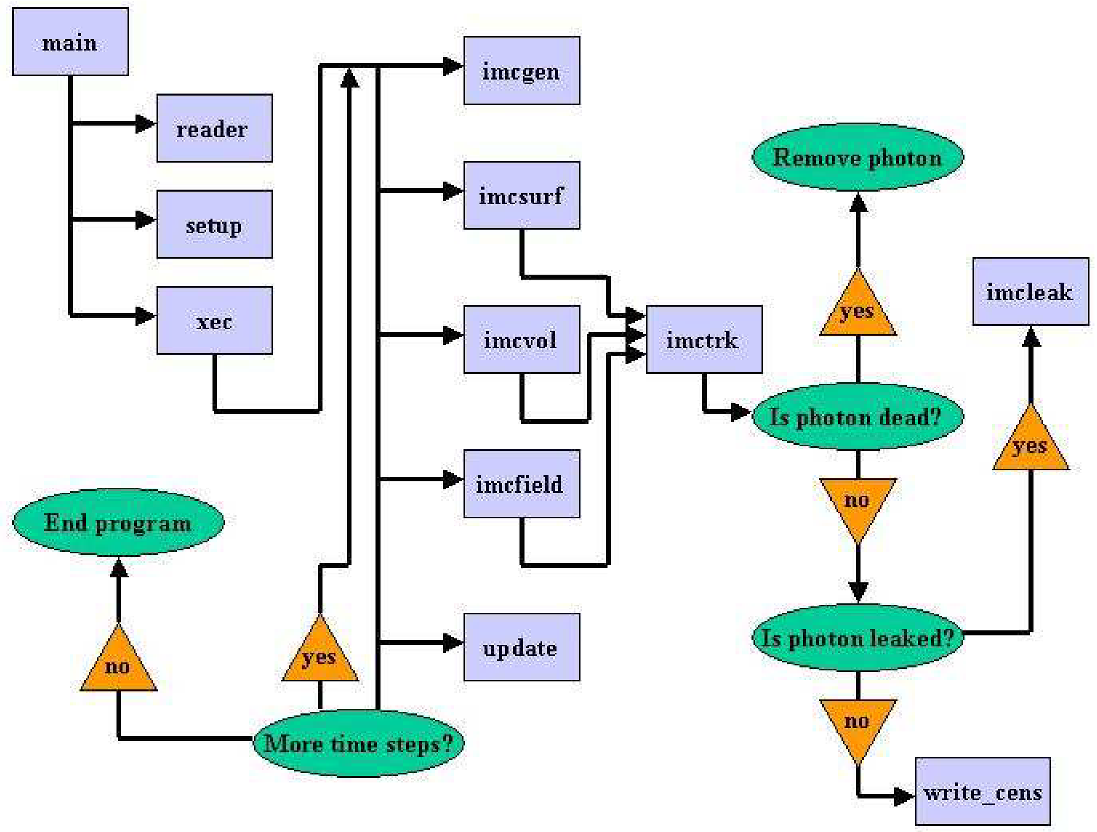

Figure 2.1: A flowchart of the MC/FP code.

from synchrotron, bremsstrahlung, or pair annihilation) and boundary sources, and determines how many photons are generated from these sources as well as returning from the census file. IMCSURF deals with the photons generated from the surface sources, which can either be blackbodies or user-specified distributions. It randomly picks photons from these distributions, and for each photon, calls subroutines which track it and perform Compton scattering and absorption calculations with a Monte Carlo method described above. IMCVOL does the same thing as IMCSURF, except for photons generated inside the simulation volume. IMCFIELD reads in photons from the previous time step from a census file, and tracks them with the same subroutines. UPDATE updates the electron-positron distribution based on energy losses or gains from Compton scattering, Coulomb scattering, and other sources, using the Fokker-Planck method described above.

Using routines from Message Passing Interface (MPI), I have restructured the MC/FP code so that it can run on parallel computers. I have parallelized the three routines IMCSURF, IMCVOL, and UPDATE with the master-slave algorithm from Gropp et al. (1999). In this algorithm, each slave process performs the calculation of a single zone. When a slave process is finished, it is given another zone to work on by the master process. This ensures that the slaves have little idle time and the entire job is finished quickly. The code which accomplishes this for the UPDATE routine can be seen below; the code for the IMCSURF and IMCVOL routines are similar.

```
      if(myid.eq.master) then
c     beginning of master part
cccccccccccccccccccccccccccccccccccccccccccccccccccccc
c
c     Broadcast data to all the processes needed in the
c     Fokker-Planck routine.
      call FP_bcast
c
c     This sends the first round of zones to the slaves for
c     processing.
      do 900 l = 1, min(num_zones, (numprocs-1))
         zone = l
         call FP_send_job(l, zone)
         num_sent = num_sent + 1
  900 continue
c
c     As slaves complete processing a zone, this receives the
c     results and sends the next zone to the slaves.
```

```
      do 902 l = 1, num_zones
            call FP_recv_result(sender, zone)
            if(num_sent.lt.num_zones) then
               zone = num_sent+1
               call FP_send_job(sender, zone)
               num_sent = num_sent + 1
            else
               call FP_send_end_signal(sender)
            endif
 902  continue
c
      call E_add_up(E_tot_old, E_tot_new, dT_max)
c
c
      else if(myid.ne.master) then
c     beginning of slave part
ccccccccccccccccccccccccccccccccccccccccccccccccccccccccccccccccc
c
c     receive broadcast of parameters used in FP_calc.
      call FP_bcast
c
c     if there are more nodes than work skip this node.
      if(myid.gt.num_zones) goto 990
c
c     as long as the node doesn't receive the end_signal, it
c     will keep performing the FP calculation for zones.
 991  call FP_recv_job(zone)
      if(zone.eq.end_signal) goto 990
      call FP_calc(zone)
      call FP_send_result(zone)
      goto 991
 990  continue
c
      call E_add_up(E_tot_old, E_tot_new, dT_max)
c
      endif
c     end of slave part
```

The master and slave process first call FP_BCAST, which broadcasts variables that all zones will need for the FP calculation. Then the master process enters a “do loop” where it calls FP_SEND_JOB for each slave process. This sends the “job” to the slave processes. A “job” consists of the variables an individual process will need to perform the calculation (such as the electron temperature in that zone and the energy deposited by Compton scattering into the electrons), as well as the number of the zone it is working on. Each FP_SEND_JOB call is matched by an FP_RECV_JOB call by the slave process. Next, the master process enters another “do loop” where it waits for the slave processes to send the results. When it receives a result with FP_RECV_RESULT, it immediately sends another “job” to that slave process (SENDER), unless there are no more zones. In this case, it sends the slave process an end signal (FP_SEND_END_SIGNAL). After all the zone calculations are done, the subroutine FP_ADD_UP computes the total energy that went into all the zones at the beginning of the time step (E_TOT_OLD), the total energy lost by all the zones by the end of the time step (E_TOT_NEW) and the largest change in temperature of a zone (DT_MAX). These variables are used to calculate the size of the next time step.

From a slave process’ point of view, it first receives the broadcast from the master process (FP_BCAST). Then it decides if it needs to do any work; if there are more processes than zones, then the process may not be needed. Assuming the process is needed, it will receive the “job” from the master process (FP_RECV_JOB) and, unless the job contains the end signal, it will perform the FP calculation (FP_CALC). It will then send the result to the master process (FP_SEND_RESULT), a call which is matched with a FP_RECV_RESULT by the master process. When a slave process finally does receive the end signal, it will assist the master process with E_ADD_UP.

The photon-tracking and Fokker-Planck calculations require a considerable amount of overhead. In the SETUP routine, a new subroutine was added which broadcasts the variables initialized in that routine to all the processes. In addition, at the beginning of IMCSURF, IMCVOL, IMCFIELD, and UPDATE, variables necessary for those respective calculations are broadcast to all the processes; for example, the energy deposited in each zone and in the census is summed up before UPDATE is executed.

Each slave process has its own event file and census file. The event files are added together to create one large event file in post-processing, and from this light curves and spectra are extracted. Each census file contains the particles left over from the previous time step's IMCSURF and IMCVOL routines. In IMCFIELD (which is also parallelized), each slave process performs the photon tracking on the photons in its census file.

2.4.1 Parallel Random Number Generator

Two pseudo-random number generators can be used by the MC/FP code. The first is the linear congruent random number generator from Press et al. (2001) (which is itself based on a linear congruent generator from Knuth 1997). In this case, the string of random numbers will be different for each process, and thus, results of the simulation will be different for different number of processes used. However, results converge statistically.

The other random number generator used is a variation of the lagged Fibonacci random number generator from Knuth (1997). This generator has been parallelized such that every zone calculation will have its own string of random numbers. Thus, the random numbers produced will be the same, and the result of the simulations will be identical, regardless of how many processes are used. In addition, each photon stored in the census file has its own random number seed, and thus, will have its own set of random numbers, independent of processor. This is very useful for debugging purposes. However, the lagged Fibonacci generator is considerably slower than the linear congruent one, and was not used in real applications.

The MC/FP code makes $\sim 10^7$ calls to the random number generator per time step; it is unlikely that a simulation run will have more than $\sim 10^4$ time steps, so the most random numbers used will be $\sim 10^{11}$. The linear congruent generator has a period of $\sim 10^{15}$ and the lagged Fibonacci has a period $\gtrsim 10^{18}$, so both generators provide more than enough random numbers without repeating the sequence.

2.4.2 Speed of Parallelized Code

The parallelized MC/FP code was tested for speed on the Pentium 4 Cluster at the Ohio Supercomputing Center (OSC) in Columbus, Ohio. This machine consists of 256 computing nodes (plus nodes for login, servers and memory storage); each computing node consists of two 2.4 GHz Xeon processors. Communication between processors on the same node is quicker than inter-node communication; thus, on this machine parallel jobs are run optimally with a number of processors that is a multiple of two. The time it takes a simulation to run is dependent on how fast information can be moved from one node to another. One hundred twelve nodes on the Pentium 4 cluster are connected by a switched, 8 Gbits/s network, and therefore can move information faster than the other nodes, so that running times for the same simulation can vary considerably; furthermore, a different random number stream is generated for each simulation, leading to further speed variations. A plot of average speeds for the same simulation with various number of processors can be seen in Fig. 2.2. The test simulation used was a coronal flare simulation with electron evolution similar to those of Böttcher et al. (2003). All speeds are normalized to the speed for simulation to run as a serial job, and were determined by taking the inverse of the run time. As the number of processors increases, the speed gain decreases; at some point, the speed should be approximately independent of the number of processors. It appears that the optimal number of processors used is around six. Optimally, the normalized speed would be equal to the number of processors (i.e., when four processors are used, the simulation will be four times as fast as the serial version); however, this is not obtained, due to overhead in transferring the considerable data between processors. The maximum speed obtained is around 2.5 times the speed of the serial version.

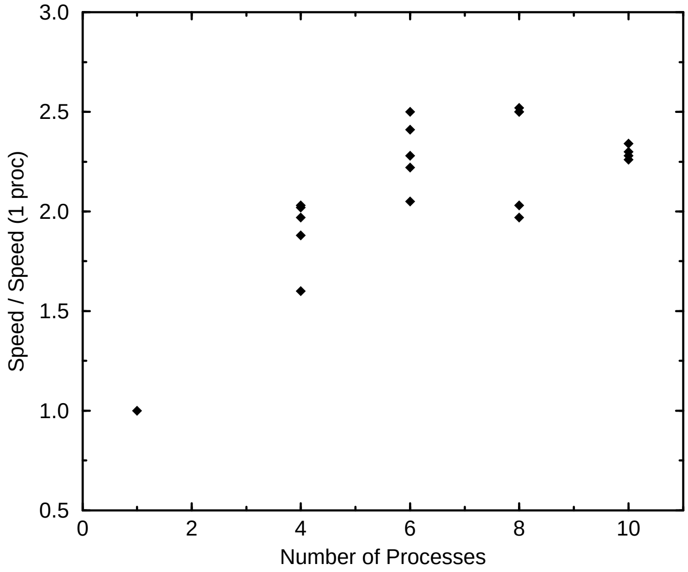

Figure 2.2: The speed of test simulations run with different numbers of processors.

2.5 Summary

The 2-D MC/FP code has been described. I have created a library of Fokker-Planck Coulomb scattering coefficients for the electron evolution routine, to expedite computation. This library has been made publicly available. I have parallelized the 2-D MC/FP code with MPI and tested its speed for different number of processors, running it on the Pentium 4 Cluster. With six processors, the maximum speed obtained was ~ 2.5 times as fast as the serial version. I have also included a new random number generator which allows the same stream of random numbers to be used, regardless of the number of processors used, although this generator slows down the code considerably.

Chapter 3

Ultraluminous X-ray Sources

3.1 Introduction

Approximately 150 off-nuclear Ultraluminous X-ray Sources (ULXs) in nearby galaxies have been discovered with luminosities greater than 10^{39} erg s^{-1}, exceeding the Eddington luminosity for a $\sim 10 M_{\odot}$ black hole (e.g., Fabbiano 1988; Colbert and Mushotzky 1999; Colbert and Ptak 2002; Liu and Mirabel 2005). While some can be identified as supernova remnants, background Active Galactic Nuclei, or faint foreground stars (e.g., Gutiérrez 2006), most seem to be the result of accretion from a high-mass star onto a compact object. Short-term variability of some of these ULXs indicates that they are not simply unresolved superpositions of several lower-luminosity sources (e.g., Matsumoto et al. 2001; Fabbiano et al. 2003). Thus, the high luminosity implies accretion onto black holes with masses $50 M_{\odot} < M < 10^4 M_{\odot}$, (intermediate mass black holes; IMBHs; Colbert and Mushotzky 1999; Makishima et al. 2000; Hui et al. 2005; Madhusudhan et al. 2006) or super–Eddington accretion. IMBHs present considerable difficulties for formation scenarios. Super–Eddington accretion presents its own theoretical difficulties, but generally, could be achieved in two different ways: An inhomogeneous accretion-disk structure in which the photon flux is spatially separated from the bulk of the matter influx, or strongly anisotropic radiation.

Anisotropic emission (King et al. 2001) may originate, e.g., from jet sources associated with accretion onto solar-mass black holes (microquasars) in which the jet is oriented at a small angle with respect to our line of sight — the so-called "microblazar" model (Georganopoulos et al. 2002; Körding et al. 2002). The latter model is now considered unlikely based on recent observations of X-ray ionization of optical nebulae associated with some ULXs (Pakull and Mirioni 2003; Gutiérrez 2006).

A promising mechanism for sustaining super-Eddington accretion in a radiation-dominated, magnetized accretion flow, is provided by the so-called photon bubble instability (Arons 1992; Gammie 1998; Begelman 2001, 2002, 2006b). In this model, radiation can escape along low-density regions (LDRs) aligned with predominantly vertical magnetic field lines. The accretion flow is concentrated in thin, optically thick high-density regions (HDRs), where the magnetic pressure of field lines oriented predominantly within the disk dominates over the gas pressure, thus confining the gas and preventing the radiation pressure from disrupting the accretion flow. In such a configuration, the total disk luminosity can exceed the Eddington luminosity by a factor approximately equal to the ratio of the magnetic field pressure to the gas pressure (Begelman 2001, 2002) in the HDRs. The photon bubble model is discussed further in § 4. For the rest of this chapter I will discuss observational properties of ULXs.

3.2 Observational Properties

3.2.1 X-ray Spectra

Given the variety of different promising candidate models for the nature of ULXs, the obvious question is: can one distinguish between these models with ULXs' X-ray spectra? If so, what are the characteristic spectral features of the individual models? From an accreting IMBH it is generally believed that a multi-color disk blackbody (MCDBB) spectrum with an inner temperature of $kT_{in} \sim 0.1$ — 0.3 keV (that is, the disk temperature at the innermost stable circular orbit) and possibly a high energy component from Compton up-scattering in a tenuous, hot corona would be a realistic phenomenological description of the spectrum, analogous to solar–mass XRBs. However, a recent, more detailed analysis of non-LTE accretion flows around IMBHs (Hui et al. 2005) has indicated that the effects of black-hole rotation and Compton scattering within the disk may very well lead to much higher apparent disk temperatures, up to $kT \sim 1$ keV, in addition to deviations from conventional MCDBB spectra at both soft and hard X-ray energies due to metal opacity effects.

A featureless power-law spectrum would be expected from a microblazar, analogous to the spectra of (galaxy–sized) blazars. The continuum spectrum from the photon bubble model might be dominated by the MCDBB spectrum emanating from the HDRs. However, this spectrum might be modified during the radiation transport in the photon bubble cavities. Furthermore, the almost free-streaming radiation of the photon bubbles could be repeatedly Compton-reflected off the surfaces of the HDRs, potentially leading to strong fluorescence lines and/or radiative recombination edges, in addition to Compton reflection features from hard X-ray emission impinging upon the disk from radiation sources external to the disk (Ballantyne et al. 2004, 2005). Such features may be observable, assuming they are not overwhelmed by other radiation sources, in particular the blackbody from the HDRs.

Distinguishing scenarios by spectral modeling is currently very difficult for all but the highest quality ULX data sets, and spectral fitting to these ULX spectra gives contradictory results. For example, Feng and Kaaret (2005) recently performed a detailed spectral and timing analysis of archival *XMM-Newton* data on 28 ULXs that had sufficient photon statistics to allow for meaningful fitting with models more complicated than a simple power-law. They found that their continuum spectra fell into three general categories: (1) Optically thin bremsstrahlung-dominated, quasi-thermal spectra with temperatures of $kT \sim 0.6 - 0.8$ keV, characteristic for X-ray emission from young supernova remnants; (2) MCDBB spectra of temperatures $kT \sim 0.1 - 0.4$ keV, plus occasionally a hard X-ray power-law, as possible in the case of accretion onto IMBHs; (3) MCDBB spectra at temperatures $kT \sim 1$ keV, plus a power-law component dominating at lower energies. Based on these results, Feng and Kaaret (2005) suggest that ULXs may, in fact, not be a homogeneous class of objects. This is in accord with recent results of Winter et al. (2006a) that realistic stellar evolution and population synthesis calculations suggest that the expected rate of captures of massive stars by IMBHs may not be sufficient to produce the total observed number of ULXs. Winter et al. (2006b) classified ULXs into low/hard and high/soft states based on their X-ray luminosities and spectra, assuming the ULXs were IMBHs accreting in states similar to galactic X-ray binaries. They found that the high/soft ULXs were grouped around one of two blackbody temperatures: one grouped around 1 keV and one grouped around 0.1 keV, further indication that ULXs are not a homogeneous group. The long term monitoring of some ULXs such as NGC 5204 X-1 shows that their X-ray spectra harden as their flux increases, opposite to what has been observed in Galactic X-ray binaries (Roberts et al. 2006).

Stobbart et al. (2006) found that 6 out of 13 of the most-observed ULXs were fit approximately equally well with a cool MCDBB and hard power-law as with a soft power-law and warm MCDBB. Even more surprisingly, they found that most spectra (10 out of 13) were fit best by a cool, $kT \sim 0.2$ keV blackbody and a warmer $kT_{in} \sim 2$ keV MCDBB, and 11 out of 13 were fit by a cool MCDBB and an optically thick ($\tau \sim 10$) corona. These spectra could also be explained by a hot, inner (optically thick) plasma sphere and a cool outer disk (Agrawal and Misra 2006), in which case the cool blackbody temperature could not be directly related to the black hole mass by virtue of the relation between the inner disk temperature and the black hole mass.

Several spectral features not-associated with MCDBB or power-laws have been detected in X-ray spectra of ULXs. An Fe Kα line has been observed in M82 X-1 (Strohmayer and Mushotzky 2003; Agrawal and Misra 2006); absorption edges have been observed in the 0.1—1 keV range in M101 ULX-1 (Krawczynski et al. 2004); and possible edges at ~ 0.7 keV and ~ 8 keV, and an emission feature at ~ 6 keV has been seen in Holmberg IX X-1 (Dewangan et al. 2006a). In the ULX M51 X-26 emission features have been seen at 1.8 keV, 3.24 keV, 4.03 keV, and 6.65 keV with *Chandra* (Terashima and Wilson 2004) and at 6.4 keV with *XMM–Newton* (Dewangan et al. 2005). This indicates that the detection of emission lines and/or radiative recombination edges is currently feasible, at least for bright ULXs, and predictions of expected line features from various models will thus be useful as an additional model diagnostic.

In summary, current diagnostics for the distinction between different models for ULXs indicate that ULXs may in fact not be a homogeneous set of physical objects, different models may apply to different sources, and in many cases, observational results are inconclusive. Consequently, more detailed model predictions of various ULX models might be helpful in identifying additional diagnostics which may be used to confirm or rule out such models. In § 4 I will make predictions of the X-ray spectra from the photon bubble model of ULXs.

3.2.2 X-ray Timing Properties

As an alternative to spectral features, timing properties of ULXs have been suggested as diagnostics to distinguish between models. Kalogera et al. (2004) have pointed out that Shakura-Sunyaev-type accretion disks around IMBHs are expected to be subject to the thermal-viscous instability and should thus exhibit state transitions on long (months—years) time scales, analogous to state transitions in Galactic X-ray binaries, for black-hole masses exceeding a critical value of $\sim 50\,M_{\odot}$. In contrast, the (local) photon bubble instability has a (globally) stabilizing effect on radiation-pressure dominated accretion flows, allowing for persistent high-luminosity accretion states on long time scales. The fact that several ULXs have indeed exhibited significant long-term variability would then argue for the IMBH hypothesis.

Also, the rapid variability of ULXs can, in principle, be used as a diagnostic for the black-hole mass. Quasi–periodic oscillations (QPOs) have been observed for two ULXs, M82 X-1 (Strohmayer and Mushotzky 2003) and Holmberg IX X-1/M81 X-9 (Dewangan et al. 2006a). Based on a correlation between the QPO frequency and the spectral parameters of Galactic X-ray binaries, Dewangan et al. (2006b) infer a black-hole mass of $M_{\odot} \sim 25 - 520\,M_{\odot}$ for M82 X-1, and Dewangan et al. (2006a) infer an upper limit of $\lesssim 400\,M_{\odot}$ for the black hole in Holmberg IX X-1; it should be noted, however, that these results are model–dependent.

Additionally, the power density spectra (PDS)—essentially, the Fourier transform of the light curve without any phase-dependent component—for AGN and Galactic black hole candidates have been found to have a remarkable property. At high frequencies, their PDS have a break between a $PDS \propto \nu^{-1}$ and a $PDS \propto \nu^{-2}$ component. The frequency where this break occurs (the "break frequency", or ν_b) has been found to correlate well with the black hole mass by $M_{BH} \propto \nu_b^{-1}$ (Markowitz et al.

2003). One should not confuse this with the lower frequency break in XRBs where the PDS changes from PDS $\propto \nu^0$ to $\propto \nu^{-1}$. Overall, high-quality timing observations spanning a useful range of Fourier frequencies, are very rare for most ULXs because of typically rather short individual observations, poor photon statistics, and/or poor and uneven sampling of variability on longer time scales.

However, a method has been developed for determining the mass of black holes based on very little timing data (e.g., Lu and Yu 2001; Nikolajuk et al. 2004; O'Neill et al. 2005). This method could be used with ULXs' sparse timing data and is described in Nikolajuk et al. (2004) as well as below.

Assume one has an X-ray light curve, $f(t)$, with N data points over a time interval T, where $T < 1/\nu_b$. Then one measure the normalized excess variance of these data:

$$\sigma^2_{nxs} = \frac{1}{N\bar{f}(t)} \sum_{i=1}^{N} [(f(t_i) - \bar{f}(t))^2 - \sigma_i^2] \tag{3.1}$$

where $\bar{f}(t)$ is the mean of f and σ_i is error in $f(t_i)$. It is convenient to normalize the PDS to ν_b so that

$$P(\nu) = A\left(\frac{\nu}{\nu_b}\right)^{-2} \ , \ \nu > \nu_b \tag{3.2}$$

where $P(\nu)$ is the PDS and A is a constant. Assuming the overall power of the PDS does not depend on M_{BH}, one gets

$$P_{tot} = \int_{\nu_b}^{\infty} P(\nu)\ d\nu = A\nu_b. \tag{3.3}$$

So this gives the relation between A and ν_b through constant P_{tot}, which is independent of M_{BH} and hence independent of ν_b. Parseval's theorem says that Eqn. 3.1 is equivalent to (e.g., Press et al. 2001)

$$\sigma^2_{nxs} = \int_{1/T}^{1/2\Delta t} P(\nu)\ d\nu \tag{3.4}$$

where Δt is the smallest measureable time interval in the light curve. Because $1/T > \nu_b$, this integral is only over the $P \propto \nu^{-2}$ section of the PDS. Hence, one can write:

$$\sigma^2_{nxs} = \int_{1/T}^{1/2\Delta t} A \left(\frac{\nu}{\nu_b}\right)^{-2} d\nu$$

$$= A\nu_b^2\,[T - 2\Delta t] \tag{3.5}$$

Because $\nu_b \propto M_{BH}$,

$$\sigma^2_{nxs} = \frac{C}{M_{BH}}\,[T - 2\Delta t] \tag{3.6}$$

where C is another constant. Hence, if σ^2_{nxs} is found from a light curve, one can determine M_{BH}. One could normalize this expression (i.e., determine C) by measurements of XRBs and AGN with well-known black hole masses and adequate timing data. This method has been used to estimate M_{BH} for AGN and found the values to be in good agreement with measurements of M_{BH} from other methods (e.g., Lu and Yu 2001; Nikolajuk et al. 2004; O'Neill et al. 2005).

To be sure that $T < 1/\nu_b$, one must observe with small time intervals. For a $10M_\odot$ black hole, $T \lesssim 0.4$ s and for a $500M_\odot$ black hole, $T \lesssim 10$ s (using the relation of Markowitz et al. (2003)). Timing resolution small enough to see timing intervals $\Delta t < T$ is only available with *RXTE* or *ASCA*, and only the former is still operating. *RXTE* data is very limited for ULXs. M82 X-1 and M81 X-9 have been observed by

RXTE for a total of 7.26 ks (Rephaeli and Gruber 2002); two ULXs in IC 342 have been observed for ~ 0.5 Msec with *ASCA* (Sugiho et al. 2001). This method could be applied to these sources. However, high-frequency timing data on others would be needed to determine their mass.

X-ray variability is the easiest way to distinguish between ULXs which are accreting binaries and those that are other sources (supernova remnants or background AGN, for example). ULXs are mostly found in galaxies with active star formation, although some are found in elliptical galaxies (Irwin et al. 2004). However, ULXs that are found in elliptical galaxies have been found to be much less variable than those found in late type galaxies (e.g., Feng and Kaaret 2006), and are unlikely to be accreting binaries. Their distribution within their galaxies gives further evidence for this (Irwin et al. 2004).

3.2.3 Optical Observations

If one could observe the optical variability of a ULX, its mass could be constrained. Unfortunately, merely identifying the optical counterpart to ULXs is difficult or impossible, even for *Chandra*'s spatial resolution. Often, more than one optical counterpart falls within *Chandra*'s or *XMM-Newton*'s error circle. This is the case, e.g., for NGC 1313 X-2 (Mucciarelli et al. 2005), NGC 4559 X-7 (Soria et al. 2005), and for the ULXs found in star clusters (e.g., Wu et al. 2002). However, some ULXs have been identified with an optical counter part, e.g., the ULX in NGC 5204 (Liu et al. 2004), M101 ULX-1 (Kuntz et al. 2005), and NGC 3031 X-11 (Liu et al. 2002). When the secondary has been identified, it has been a high mass star. Galactic X-ray binaries with high mass secondaries have their optical component dominated by the companion star rather than the accretion disk; it is natural to assume the same is true for these ULXs. The possibility that all accreting binary ULXs are found in late type galaxies argues that all accreting binary ULXs have massive secondaries.

Once the optical component of a ULX has been identified, one could observe the optical variability of the source. If the secondary is irradiated by intense radiation by the accretion disk, and assuming the optical light is dominated by the star, this could lead to orbital phase-dependent variability which, for large inclination angles, could be observed (e.g., Phillips and Podsiadlowski 2002). Copperwheat et al. (2005) developed a detailed numerical model of an irradiated star based on radiation transport and equilibrium and included such effects as gravitational distortion and limb darkening. Copperwheat et al. (2007) used this model to more precisely determine the spectral type and mass of various ULX optical companions. Once the period is determined, the mass of the black hole could be constrained. However, magnitude variations would be extremely small and difficult to detect. So far, no periodic optical variability has been detected in any ULX.

Chapter 4

Photon Bubble Model for ULXs

4.1 Introduction

The photon bubble model has been suggested to explain the emission from ULXs. I will make predictions of the X-ray spectra from the photon bubble model of ULXs with the MC/FP code (Chapter 2) coupled with the XSTAR program for X-ray reprocessing in the HDRs (reflection). I will be primarily interested in predictions of spectral features in addition to a warm MCDBB and soft power-law component, although this is not a study of any individual object. In addition I will make predictions of a power-law component that extends above 10 keV which may not be detectable by *Chandra* or *XMM-Newton* but may be by *Suzaku* or future telescopes. The simulations explore 0.5–10 keV luminosities up to $\sim 8 \cdot 10^{39}$ erg s^{-1} which does not include some of the brightest ULXs.

I will describe the Photon Bubble Model in § 4.2. I next describe how I used the solution of Begelman (2002) to set up my simulations (§ 4.3.1) and how I set up the MC/FP code to simulate the emission from this model (§ 4.3.2). Then I will describe the results (§ 4.4) and compare them to other, similar simulations as well as make some simple comparisons with observations (§ 4.5).

4.2 Photon Bubble Model

Arons (1992) proposed the photon bubble model for super-Eddington accretion columns on the poles of magnetized neutron stars; this was partially motivated by the fact that photon bubbles had been observed in radiation hydrodynamic simulations (Klein and Arons 1989, 1991). Later X-ray observations detected key signatures of photon bubbles in magnetized neutron stars (Klein et al. 1996). The photon bubbles of Arons (1992) were driven by "radiation buoyancy", i.e., radiation pressure gradients in a magnetized accretion column. Gammie (1998) modified the solution of Arons (1992) for radiation pressure dominated (radiation pressure much greater than gas pressure) accretion disks and included effects of non-negligible gas pressure. Shaviv (2000) suggested that photon bubbles may be responsible for long-term (~ 20 years) super-Eddington luminosities observed in the nova η Carinae.

Photon bubbles are regions of over and under dense material constrained to move along magnetic field lines. Radiation would be more or less constrained to the tenuous regions, allowing matter to flow inward while being subject to less radiation pressure, thus allowing the disk to exceed the Eddington limit. All photon bubble solutions mentioned above require a strong, stiff magnetic field to constrain plasma motion to one dimension. Begelman (2001) and Begelman (2002) calculated a steady state solution for an inhomogeneous, radiation dominated accretion disk. Based on this model, Begelman (2002) suggested that ULXs are the result of super-Eddington accretion onto solar mass black holes. It is this solution which I have used in determining the disk parameters for my photon bubble simulations later in this chapter.

Inhomogeneous accretion disks have high density regions (HDRs) and low density regions (LDRs) with mass densities ρ_{HDR} and ρ_{LDR}, respectively, with the geometric mean of these given by

$$\bar{\rho} = \sqrt{\rho_{HDR}\rho_{LDR}}. \tag{4.1}$$

In such a disk, most of the mass is confined to the HDRs whereas most of the volume is in the LDRs. In this case, the gravitational pressure will be dominated by the HDRs so that Eqns 1.5 and 1.6 become

$$-\frac{dP}{dr} = \frac{\kappa\bar{\rho}}{c}\frac{L}{4\pi R^2} \tag{4.2}$$

$$\frac{dP}{dr} = \frac{GM\rho_{HDR}}{R^2} \tag{4.3}$$

respectively. Following the derivation of the Eddington flux given in § 1.5 one gets an equation for the flux from an inhomogeneous disk:

$$F = \frac{cGM\delta}{\kappa R^2}\frac{\rho_{HDR}}{\bar{\rho}}. \tag{4.4}$$

Dividing this by the Eddington flux (Eqn. 1.12) gives

$$l = \frac{F}{F_{Edd}} = \frac{\rho_{HDR}}{\bar{\rho}} = \frac{\bar{\rho}}{\rho_{LDR}} = \sqrt{\frac{\rho_{HDR}}{\rho_{LDR}}}. \tag{4.5}$$

So l is the factor by which the local flux can exceed the Eddington limit in an accretion disk with photon bubbles.

Begelman (2006b) has updated the work presented in Begelman (2001, 2002) with a more detailed analysis taking into account a finite optical depth in the vertical structure of the disk. Using this solution in future radiation transfer simulations would be a logical continuation of this work.

4.3 Model Setup

4.3.1 Disk Distribution

Begelman (2002) found the disk parameters relevant to the disk structure to depend on: the black hole mass, $m \equiv M/M_{BH}$; the accretion rate, $\dot{m} = \dot{M}\kappa c/4\pi G M_{BH}$; β, the ratio of the HDR's gas pressure to the magnetic pressure; and α, the Shakura-Sunyaev viscosity parameter. Throughout this chapter I assumed $\beta = 0.1$ and $m = 10$ (resulting in an Eddington luminosity of $1.3 \cdot 10^{39}$ erg s^{-1}).

The Eddington enhancement factor can be related to the number density (see Eqn. 4.5):

$$l = \frac{F}{F_{Edd}} = \frac{n_{HDR}}{\bar{n}} = \frac{3}{2}\frac{\dot{m}D}{\delta r} \tag{4.6}$$

where $\bar{n} = \sqrt{n_{HDR} n_{LDR}}$ is the geometric average of the LDR and HDR number densities. Begelman (2002) derives the following equation for δ:

$$\delta \sim \max\left[0.3\left(\frac{\beta}{0.1}\right)^{-4/13}\left(\frac{\alpha}{0.01}\right)^{-5/13}(\dot{m}D)^{5/13} m^{-1/13} r^{-5/26},\right.$$

$$0.2\left(\frac{\beta}{0.1}\right)^{4/21}\left(\frac{\alpha}{0.01}\right)^{-5/21}(\dot{m}D)^{5/21}m^{-1/21}r^{1/14}\Bigg] \tag{4.7}$$

Note that in Eqn. 4.7 I correct a typographical error in Eqn. 13 of Begelman (2002). The flux dissipated in the Shakura and Sunyaev (1973) α disk model is:

$$F = \frac{3}{2}\frac{c^5}{GM}\alpha\bar{\rho}\delta^3 r^{-3/2}. \tag{4.8}$$

Setting this equation equal to Eqn. 1.12 one can derive an expression for the average density:

$$\bar{n} = 4.8 \cdot 10^{18}\frac{\dot{m}D}{m\alpha}\delta^{-3}r^{-3/2}\,\mathrm{cm}^{-3} \tag{4.9}$$

where $\bar{n} = \bar{\rho}/m_p$. Based on this expression for the average density, and equation 4.6, the following equations were derived for the densities in the HDR and LDR:

$$n_{HDR} = 6.0 \cdot 10^{18}(\dot{m}D)^2(m\alpha)^{-1}\delta^{-4}r^{-5/2}\ \ \mathrm{cm}^{-3} \tag{4.10}$$

$$n_{LDR} = 3.6 \cdot 10^{18}(m\alpha)^{-1}\delta^{-2}r^{-1/2}\ \ \mathrm{cm}^{-3}. \tag{4.11}$$

Although these densities refer to the disk midplane, the Shakura and Sunyaev (1973) solution for a radiation-dominated accretion disk shows that the density will be essentially constant in the vertical direction. Thus, these densities were considered to be the density at the photosphere. The temperature for the HDRs was found by assuming that all the energy is released in the HDRs, and thus, the flux emitted at the photosphere is set equal to the blackbody flux. This gives the Shakura and Sunyaev

(1973) expression:

$$kT_{HDR} = 5.09\ m^{-1/4}(\dot{m}D)^{1/4}r^{-3/4}\ \text{ keV}. \tag{4.12}$$

The "wavelength" of the plane-parallel shocks—i.e., this distance between HDRs—is given by (Begelman 2002)

$$\lambda = \beta\alpha\delta R. \tag{4.13}$$

The proton temperature in the LDRs was found by assuming all of the gravitational energy is converted into heat of the protons:

$$kT_{lp} = \frac{GM_{BH}m_p}{r} \tag{4.14}$$

The electron temperature in the LDR is expected to be significantly lower than the proton temperature due to Compton cooling by radiation from the HDRs. The LDR's electron temperature was determined by implicitly solving a Fokker-Planck equation with the MC/FP code; see § 4.3.2 below. The magnetic field in the LDR was determined by assuming it to be in equipartition with the electrons.

The Eddington ratio is dependent on radius (equation 4.6), so for a given disk, outside of a certain radius (r_{inhom}) $l < 1$, and the disk becomes a homogeneous, Shakura-Sunyaev disk. Outside of this radius, the disk was represented by MCDBB with $kT \propto r^{-3/4}$.

4.3.2 Simulation Description

Equations 4.7 through 4.14 were used to determine the simulation parameters at various radii. To find the total spectrum of the disk, simulations were run at evenly-spaced radii and the results were averaged, weighted by disk area. At each radius, I simulated one individual LDR sandwiched by two HDRs in a plane-parallel geometry (see Fig. 4.1). Within the plane-parallel geometry the LDR is divided into 40 zones, 4 radial and 10 vertical. The fraction of photons which escape is given by the ratio of the escape area to the region's total surface area, which is $\sim 1\%$. Multiple Compton reflections are certainly possible with such a small escape fraction, however for nearly all of the cases presented here, the reflected component was completely drowned out by the blackbody; see below.

The radiation transfer and self-consistent balance between electron heating and cooling within the LDR are simulated with the two-dimensional Monte Carlo/Fokker-Planck (MC/FP) code described in Chapter 2.

Initially, the emission emanating from the HDRs was represented by blackbody spectra inserted at the upper and lower boundaries. A small number of photons were also produced by synchrotron/cyclotron processes in the LDRs. Photons were subjected to Compton scattering and reflection off the HDRs. Escaping photons at the outer boundaries were added to an event file for later spectral extraction.

The proton temperature in the LDR was calculated from equation 4.14, and the electron temperature was calculated numerically within the MC/FP simulation (see

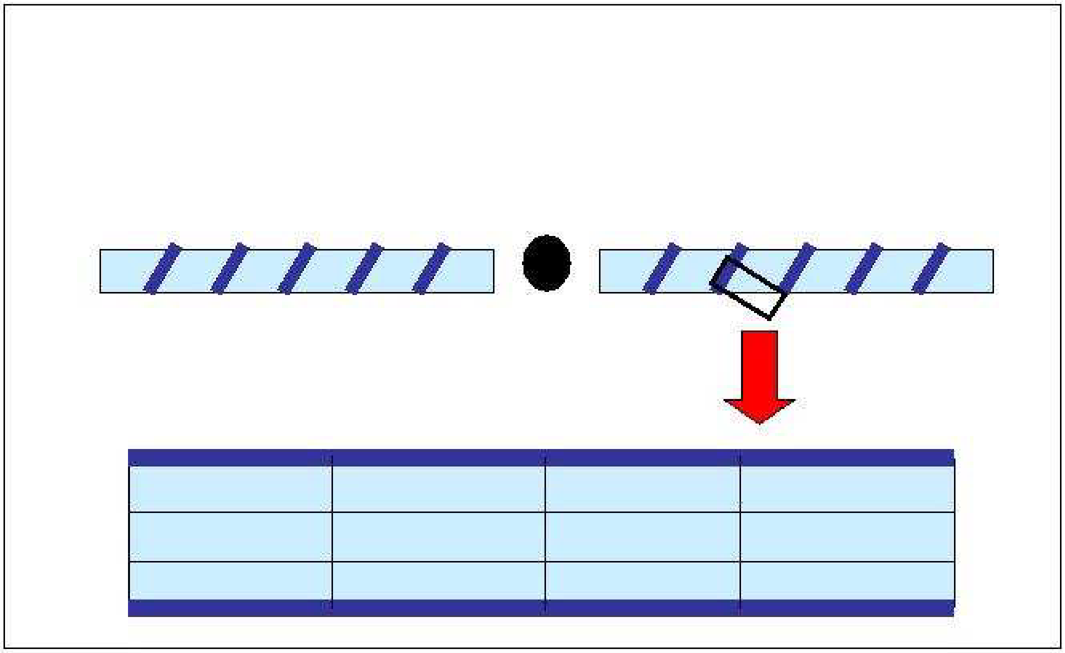

Figure 4.1: The simulation geometry. Each simulation is of one part of the disk, which includes a LDR sandwiched by two HDRs. The LDR is divided into 40 zones. Afterwords, simulations of different parts of the disk are averaged, weighted by area.

§ 2.3.2), which was run until the electron temperature reached a stable equilibrium. The MC/FP simulation was run to extract the photon flux and spectrum incident on the boundaries between the HDRs and the LDR. To calculate the expected spectral features from fluorescence line emission, radiative recombination, and Compton reflection, the impinging spectrum was used as an input into the latest version of XSTAR (Kallman and Bautista 2001). Solar abundances of the most profuse astrophysical elements (H, He, C, Ca, N, O, Ne, Mg, Si, S, Ar, Ca and Fe) were assumed in the HDR, based on Grevesse et al. (1996). XSTAR was run in constant pressure mode; the pressure was calculated from the specified density and the ideal gas law. The main parameter in determining the reflection spectrum's shape and intensity is the ionization parameter:

$$\xi = \frac{4\pi F}{n_{HDR}}. \tag{4.15}$$

Note that XSTAR uses the flux calculated between 1 and 1000 Ry (13.6 eV to 13.6 keV). In order to circumvent XSTAR's limitation to densities $n_e \lesssim 1 \cdot 10^{17}\mathrm{cm}^{-3}$, the impinging flux was re-scaled to keep the ionization ξ at the value corresponding to the physical situation. The inverse flux scaling was applied to the XSTAR output spectrum. Keeping ξ constant ensures that the scaling of a flux dominated by recombination features, $F \propto n_e$ is properly recovered. Testing of XSTAR with various densities but the same ξ seems shows that this is appropriate for the energy range of interest. The resulting reflection spectrum was then added to the intrinsic blackbody from the HDR as boundary sources in a second run of the MC/FP code for the final evaluation of the emanating X-ray spectrum. For an example of a simulation, with spectra at different radii, see Fig. 4.2.

4.4 Results

The simulation parameters and fit results can be seen in Table 4.1. In this table, $\dot{m}$ is the accretion rate, α is the Shakura-Sunyaev viscosity parameter, kT_{in} is the

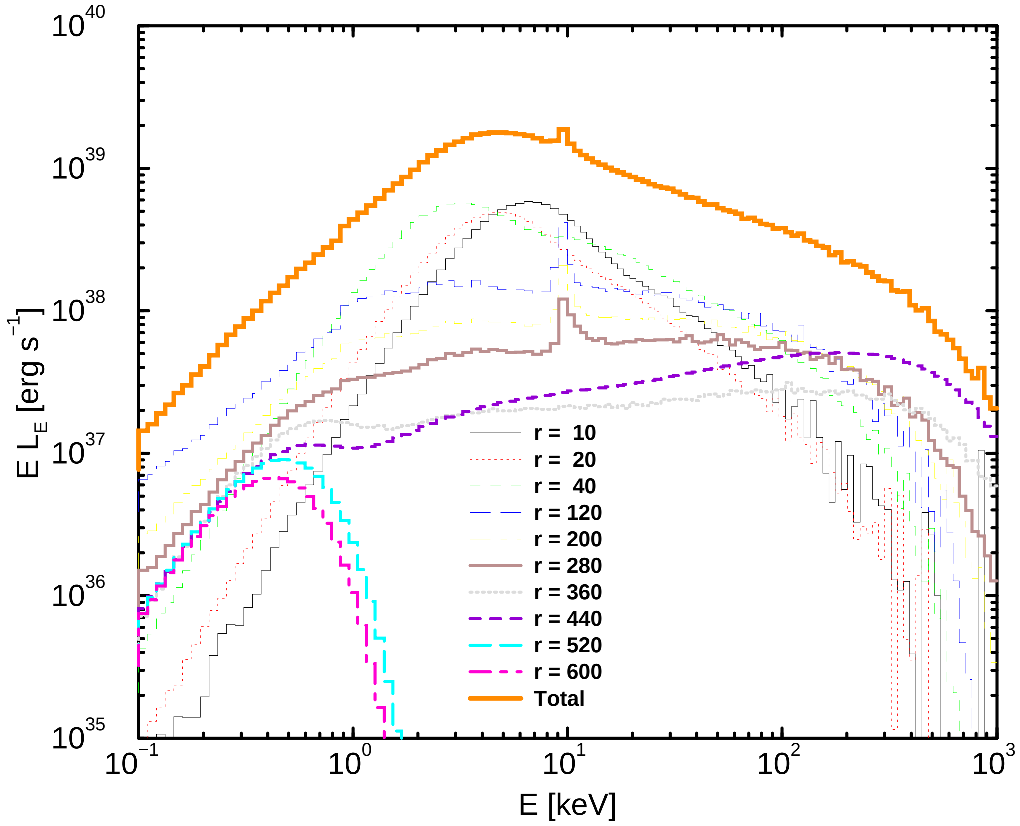

Figure 4.2: Spectra at various radii and the total spectrum for Simulation 2. Similar figures for other simulations can be seen in Appendix C.

inner disk temperature, and r_{inhom} is the radius outside of which photon bubbles cannot exist ($l < 1$). Results of our simulations are: total luminosity over the Eddington luminosity (L_{tot}/L_{Edd}); the 0.2—10 keV luminosity over the Eddington luminosity (L_X/L_{Edd}); the fitted photon index, Γ; the high energy exponential cutoff; and the fraction of the total luminosity in the MCDBB component (f_{BB}), in the Comptonization component (f_{Compt}), and the reflection component (f_{refl}). Note that these do

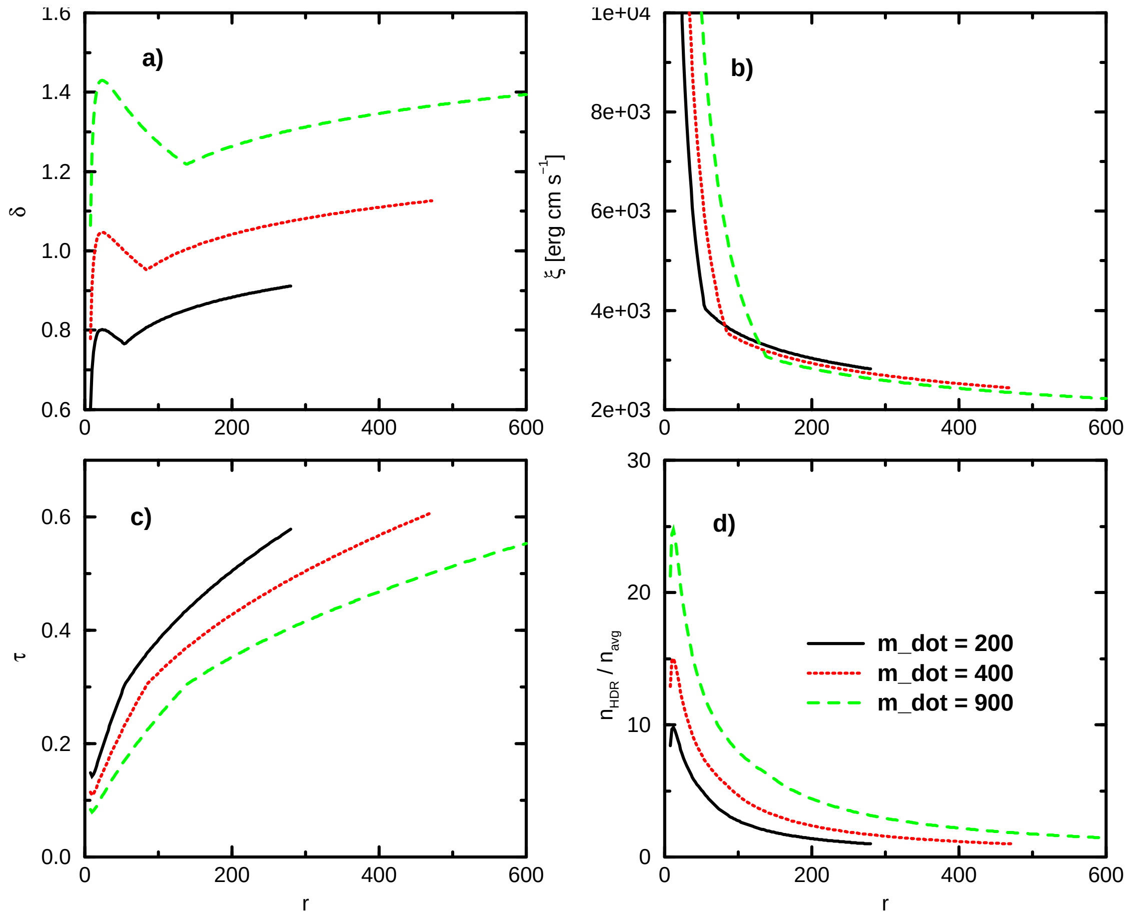

Figure 4.3: The parameters δ (a), ξ (b), τ (c), and l (d) as a function of radius, for $\dot{m} = 200$ (solid black), $\dot{m} = 400$ (dotted red), and $\dot{m} = 900$ (dashed green). These simulations have $\alpha = 0.01$.

not all add up to unity due to rounding. The relevant disk parameters are plotted as a function of radius in Figs. 4.3 to 4.5.

The transition between the expressions for δ (Eqn. 4.7) can be readily seen in panel (a) of Fig. 4.3, with the first expression being used at lower radii. At higher α, the transition occurs at lower radii, or not at all. Note that several simulations

Table 4.1. Simulation and fit parameters; entries are described in the text.

Sim. No.	$\dot{m}$	α	kT_{in} [keV]	r_{inhom}	L_{tot}/L_{Edd}	$L_X/LEdd$	Γ	E_{cutoff} [keV]	f_{BB}	f_{Compt}	f_{refl}
1	200	0.01	1.4	280	2.8	1.3	2.18	460	0.22	0.73	0.05
2	400	0.01	1.6	472	4.4	2.5	2.42	440	0.26	0.63	0.11
3	900	0.01	2.0	860	6.9	4.7	2.42	290	0.56	0.40	0.05
4	200	0.1	1.4	482	5.0	1.7	1.96	280	0.17	0.82	0.01
5	400	0.1	1.6	804	6.5	2.9	2.12	220	0.27	0.74	0.01
6	900	0.1	2.0	1456	9.4	5.3	2.24	140	0.39	0.59	0.02
7	200	0.5	1.4	698	5.8	1.8	1.75	190	0.14	0.85	0.01
8	400	0.5	1.6	1164	8.5	3.1	1.78	160	0.17	0.79	0.05
9	900	0.5	2.0	2100	11.9	5.6	1.95	160	0.31	0.68	0.02

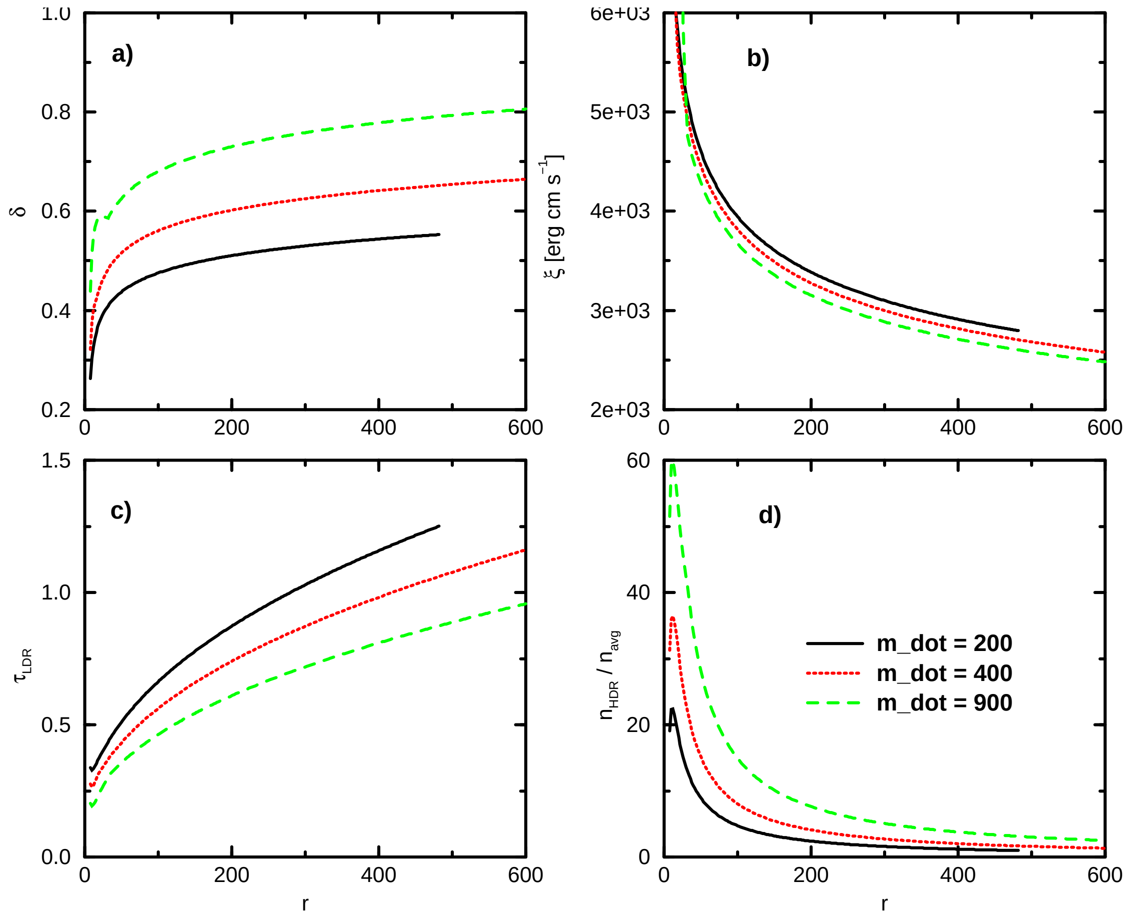

Figure 4.4: Same as Fig. 4.3 except for $\alpha = 0.1$.

violate the thin-disk condition ($\delta < 1$), especially the high $\dot{m}$ and/or low α ones. These solutions should thus be viewed with caution.

The ionization parameter (Eqn. 4.15) is essentially proportional to T^4_{HDR}/n_{HDR}. As both T_{HDR} and n_{HDR} decrease with increasing r, the ionization parameter continually decreases with radius. At no point does it drop below ~ 2000 erg cm s^{-1}, so the reflection component will be small for all cases.

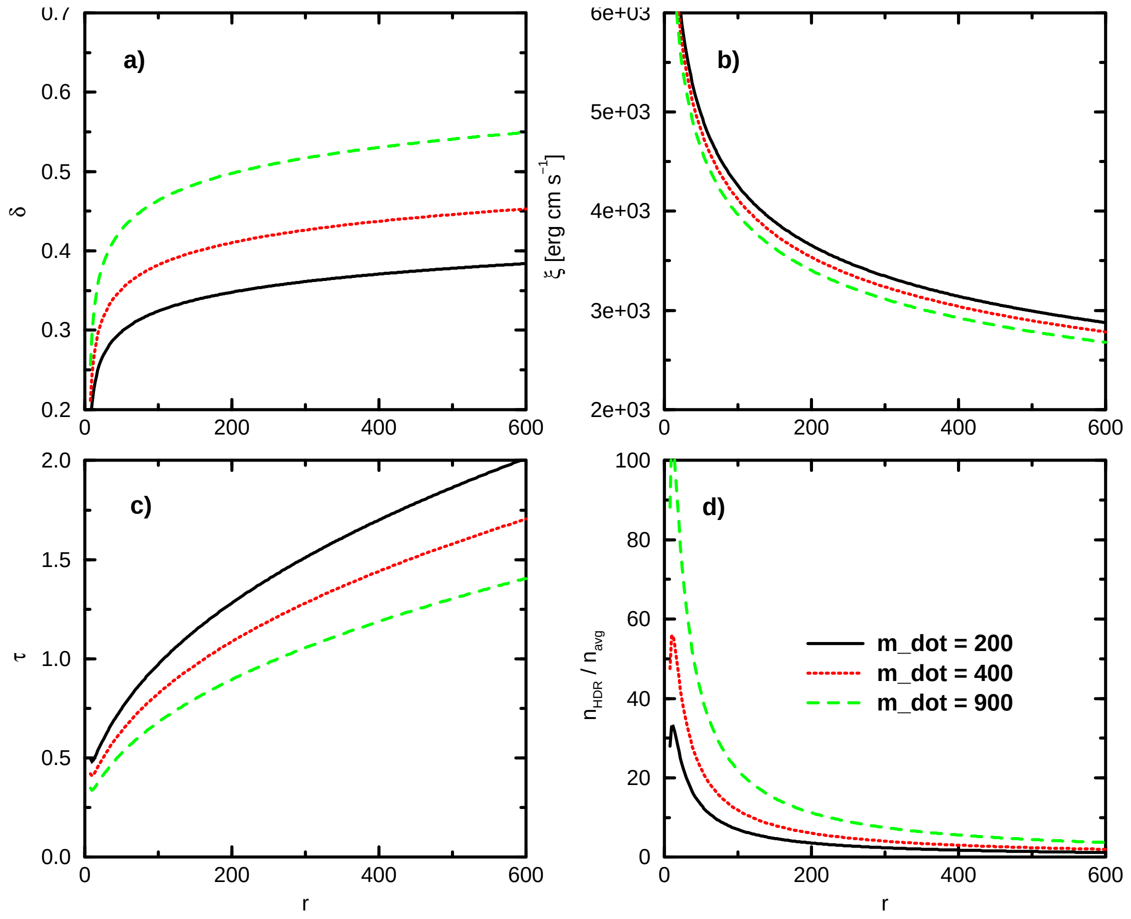

Figure 4.5: Same as Fig. 4.3 except for $\alpha = 0.5$.

The optical depth, τ, is proportional to λn_{LDR}, and is essentially always increasing with r. Thus the spectra have more luminosity from Comptonization at larger radii. It is also larger for smaller accretion rates due to its δ dependence ($\tau \propto \lambda n_{LDR} \propto \delta n_{LDR} \propto \delta^{-1}$) by virtue of δ increasing with increasing $\dot{m}$. Thus one expects a greater Comptonization component for smaller $\dot{m}$. One can see that for our simulations, this is in fact the case (Fig. 4.6). One can also see in Table 4.1 that the fractional power emitted through Comptonization decreases with increasing $\dot{m}$, as expected. This also

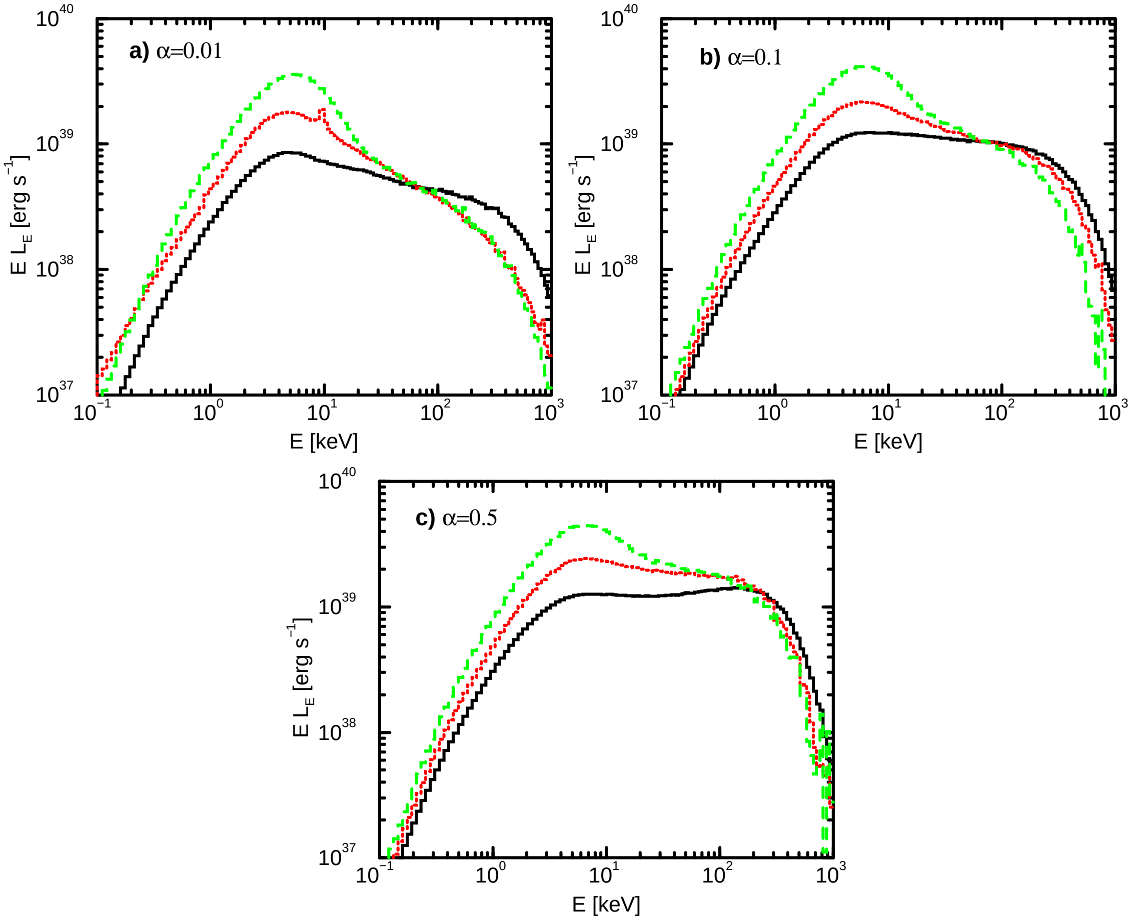

Figure 4.6: Total spectra for (a) $\alpha = 0.01$, (b) $\alpha = 0.1$, and (c) $\alpha = 0.5$. In all graphs are plotted $\dot{m} = 200$ (solid black), $\dot{m} = 400$ (dotted red), and $\dot{m} = 900$ (dashed green).

corresponds to the decrease in Γ, the photon index ($EL_E \propto E^{-\Gamma+2}$) with increasing $\dot{m}$.

The ratio l peaks at $r \sim 12$, as can be seen in panel (d) of Figs. 4.3— 4.5. This is close to where the peak flux is expected in a typical Shakura-Sunyaev accretion disk.

For each simulation, the total reflection component from XSTAR was summed up for all radii. The soft X-ray spectra were fit with a MCDBB. The MCDBB and reflection components were subtracted from the total spectra revealing the Comptonization components. This component was fit with a power-law and exponential cutoff ($EL_E \propto E^{-\Gamma+2}\ e^{-E/E_{cutoff}}$) above 25 keV. The results of this decomposition and fits are summarized in Table 4.1; the individual components for the $\alpha = 0.01$ simulations can be seen in Fig. 4.7. Note that these components are the sum of these components at all radii. The only simulation that has a significant reflection feature visible in its spectrum is Sim. 2 ($\dot{m} = 400$, $\alpha = 0.01$), with a blended Fe XXV/XXVI recombination feature at ~ 9 keV with an equivalent width of ~ 640 eV, and an edge at ~ 0.87 keV (O K). This simulation also has the highest fraction of its emission from the reflection component. One can see in Fig. 4.2 that the reflection component is strongest at $r = 120$—280.

The overall spectra are generally dominated by the high-energy Comptonization component, especially for higher $\dot{m}$. The Comptonization component in many cases extends far down in photon energy into the $\sim$ few keV range and often dominates the total bolometric luminosity, even when the total spectrum appears to be dominated by a thermal soft X-ray component.

This component contributes to the spectra even at low energies, down to $\sim 1\,$keV, as seen in Fig. 4.7. In Fig. 4.2, one can see that the Comptonization component gets stronger at larger radii, as one would expect with the increasing optical depth. This explains the significant Comptonization component to the lower energy part of the spectrum. Eventually, though, one gets to the radius where photon bubbles can no

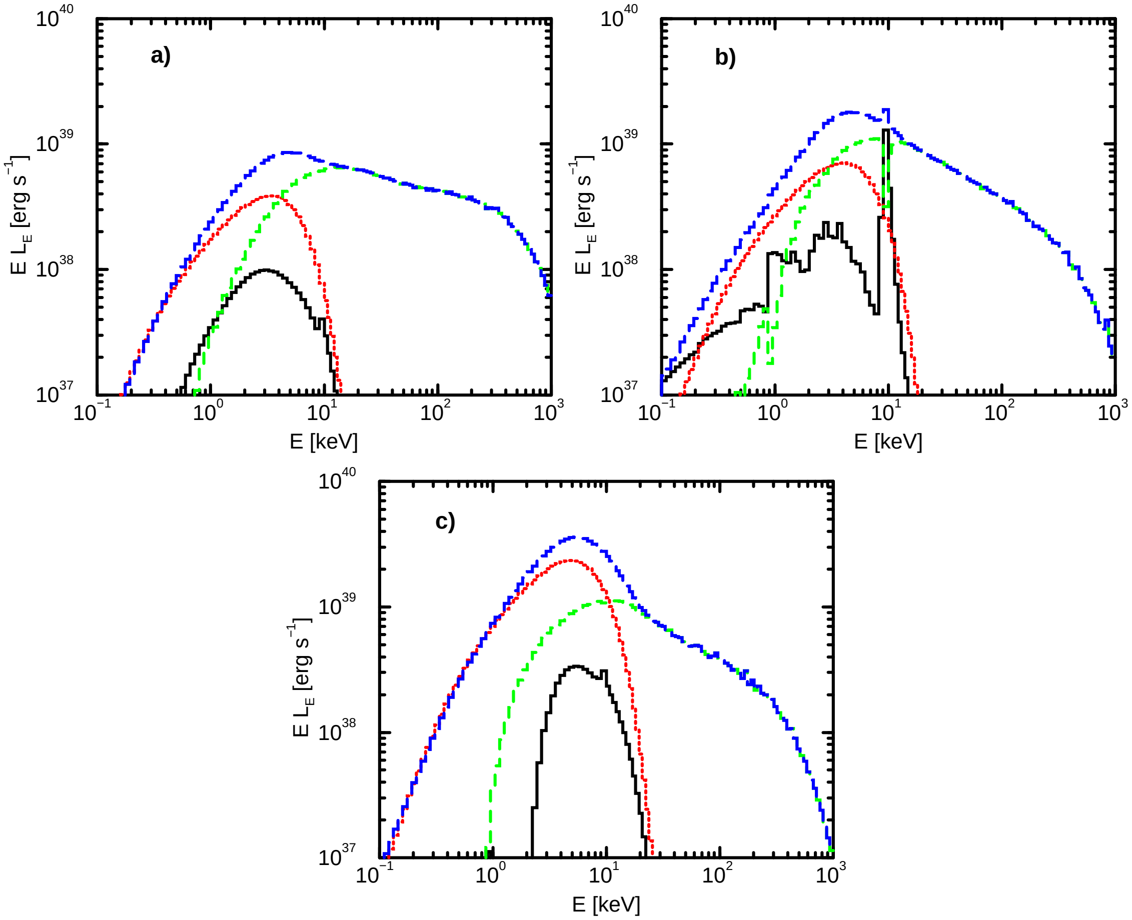

Figure 4.7: The spectra broken into components for $\alpha = 0.01$ and (a) $\dot{m} = 200$, (b) $\dot{m} = 400$, and (c) $\dot{m} = 900$. The solid black line is the reflected component, the dotted red line is the MCDBB, the dashed green line is the Comptonization component, and the long dashed blue line is the total spectrum.

longer be sustained (r_{inhom}), and there is no longer a Comptonization component, as seen in $r > 520$ in Fig. 4.2. Results for other simulations are similar to Fig. 4.2.

Spectral pivoting can be seen in all of the simulations in Fig. 4.6. This is due to the approximately equal luminosity in the Compton components of the different simulations. The energy dissipated in the LDRs is related to the proton temperature, which in our simulations does not depend on accretion rate. This is not an unrealistic assumption, as one would not expect the protons to radiate significantly. However, when the LDRs become more optically thick the energy dissipation becomes more efficient due to multiple Compton scatterings.

4.5 Discussion

Our results are significantly different from previous, similar works. Merloni et al. (2006) perform similar calculations for a low density accretion region with embedded optically thick clumps and considered reflection between these clumps. They used ionization parameters comparable to ours ($\sim$ 3000 erg cm s^{-1}, among others) and achieved much stronger reflection components with no $\sim 9\,$keV feature. This is a consequence of the substantially lower temperature of the soft blackbody (ultraviolet) photons used as an input into the Comptonization scheme in their model: their Comptonization component extends down to $\lesssim 0.1\,$keV energies (in contrast to $\sim$ a few keV in our case). For comparable ξ, calculated from the 1—1000 Ry flux the number of photons above the Fe K edge is thus much smaller than in our case. Therefore, heavy metals are almost fully ionized in most of our simulations, leading to weak or absent line features and a relatively weak Compton reflection component. Ballantyne et al. (2004) explored reflections from a hot corona off of an inhomogeneous disk and found that the spectrum can differ significantly from reflection off a homogeneous disk. They also had stronger reflection features than our results, due to lower ionization parameters, and no $\sim 9\,$keV feature.

Feng and Kaaret (2005) and Stobbart et al. (2006) fit ULXs' X-ray spectra with various models; when fit with a MCDBB or MCDBB and low-energy blackbody, their fits had inner disk temperatures similar to ours. However, we find that our model is unable to explain a soft-excess. I note that no $\sim 9\,\mathrm{keV}$ feature has been detected in the spectra of ULXs, although features at other energies have been detected (Strohmayer and Mushotzky 2003; Agrawal and Misra 2006; Krawczynski et al. 2004; Dewangan et al. 2006a), which could originate from a wind rather than reflection features in the disk. ULX observations above $\sim 10\,\mathrm{keV}$ by *Suzaku* or the next generation of hard X-ray imaging instruments might be able to detect the hard power-laws I predict, although such observations would be difficult.

One may also note that our spectra are similar to the very high state of X-ray binaries such as GX 339-4 (Belloni et al. 2006) and GRO J1655-40 (Saito et al. 2006), which have similar photon indices as found in our simulations. For smaller accretion rates, the photon bubble model may be a viable model to explain the very high state of X-ray binaries.

Since this is an exploratory study, a number of simplifying assumptions have been made. I have assumed a plane-parallel geometry; zones could be corrugated or vary in random ways, which could lead to multiple reflections, increasing the reflection component (Fabian et al. 2002). I have assumed constant densities across LDRs. This may alter the Comptonizing region of the spectra, but probably would not lead to significant differences. I have completely neglected several items. Taking into account

General Relativistic effects could gravitationally broaden the spectrum. However, most of the emission originates at $r \sim 40$, too far out to be greatly affected by GR. I have assumed n_{HDR} and n_{LDR} to be constant in the vertical direction, neglecting color corrections; this may be validated by the more detailed vertical solution of Begelman (2006b), who found that the corrections should be minor. Time variability is beyond the scope of this study and is poorly understood, and thus would involve poorly constrained parameters. It is also possible that the spectra could be modified by further Comptonization in a corona above the disk, which I have also neglected. This would make the spectra even harder than they already are, possibly too hard to match observations. However, recent magnetohydrodynamic simulations have shown difficulties in creating coronae (Hirose et al. 2006) and the photon bubble model may be an alternative to the standard disk-corona geometry. Future simulations could take advantage of more detailed analytic solutions (e.g., Begelman 2006b) and hydrodynamic simulations (e.g., Turner et al. 2005) and could include reprocessing in a corona and/or a disk wind.

Chapter 5

Redshifts of BL Lacertae Objects

5.1 Introduction

Blazars are among the most violent, highly variable astrophysical high-energy phenomena, with rapidly-varying emission from radio through γ-ray energies. They are thought to consist of relativistic jets from supermassive black holes, closely aligned with our line of sight. Several blazars have been the targets for extended multi-wavelength campaigns (e.g., Böttcher et al. 2005; Raiteri et al. 2005; Villata et al. 2004) and a multitude of campaigns on well-known and some less well-observed objects are anticipated for the near future.

BL Lacertae (BL Lac) objects, a subclass of blazars, are defined by their quasar-like continuum and the weakness or absence of broad emission lines in their optical spectra. The spectra are thought to be dominated by nonthermal emission from the highly relativistic jet, masking the contributions of the stars in the host galaxy, and line emission from gas clouds near the supermassive black hole.

There are various models for the source of the nonthermal emission from blazars, and these can be divided into two broad categories: leptonic models, where the radiative processes are dominated by electrons and positrons; and hadronic models, where they are dominated by protons and mesons. Of critical importance in distinguishing between the models is setting the energy scale, on which many parameters (e.g., the jet's speed, density, magnetic field, etc.) depend. This can only be done if the objects' redshifts, and hence distances, are known.

Many well-observed BL Lac objects have unknown or poorly known redshifts based on ∼1–3 emission or absorption lines in low signal-to-noise (S/N) spectra. In several cases, a poorly determined redshift of a BL Lac is repeatedly cited throughout the literature until its reliability is no longer questioned. Thus, a project was undertaken to obtain optical spectra of several of these objects with the 2.4 m Hiltner telescope at the MDM observatory.

Unfortunately, no definitive spectral features were revealed, and thus no definitive redshifts could be assigned. However, using the method of Sbarufatti et al. (2006), I was able to estimate a minimum redshift based on the expected equivalent widths of absorption features in the host galaxy. Imaging campaigns have shown that almost all BL Lacs' host galaxies are ellipticals with approximately the same absolute magnitude (see, e.g., Nilsson et al. 2003; Sbarufatti et al. 2005). Therefore, assuming the host galaxies are standard candles, we estimated the redshifts of several objects based on the observed magnitude of the host galaxies, found from the literature, based on Sbarufatti et al. (2005).

5.2 Observations and Data Analysis

Ohio University purchased a share in the MDM (Michigan-Darthmouth-MIT) observatory in 2004. It is now owned by the University of Michigan, Dartmouth University, the Ohio State University, Columbia University and Ohio University. The observatory is located at Kitt Peak near Tucson, Arizona and consists of the 1.3 m McGraw-Hill telescope and the 2.4 m Hiltner telescope. This chapter makes use of data taken with both telescopes, but primarily the Hiltner.

In §5.2.1 I describe the observations and basic data reduction; the redshift lower-limit procedure is described in §5.2.2. The aperture correction is described in §5.2.3.

5.2.1 Observations

Spectroscopic observations of Six BL Lac objects were taken with the 2.4 m Hiltner telescope in November 2005 and March 2006[1]. Arc lamps and one standard star per night per wavelength setting were also observed for wavelength and spectrophotometric calibration, respectively. The CCDS detector was used with a slit width of $1.5''$ and the 350 grooves/mm grating, giving a spectral resolution of ~ 4.8 Å. The grating provides a wavelength range of 1592 Å. Based on typical BL Lac properties and previous observations of the sources, their redshifts were expected to be a few tenths, and observations within the $4000 - 8500$ Å window could thus be expected

---

[1] Observations in 2005 were done by J. Shields; the 2006 observations were done by J. Shields and myself.

Table 5.1: Blazar observations with Hiltner telescope.

Object	RA (J2000)	Dec (J2000)	Setting	Exp. Time [sec]	Obs. Date (UT)
0219+428	02:22:39.6	+43:02:08	blue	4800	29 Nov. 2005
			green	7200	29 Nov. 2005
			blue	3600	30 Nov. 2005
			red	10800	30 Nov. 2005
0716+714	07:21:53.4	+71:20:36	green	7200	29 Nov. 2005
			blue	5400	30 Nov. 2005
1011+496	10:15:04.1	+49:26:01	blue	7200	26 Mar. 2006
1055+567	10:58:37.7	+56:28:11	blue	7200	26 Mar. 2006
1219+285	12:21:31.7	+28:13:59	blue	5400	26 Mar. 2006
1426+428	14:28:32	+42:40:21	blue	5090	26 Mar. 2006

to probe various strong spectral features in absorption (e.g., Balmer jump, Ca II H and K, Mg b, Na D) and emission (e.g., Hα, Hβ, [O III] 5007). Hence, three different observing settings were used: $\sim 4000 - 5500$ Å (hereafter referred to as the blue setting), $\sim 5500 - 7000$ (green setting) and $\sim 7000 - 8500$ Å (red setting). For the red and green settings, the LG-400 order-blocking filter was used. Unfortunately, weather conditions did not allow observation of all the sources with all of the settings. Seeing during the observations was in the range $\sim 1 - 3''$ with an average of $\sim 1.5''$. On 29 November conditions were nearly photometric; on the other nights, thin cirrus drifted in and out of the field. On 29 November the seeing was $\sim 2''$, and the slit was not consistently aligned with the parallactic angle, leading to noticeable flux losses from atmospheric differential refraction. A summary of the observations can be found in Table 5.1.

The spectra were reduced with IRAF[2] using standard methods. This involved bias-correcting and flat-fielding the two-dimensional spectra, extracting the one-dimensional spectra, wavelength- and flux-calibration, correcting for telluric absorption, and removing bad pixels (such as from cosmic rays). For each object and grating setting, 3-4 spectra were taken, which were then averaged into a single spectrum.

5.2.2 Redshift Limit Procedure

The procedure for finding the minimum redshift of the BL Lac objects is described in Sbarufatti et al. (2006) as well as below.

The equivalent width (EW) of a spectral line is given by:

$$EW = \int \frac{F_{line} - F_{cont}}{F_{cont}} d\lambda \tag{5.1}$$

where F_{cont} is the continuum flux and F_{line} is the line flux. If no spectral features are observed, the minimum EW of a feature one could observe was found. To do this, the spectrum was divided into 20 Å intervals, and the EW was computed for each region, which should be close to zero. This involved interpolating a line over the interval that connected the average of several points on each side of the interval and using this as the continuum. Then the root mean squared EW of all the intervals was computed. EW_{min} was taken to be $3EW_{rms}$. The 20 Å interval size was chosen as

---

[2] IRAF (Image Reduction and Analysis Facility) is distributed by the National Optical Astronomy Observatory which is operated by the Association of Universities for Research in Astronomy, Inc., under cooperative agreement with the National Science Foundation.

this is larger than spectral features one would expect to find, yet smaller than large scale variations resulting from poor flux calibration.

We expect to observe a spectral absorption feature of a given EW from the host galaxy stars, which will be smaller than the EW in the rest frame of the galaxy due to the galaxy emission being overwhelmed by the jet emission. However, there will be an enhancement due to the spectrum being redshifted. The observed EW should thus be given by:

$$EW_{obs} = \frac{(1+z)EW_0}{1+\rho(\lambda)/A(z)} \tag{5.2}$$

where EW_0 is the equivalent width of a line in the rest frame of the galaxy, ρ is the AGN flux to host galaxy flux ratio and $A(z)$ is the aperture correction, which takes into account the fact that not all of the galaxy's emission will be in the extraction aperture. It is the ratio of the integrated surface brightness inside the slit to the total integrated surface brightness of the galaxy. When computing $A(z)$ it was assumed that the galaxy's surface brightness is given by de Vaucouleurs' Law with an effective radius of 10 kpc convolved with a Gaussian point spread function with a FWHM of $1.5''$; for more details on $A(z)$ see §5.2.3. Note that I correct a typographical error in Eqn. 5.2 as found in Sbarufatti et al. (2006).

The ratio $\rho(\lambda)$ can be written as $\rho(\lambda) = \rho_0\Delta(\lambda)$ where ρ_0 is the nucleus to galaxy flux ratio at the central wavelength of the bandpass used, in this case the B band magnitude, and $\Delta(\lambda)$ is the ratio normalized to this value. $\Delta(\lambda)$ was found by dividing a power-law representing the nucleus ($F_\nu \propto \nu^{-\alpha}$ where $\alpha = 1$) by the flux of an elliptical galaxy template from Kinney et al. (1996). At the Ca II $\lambda3934$ feature that we use, $\Delta = 5.1$.

EW_{obs} is set to the minimum EW of a line that is observable in the spectra. Equation 5.2 can be solved for ρ_0:

$$\rho_0 = \frac{A(z)}{\Delta(\lambda)} \left\{ \left[(1+z)\frac{EW_0}{EW_{min}} \right] - 1 \right\} \tag{5.3}$$

Because ρ_0 is a ratio of fluxes, it can be written as the difference between the nucleus and host galaxy absolute magnitudes:

$$\log(\rho_0) = -0.4[M_n(z) - M_h(z)]. \tag{5.4}$$

The absolute nucleus magnitude is:

$$M_n(z) = m_n(z) + 5 - 5\log[d_L(z) - k_n(z)] \tag{5.5}$$

where $d_L(z)$ is the luminosity distance and $k_n(z)$ is the nucleus k-correction, taken from Wisotzki (2000). $m_n(z)$, the apparent magnitude of the nucleus is found by:

$$m_n = -2.5\log[100^{m_{tot}/5} - 100^{m_h(z)/5}] \tag{5.6}$$

where m_{tot} is the total apparent magnitude of the object (host galaxy and nucleus), and $m_h(z)$ is the apparent magnitude of the host, found from the luminosity distance and the absolute magnitude of the host. m_{tot} was found either from simultaneous observations with the 1.3 m McGraw-Hill telescope or derived from the observed spectrum; see below. The host galaxy was assumed to be a standard candle with an absolute B magnitude of $M_h = -20.5 \pm 0.5$ (consistent with Sbarufatti et al. 2005), corrected for evolution:

$$M_h(z) = -20.5 - E(z). \tag{5.7}$$

The evolution correction was taken from Poggianti (1997), modified from the cosmology they used ($q_0 = 0.225$, $H_0 = 50$ km s^{-1} Mpc^{-1}, $\Omega_\Lambda = 0.0$, $t_0 = 15$ Gyr) to the now commonly accepted cosmology ($q_0 = -0.5$, $H_0 = 70$ km s^{-1} Mpc^{-1}, $\Omega_\Lambda = 0.7$, $t_0 = 13$ Gyr).

To find the minimum redshift, Eqns. 5.3 and 5.4 for ρ_0 are plotted, and the z where they intersect is used. In this work, the Ca II λ3934 (blend of H & K) feature was used, with rest frame equivalent width of $EW_0 = 16$ Å which is its equivalent width based on the galaxy template of Kinney et al. (1996).

For the objects 1011+496 and 1055+567, photometric observations on the same night were taken with the McGraw-Hill 1.3 m telescope [3]. These were used to determine m_{tot}, as mentioned above. For the rest of the spectra, m_{tot} was determined by integrating the spectrum weighted by the response function for the B filter using the IRAF utility SBANDS. The spectra for 0219+428 and 0716+714 did not extend over the full bandwidth of the B filter, and so were extrapolated below $\sim$ 4100 Å. The magnitudes of 1011+496 and 1055+567 taken from photometric observations were compared with the magnitudes derived from the spectra and found to vary by less than 0.5 mag. We compared the standard star observation on 26 March with

---

[3] These photometric observations were taken by S. Basu and M. Böttcher.

an exposure of that star aborted due to losing the guide star by heavy cloud cover. The difference was ~ 0.52 magnitudes. Thus, we chose 0.5 as the error for the other objects' spectroscopic magnitudes; although this error has not been derived rigorously, it seems to be reasonable. Spectroscopic magnitudes were also compared with historical light curves and found to be reasonable; 0716+714 and 1219+285 appear to have been observed during high luminosity states. 0716+714 has rarely been observed brighter, with a maximum of $m_B \sim 13.3$ (Stalin et al. 2006), only slightly brighter than our observation; 1219+285 has often been observed brighter (Liu et al. 1995), with a maximum of $m_B \sim 14.4$, significantly brighter than our observation. When determining the minimum redshift, the lower value of the 1σ error bars were used, giving the lowest possible redshift limit.

5.2.3 Aperture Correction

The aperture correction, $A(z)$, is the ratio of the integrated surface brightness inside the extraction aperture to the total integrated surface brightness of the galaxy; i.e.,

$$A(z) = \frac{\int_0^{2\pi} \int_0^{r(\theta)} I^C(R)\ R\ dR\ d\theta}{\int_0^{2\pi} \int_0^{\infty} I^C(R)\ R\ dR\ d\theta}. \tag{5.8}$$

Here θ is the angle measured along the extraction width, and $r(\theta)$ is the distance from the center of the aperture to the edge, for a particular θ. If $r < \theta_{crit}$ then $r = w \cos\theta$, and if $r > \theta_{crit}$ then $r = l/\cos\theta$, where $\theta_{crit} = \arctan(l/w)$, and w and l are the distances on the sky corresponding to half the aperture width and length, respectively. w is found by $w = \phi_w d_L(z)/(1+z)^2$ and l by $l = \phi_l d_L(z)/(1+z)^2$, where ϕ_w and ϕ_l are half the aperture width and length (in this case, $0.75''$ and $4.92''$) and d_L is the luminosity distance.

The host galaxies of all known blazars are elliptical galaxies which have surface brightness profiles well-described by de Vaucouleurs' Law. Thus, I^C—the observed surface brightness inside the aperture— is given by a convolution of de Vaucouleurs' Law and a Gaussian PSF:

$$I^C(R) = \int_0^{2\pi} \int_0^{\infty} \left\{ I(R_e) \exp\left[-7.67 \left(\frac{R'}{R_e} \right)^{1/4} - 1 \right] \right\}$$

$$\times \left\{ \frac{1}{\sigma(z)\sqrt{2\pi}} \exp\left[\frac{-(R-R')^2}{2\sigma(z)^2} \right] \right\} \; R' \; dR' \; d\theta \tag{5.9}$$

where R_e is the effective radius (assumed to be 10 kpc) and $\sigma(z)$ is the Gaussian parameter, derived from the Full Width at Half Maximum by

$$\sigma(z) = \frac{FWHM}{2.3548} \frac{d_L(z)}{(1+z)^2}. \tag{5.10}$$

In this case, the FWHM was assumed to be $1.5''$. The luminosity distance was computed assuming a cosmology with $q_0 = -0.5$, $H_0 = 70$ km s^{-1} Mpc^{-1}, $\Omega_\Lambda = 0.7$, and $t_0 = 13$ Gyr.

5.3 Results

Spectra observed with the 2.4 m Hiltner telescope can be seen in Figs. 5.1 and 5.2. Due to problems in setting the grating tilt, spectra observed on 29-30 November

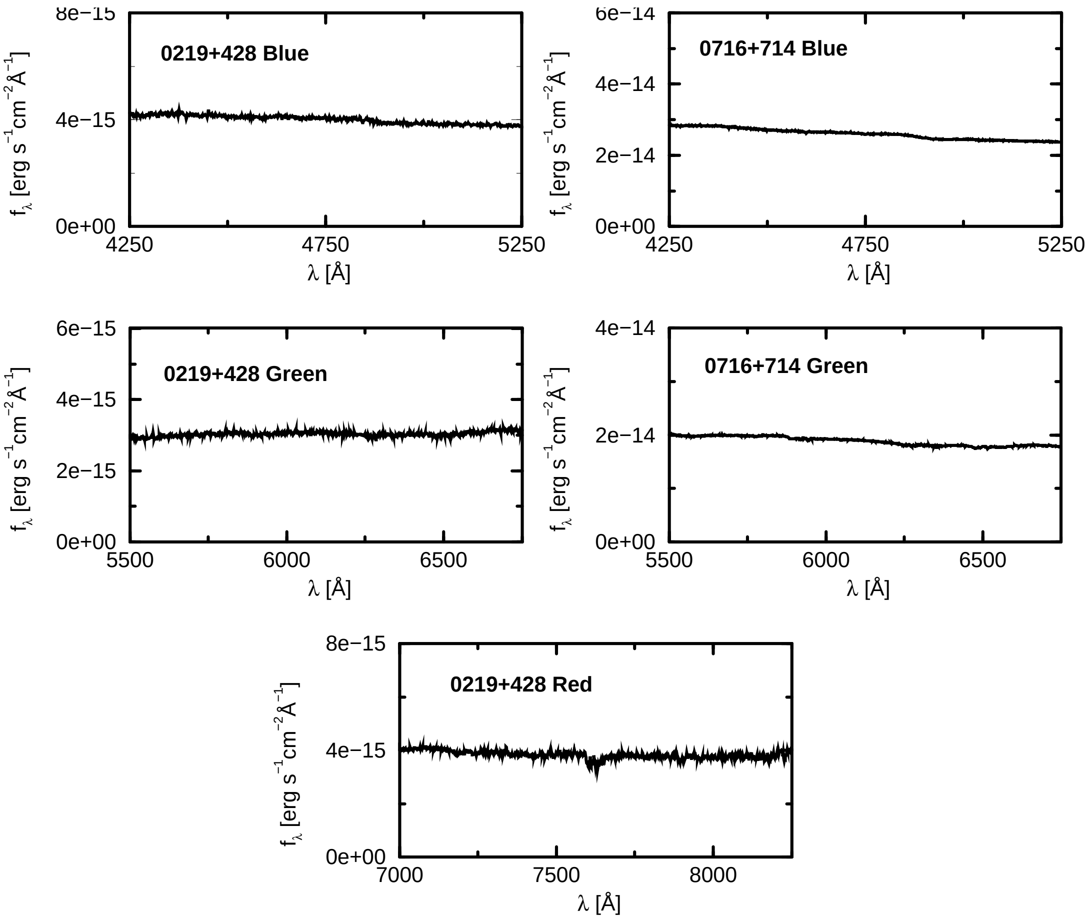

Figure 5.1: Blazar spectra taken in 2005.

were not observed in the intended wavelength range. Results are summarized in Table 5.2. Flux calibration was performed using only one standard star per night, thus the calibration is somewhat suspect. In particular, there is a discontinuity at ~ 4880 Å in spectra taken in 2005 and ~ 4500 Å taken in 2006. Some large-scale structure in the spectra is present that is probably due to residual systematic errors. However, as I am looking for spectral features on much smaller scales, good flux calibration is not critical.

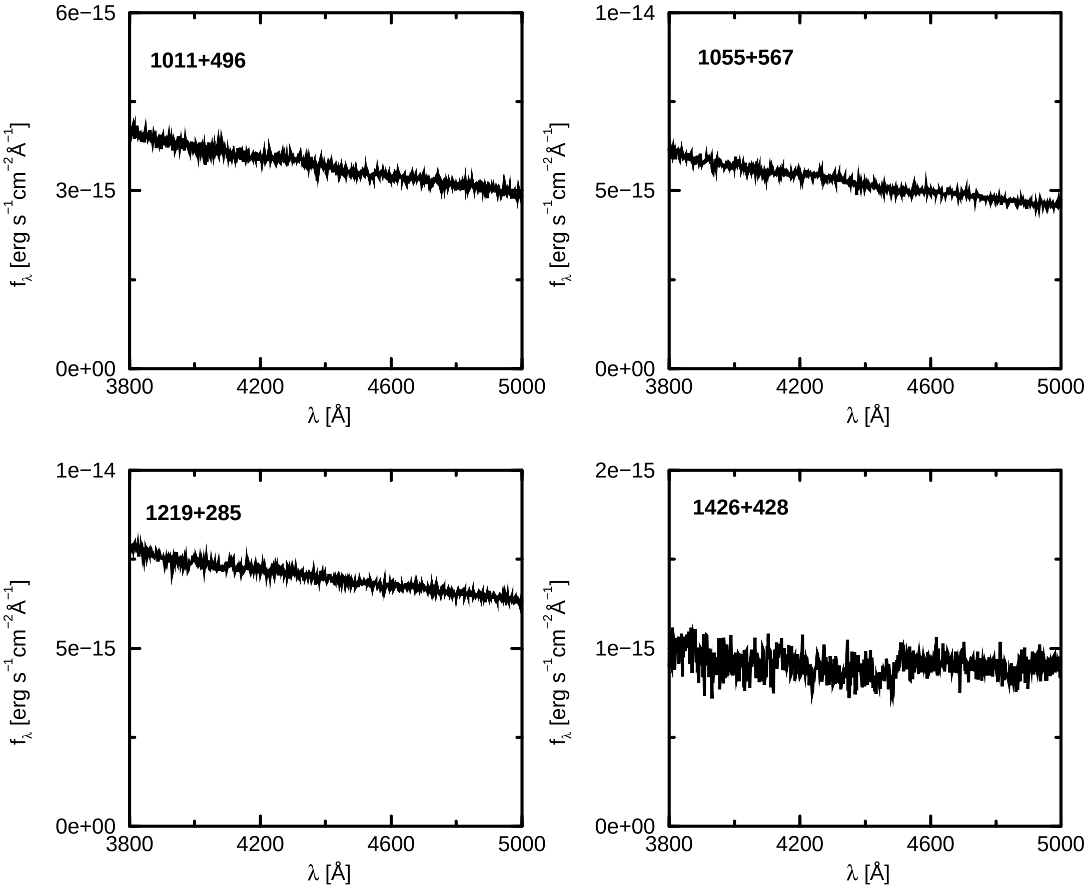

Figure 5.2: Blazar spectra taken in 2006.

Table 5.2: Results of blazar observations.

Object	m_B	S/N	EW_{min} [Å]	z_{spec}	z_{phot}
0219+428	15.35 ± 0.50	90	0.8663	$\geq$0.096	0.321
0716+714	13.39 ± 0.50	270	0.2714	$\geq$0.070	-
1011+496	15.80 ± 0.02	50	0.9981	$\geq$0.134	0.213 ± 0.041
1055+567	15.60 ± 0.02	70	0.7887	$\geq$0.136	-
1219+285	14.88 ± 0.50	90	0.4293	$\geq$0.104	0.161 ± 0.035
1426+428	17.10 ± 0.50	10	3.168	$\geq$0.106	0.132 ± 0.030

A brief description of the previous observations and results for individual objects are discussed below. All error bars quoted are 1σ error bars.

0219+428 (3C 66A) has been the target of a recent multiwavelength campaign (Böttcher et al. 2005) and has been extensively observed in the radio to γ-rays. Its optical spectrum was first observed by Wills and Wills (1974), who found it to be flat and featureless. Observations by Miller et al. (1978) with the Lick 3 m Shane reflector revealed an emission feature at 4044 Å, which they identified as Mg II 2800, giving the object a redshift of $z = 0.444$. However, the feature is located in a region where it is confused with telluric H_2O absorption, and the authors did not consider it reliable. *International Ultraviolet Explorer* observations detected a feature at 1750 Å which could be Lyα emission at a redshift of $z = 0.444$, but the redshift of 0219+428 is still far from certain (Lanzetta et al. 1993). Its host galaxy was marginally resolved by Wurtz et al. (1996), and found to have a magnitude of $r_{Gunn} = 19.0$. Converting to Johnson R using the prescription of Kent (1985) yields $m_R = 18.43$, and thus a photometric redshift of $z = 0.321$. Wurtz et al. (1996) do not provide an error estimate for the magnitude; however, since it was only marginally resolved, the error can be assumed to be high. My spectrum's wavelength range does not cover the range of the Miller et al. (1978) feature, so I am unable to confirm or refute their detection; however, I was able to constrain 0219+428's redshift to $z \geq 0.096$. The 0219+428 green spectra in particular suffered from a non-optimal rotator angle (mentioned above), and may explain the rather dramatic difference in slope from the red and blue spectra. Although I removed most telluric features, I was unable to fully remove the A band feature in the red spectrum.

PKS 0716+714 has been detected in X-rays and γ-rays (see, e.g., Foschini et al. 2006), and could possibly have a precessing jet (Nesci et al. 2005) making it an interesting object. High S/N spectra taken with the KPNO 2.1 m and MMT 6.5 m telescopes are flat and featureless (Rector and Stocke 2001). This thesis' observations also did not reveal any spectral features, and I constrained its redshift to $z \geq 0.070$. The green spectrum of this object was also severely affected by the poor seeing and non-optimal rotator angle. Its host galaxy is unresolved, and Sbarufatti et al. (2005) used this to constrain its redshift to $z \geq 0.52$.

1011+496 has been detected by EGRET (Thompson et al. 1995) and BeppoSAX (Donato et al. 2005) and is a potential target for future multiwavelength campaigns. Its last published spectrum was with the 2.7 m McDonald Observatory using the Intensified Image Dissector Scanner (Machalski 1991). Their spectrum was from 3200 Å to 6000 Å and included an unidentified feature at ~ 3700 Å. Another spectrum with the KPNO 2.1 m telescope from 4400-6500 Å showed no emission or absorption lines. Neither spectrum had a $S/N > 5$. Its redshift is usually quoted as $z = 0.20$, as this is the redshift of the nearby cluster, A950, to which 1011+498 is presumed to belong (Leir and van den Bergh 1977). With my higher S/N spectrum I was also unable to detect any spectral features; however, I could constrain its redshift to $z \geq 0.134$. With its resolved host galaxy magnitude of $m_R = 17.30$ from HST observations (Urry et al. 2000), its photometric redshift can be estimated to be $z = 0.213 \pm 0.041$, in agreement with it being part of the cluster A950. 1011+496 has never had an optical spectrum published beyond 6500 Å.

1055+567 has also been detected by EGRET (Thompson et al. 1995) and BeppoSAX (Donato et al. 2005). Marcha et al. (1996) report a redshift of $z = 0.410$ based on probable detection of the [O III] doublet in MMT spectra. A measurement by Bade et al. (1998) using the WHT, obtained with the source at a comparable flux level, does not appear to confirm the [O III] emission and the authors instead estimate $z = 0.144$ based on Na I D absorption and blended Hα + [N II] emission. However, both features are very weak, and the putative emission feature is additionally suspect since it sits on the wing of the atmospheric A-band absorption feature. The spectrum in this work does not cover the wavelength range of these features, and I can only constrain the redshift to be $z \geq 0.136$. 1055+567 has not had an observation of its host galaxy published, thus I cannot estimate a photometric redshift. It should be noted that, although the $z = 0.144$ value is cited more often in the literature (and is quoted as such in the Simbad database), the $z = 0.410$ redshift is still used as well.

1219+285 (W Comae) has been detected by EGRET (Sreekumar et al. 1996) and is considered a promising target for VHE γ-rays by instruments such as VERITAS or MAGIC. Böttcher et al. (2002) presented several models of its broadband spectral energy distribution. Weistrop et al. (1985) performed spectroscopy on the object with the 4 m KPNO telescope and estimated a redshift of $z = 0.102$ based on [O III] and Hα. However, the spectrum shows strong residuals due to sky subtraction and possibly other problems, and the authors acknowledge the line identifications are uncertain. My high S/N spectrum did not reveal any spectral features, but I did not observe in a range that would allow us to confirm the features detected by Weistrop et al. (1985). Nesci et al. (2001) published a spectrum of the object with the 2.6 m Byurakan Observatory telescope but were unable to confirm the observation of [O III] detected by Weistrop et al. (1985), possibly because they observed the object while it was particularly bright. The host galaxy of 1219+285 was resolved by Nilsson et al. (2003), and they found its magnitude to be $m_R = 16.60 \pm 0.10$. They report that a nearby companion galaxy may be distorting the host galaxy of 1219+285. Based on the Nilsson et al. (2003) measurement, we estimate its photometric redshift to be $z = 0.161 \pm 0.035$, a considerable discrepancy with the spectroscopic value of Weistrop et al. (1985). I could spectroscopically constrain the redshift of 1219+285 to $z \geq 0.104$. It therefore seems unlikely that the Weistrop et al. (1985) redshift of $z = 0.102$ is correct.

1426+428 has been detected at VHE γ-rays by CAT and VERITAS (Djannati-Ataï et al. 2002; Petry et al. 2000) and has been the target of multiwavelength campaigns (Horns 2003). Its only reported optical spectra were published by Remillard et al. (1989). Their highest S/N spectrum ($S/N \sim 10$) with the MDM 1.3 m telescope yielded $z = 0.129$ from marginal detections of Mg I and Na I at ~ 5800 and ~ 6650 Å. Unfortunately, I was not able to achieve a higher S/N spectrum, nor was I able to observe at a wavelength above 5500 Å, thus I could not confirm this observation; I could only constrain its redshift to $z \geq 0.106$. The host galaxy of 1426+428 was resolved by Urry et al. (2000) and found to have $m_R = 16.14$, leading to a photometric redshift of $z = 0.132 \pm 0.030$. Thus, it seems likely the Remillard et al. (1989) redshift is correct.

5.4 Summary

The spectra of six BL Lac objects with poorly known or unknown redshifts have been obtained. For several objects, these spectra have higher S/N than any previously published. Based on this thesis' results, the commonly used redshift for 1219+285 is almost certainly wrong. The questionable Remillard et al. (1989) redshift for 1426+428 has been verified photometrically. The redshifts of the other objects studied remain undetermined.

Chapter 6

Conclusions

6.1 Observing Photon Bubbles

Observing photon bubbles in ULXs could be quite difficult. To observe them in energy ranges which could test the models presented in this dissertation (Chapter 4) may not be possible with present instruments. *Suzaku* is essentially the only current instrument that can observe in the ∼100—1000 keV range, and its poor spatial resolution would make it difficult to distinguish ULXs' X-ray emission from the AGN's. Testing these models in ULXs may have to wait for the next generation X-ray telescopes, e.g., *Constellation-X*. However, observations of AGN radiating at above the Eddington Limit may prove enlightening. For example, Leighly et al. (2006) have observed possible super-Eddington accretion from the quasar PHL 1811, which they speculate may be due to a photon bubble instability in the disk; several other AGN may exhibit super-Eddington accretion (Warner et al. 2004). Comparisons of these AGN's spectral features with ULX spectral features may be a productive area of research.

6.2 The Future of the MC/FP code

The 2-D MC/FP code has been parallelized and is now considerably faster than the serial version. It could be used for continued modeling of photon bubbles in accretion disks. Similar modeling for parameters appropriate for galactic black hole candidates or AGN could be done. It could also be used to model radiation from buoyancy-driven photon bubbles (Arons 1992; Begelman 2006a).

It could be applied to a number of other future accretion problems as well. One possibility is using it to reproduce phase-dependent spectra from XRBs and microquasars. The high energy γ-ray spectra have been shown to be dependent on the binaries' orbital phase for some microquasars such as LS I +61 303 (Albert et al. 2006) which has been modeled as emission from a jet (Gupta and Böttcher 2006). Their spectral modeling includes considerable orbital variability in the hard X-ray spectrum as well. However, the hard X-ray emission of microquasars might not be dominated by a component from the jet, but rather from a Comptonizing corona. The MC/FP code could be used to test whether this model includes significant orbital-phase dependent variability as well, and test if observational signatures in X-ray variability are different from the jet model.

The magneto-rotational instability is generally believed to be the mechanism for transport of angular momentum in an accretion disk, and ample magnetohydrodynamic simulations have been done for this problem (e.g., Fragile et al. 2007); however, radiative transfer simulations have not. The MC/FP code could be used to explore spectral signatures of this instability in a time-independent as well as time-dependent fashion.

Another possibility is further modifying the code to simulate jets in blazars and microquasars. This would involve modifying the code for bulk relativistic motion, physical (adiabatic) expansion of the plasma, and modifying the FP routine for a power-law dominated electron distribution. This would have a considerable advantage over comparable codes for simulating leptonic models of jets (e.g, Böttcher et al. 1997; Gupta et al. 2006) in that it includes many more radiation processes, includes multiple zones, and performs calculations (e.g., Compton scattering and electron evolution) in a much more realistic fashion.

6.3 Blazar Modeling and Monitoring

Clearly there is much more work to be done to determine the redshifts of the blazars observed in this dissertation. Further spectroscopic observations could be done at larger wavelengths to possibly detect spectral features, especially for those objects which have never been observed at these wavelengths (e.g., 1011+496). Observations could be done at the MDM Observatory, where a future observer might be more fortunate with weather conditions, and may observe these objects in a lower-luminosity state, revealing more of the host galaxy. In future observations, it is recommended that the slit be opened to $\sim 2''$, to observe more of the host galaxy. It is unlikely that the loss of spectral resolution for doing this would be critical, especially if observed with the dispersion I used, and the increased S/N will certainly be worth it. Future photometric observations could be used too, in observing the host galaxies of objects such as 0219+428 (3C 66A), which has been only "marginally resolved" (Wurtz et al. 1996) or not resolved at all.

Based on this dissertation's redshift result for 1219+285 (W Comae; Chapter 5), some results may have to be modified. If W Comae is at a redshift of $z = 0.161$ instead of $z = 0.104$, its luminosity distance will be 770 Mpc instead of 470 Mpc (using the standard cosmological model mentioned elsewhere in Chapter 5), and its luminosity will be 2.6 times as great at previously calculated. This may modify the models of Böttcher et al. (2002) for this object. In their models, they found drastically different predictions for very high energy γ-rays ($\gtrsim$ 100 GeV) for fits to lower-energy data, which could be tested by high energy γ-ray Cherenkov telescopes. Observations by *STACEE* have not observed any high energy emission from this object, and have placed constraints on these models (Scalzo et al. 2004) which a more realistic distance may call into question. If a redshift of 0219+428 is determined to be significantly different from its current value, models of this object (Joshi and Böttcher 2007) may have to be revised as well.

Bibliography

V. K. Agrawal and R. Misra. The Unusual Spectrum of the Ultraluminous X-Ray Source M82 X-1. *ApJ*, 638:L83–L86, February 2006.

J. Albert et al. Variable Very-High-Energy Gamma-Ray Emission from the Microquasar LS I +61 303. *Science*, 312:1771–1773, June 2006.

J. Arons. Photon bubbles - Overstability in a magnetized atmosphere. *ApJ*, 388: 561–578, April 1992.

N. Bade, V. Beckmann, N. G. Douglas, P. D. Barthel, D. Engels, L. Cordis, P. Nass, and W. Voges. On the evolutionary behaviour of BL Lac objects. *A&A*, 334: 459–472, June 1998.

D. R. Ballantyne, N. J. Turner, and O. M. Blaes. X-Ray Reflection from Inhomogeneous Accretion Disks. I. Toy Models and Photon Bubbles. *ApJ*, 603:436–448, March 2004.

D. R. Ballantyne, N. J. Turner, and A. J. Young. X-Ray Reflection from Inhomogeneous Accretion Disks. II. Emission-Line Variability and Implications for Reverberation Mapping. *ApJ*, 619:1028–1035, February 2005.

M. C. Begelman. Super-Eddington Atmospheres That Do Not Blow Away. *ApJ*, 551: 897–906, April 2001.

M. C. Begelman. Super-Eddington Fluxes from Thin Accretion Disks? *ApJ*, 568: L97–L100, April 2002.

M. C. Begelman. Nonlinear Photon Bubbles Driven by Buoyancy. *ApJ*, 636:995–1001, January 2006a.

M. C. Begelman. Photon Bubbles and the Vertical Structure of Accretion Disks. *ApJ*, 643:1065–1080, June 2006b.

T. Belloni, I. Parolin, M. Del Santo, J. Homan, P. Casella, R. P. Fender, W. H. G. Lewin, M. Méndez, J. M. Miller, and M. van der Klis. INTEGRAL/RXTE high-energy observation of a state transition of GX 339-4. *MNRAS*, 367:1113–1120, April 2006.

A. M. Beloborodov. Plasma Ejection from Magnetic Flares and the X-Ray Spectrum of Cygnus X-1. *ApJ*, 510:L123–L126, January 1999.

M. Böttcher. *Zeitabhängiger Strahlungstransport in Jets von aktiven galaktischen Kernen.* PhD thesis, University of Bonn, 1997.

M. Böttcher. Coronal Cooling and Its Signatures in the Rapid Aperiodic Variability of Galactic Black Hole Candidates. *ApJ*, 553:960–967, June 2001.

M. Böttcher et al. Coordinated Multiwavelength Observation of 3C 66A during the WEBT Campaign of 2003-2004. *ApJ*, 631:169–186, September 2005.

M. Böttcher, D. R. Jackson, and E. P. Liang. Two-dimensional Monte Carlo/Fokker-Planck Simulations of Flares in Accretion Disk Corona Models. *ApJ*, 586:389–402, March 2003.

M. Böttcher and E. P. Liang. Comptonization Signatures in the Rapid Aperiodic Variability of Galactic Black Hole Candidates. *ApJ*, 506:281–288, October 1998.

M. Böttcher and E. P. Liang. A New Model for the Hard Time Lags in Black Hole X-Ray Binaries. *ApJ*, 511:L37–L40, January 1999.

M. Böttcher and E. P. Liang. Monte Carlo Simulations of Thermal-Nonthermal Radiation from a Neutron Star Magnetospheric Accretion Shell. *ApJ*, 552:248–258, May 2001.

M. Böttcher, E. P. Liang, and I. A. Smith. Radiation feedback in hot accretion-disk corona models and application to GX 339-4. *A&A*, 339:87–94, November 1998.

M. Böttcher, H. Mause, and R. Schlickeiser. γ-ray emission and spectral evolution of pair plasmas in AGN jets. I. General theory and a prediction for the GeV - TeV emission from ultrarelativistic jets. *A&A*, 324:395–409, August 1997.

M. Böttcher, R. Mukherjee, and A. Reimer. Predictions of the High-Energy Emission from BL Lacertae Objects: The Case of W Comae. *ApJ*, 581:143–154, December 2002.

E. Canfield, W. M. Howard, and E. P. Liang. Inverse Comptonization by one-dimensional relativistic electrons. *ApJ*, 323:565–574, December 1987.

B. W. Carroll and D. A. Ostlie. *An Introduction to Modern Astrophysics*. An Introduction to Modern Astrophysics, by B.W. Carroll and D.A. Ostlie. Benjamin Cummings, 1996. ISBN 0-201-54730-9., 1996.

E. J. M. Colbert and R. F. Mushotzky. The Nature of Accreting Black Holes in Nearby Galaxy Nuclei. *ApJ*, 519:89–107, July 1999.

E. J. M. Colbert and A. F. Ptak. A Catalog of Candidate Intermediate-Luminosity X-Ray Objects. *ApJS*, 143:25–45, November 2002.

C. Copperwheat, M. Cropper, R. Soria, and K. Wu. Optical and infrared signatures of ultra-luminous X-ray sources. *MNRAS*, 362:79–88, September 2005.

C. Copperwheat, M. Cropper, R. Soria, and K. Wu. Irradiation models for ULXs and fits to optical data. *MNRAS*, 376:1407–1423, April 2007.

C. D. Dermer and E. P. Liang. Electron thermalization and heating in relativistic plasmas. *ApJ*, 339:512–528, April 1989.

G. C. Dewangan, R. E. Griffiths, M. Choudhury, T. Miyaji, and N. J. Schurch. XMM-Newton View of the Ultraluminous X-Ray Sources in M51. *ApJ*, 635:198–213, December 2005.

G. C. Dewangan, R. E. Griffiths, and A. R. Rao. Quasi-periodic Oscillations and Strongly Comptonized X-Ray Emission from Holmberg IX X-1. *ApJ*, 641:L125–L128, April 2006a.

G. C. Dewangan, L. Titarchuk, and R. E. Griffiths. Black Hole Mass of the Ultraluminous X-Ray Source M82 X-1. *ApJ*, 637:L21–L24, January 2006b.

A. Djannati-Ataï, B. Khelifi, S. Vorobiov, R. Bazer-Bachi, L. M. Chounet, G. Debiais, B. Degrange, P. Espigat, B. Fabre, G. Fontaine, P. Goret, C. Gouiffes, C. Masterson, F. Piron, M. Punch, M. Rivoal, L. Rob, and J.-P. Tavernet. Detection of the BL Lac object 1ES 1426+428 in the Very High Energy gamma-ray band by the CAT Telescope from 1998-2000. *A&A*, 391:L25–L28, August 2002.

D. Donato, R. M. Sambruna, and M. Gliozzi. Six years of BeppoSAX observations of blazars: A spectral catalog. *A&A*, 433:1163–1169, April 2005.

G. Fabbiano. X-ray spectra and large-scale features of two starburst galaxies - NGC 253 and M82. *ApJ*, 330:672–683, July 1988.

G. Fabbiano, A. Zezas, A. R. King, T. J. Ponman, A. Rots, and F. Schweizer. The Time-variable Ultraluminous X-Ray Sources of “The Antennae”. *ApJ*, 584:L5–L8, February 2003.

A. C. Fabian, D. R. Ballantyne, A. Merloni, S. Vaughan, K. Iwasawa, and T. Boller. How the X-ray spectrum of a narrow-line Seyfert 1 galaxy may be reflection-dominated. *MNRAS*, 331:L35–L39, April 2002.

H. Feng and P. Kaaret. XMM-Newton Observations of Ultraluminous X-Ray Sources in Nearby Galaxies. *ApJ*, 633:1052–1063, November 2005.

H. Feng and P. Kaaret. A Comparison of Ultraluminous X-Ray Sources in NGC 1399 and the Antennae Galaxies (NGC 4038/4039). *ApJ*, 653:536–544, December 2006.

J. D. Finke and M. Böttcher. A Library of Fokker-Planck Coefficients for Coulomb Scattering. *PASP*, 117:483–484, May 2005.

A. D. Fokker. Die mittlere Energie rotierender elektrischer Dipole im Strahlungsfeld. *Annalen der Physik*, 348:810–820, 1914.

L. Foschini, G. Tagliaferri, E. Pian, G. Ghisellini, A. Treves, L. Maraschi, F. Tavecchio, G. di Cocco, and S. R. Rosen. Simultaneous X-ray and optical observations of S5 0716+714 after the outburst of March 2004. *A&A*, 455:871–877, September 2006.

P. C. Fragile, P. Anninos, O. M. Blaes, and J. D. Salmonson. 3D Relativistic MHD Simulation of a Tilted Accretion Disk Around a Rapidly Rotating Black Hole. *ArXiv Astrophysics e-prints*, January 2007.

J. Frank, A. King, and D. J. Raine. *Accretion Power in Astrophysics: Third Edition.* Accretion Power in Astrophysics, by Juhan Frank and Andrew King and Derek Raine, pp. 398. ISBN 0521620538. Cambridge, UK: Cambridge University Press, February 2002., February 2002.

C. F. Gammie. Photon bubbles in accretion discs. *MNRAS*, 297:929–935, July 1998.

M. Georganopoulos, F. A. Aharonian, and J. G. Kirk. External Compton emission from relativistic jets in Galactic black hole candidates and ultraluminous X-ray sources. *A&A*, 388:L25–L28, June 2002.

N. Grevesse, A. Noels, and A. J. Sauval. Standard Abundances. In S. S. Holt and G. Sonneborn, editors, *ASP Conf. Ser. 99: Cosmic Abundances*, pages 117–+, 1996.

W. Gropp, E. Lusk, and A. Skjellum. *Using MPI: Portable Parallel Programming with the Message Passing Interface.* MIT Press, Cambridge MA, 2nd edition, 1999.

S. Gupta and M. Böttcher. A Time-dependent Leptonic Model for Microquasar Jets: Application to LS I +61 303. *ApJ*, 650:L123–L126, October 2006.

S. Gupta, M. Böttcher, and C. D. Dermer. Time-dependent Synchrotron and Compton Spectra from Jets of Microquasars. *ApJ*, 644:409–423, June 2006.

C. M. Gutiérrez. Optical Counterparts of Ultraluminous X-Ray Sources. *ApJ*, 640: L17–L20, March 2006.

E. Haug. Electron-positron bremsstrahlung in mildly relativistic thermal plasmas. *A&A*, 148:386–390, July 1985.

S. Hirose, J. H. Krolik, and J. M. Stone. Vertical Structure of Gas Pressure-dominated Accretion Disks with Local Dissipation of Turbulence and Radiative Transport. *ApJ*, 640:901–917, April 2006.

D. Horns. Multi-wavelength Observations of the TeV Blazars Mkn 421, 1ES1959+650, and H1426+428 with the HEGRA Cherenkov Telescopes and the RXTE X-ray Satellite. In L. O. Takalo and E. Valtaoja, editors, *ASP Conf. Ser. 299: High Energy Blazar Astronomy*, pages 13–+, July 2003.

Y. Hui, J. H. Krolik, and I. Hubeny. Non-LTE Spectra of Accretion Disks around Intermediate-Mass Black Holes. *ApJ*, 625:913–922, June 2005.

J. A. Irwin, J. N. Bregman, and A. E. Athey. The Lack of Very Ultraluminous X-Ray Sources in Early-Type Galaxies. *ApJ*, 601:L143–L146, February 2004.

M. Joshi and M. Böttcher. Modeling the Spectral Energy Distribution and Variability of 3C 66A during the WEBT campaign of 2003 – 2004. *ArXiv e-prints*, 704, April 2007.

T. Kallman and M. Bautista. Photoionization and High-Density Gas. *ApJS*, 133: 221–253, March 2001.

V. Kalogera, M. Henninger, N. Ivanova, and A. R. King. An Observational Diagnostic for Ultraluminous X-Ray Sources. *ApJ*, 603:L41–L44, March 2004.

S. M. Kent. Photometry of stars in the uvgr system. *PASP*, 97:165–174, February 1985.

A. R. King, M. B. Davies, M. J. Ward, G. Fabbiano, and M. Elvis. Ultraluminous X-Ray Sources in External Galaxies. *ApJ*, 552:L109–L112, May 2001.

A. L. Kinney, D. Calzetti, R. C. Bohlin, K. McQuade, T. Storchi-Bergmann, and H. R. Schmitt. Template Ultraviolet to Near-Infrared Spectra of Star-forming Galaxies and Their Application to K-Corrections. *ApJ*, 467:38–+, August 1996.

O. Klein and Y. Nishina. Über die Streuung von Strahlung durch freie Elektronen nach der neuen relativistischen Quantendynamik von Dirac. *Z. für Physik*, 52: 853–868, 1929.

R. I. Klein and J. Arons. Time-dependent two dimensional radiation hydrodynamics of accreting matter onto highly magnetized neutron stars. In J. Hunt and B. Battrick, editors, *ESA SP-296: Two Topics in X-Ray Astronomy, Volume 1: X Ray Binaries. Volume 2: AGN and the X Ray Background*, pages 89–98, November 1989.

R. I. Klein and J. Arons. Time-Dependent Two-Dimensional Radiation Hydrodynamics of Accreting Matter onto Highly Magnetized Neutron Stars - the Evolution of Photon Bubbles. In L. Crivellari, I. Hubeny, and D. G. Hummer, editors, *NATO ASIC Proc. 341: Stellar Atmospheres - Beyond Classical Models*, pages 205–+, 1991.

R. I. Klein, J. G. Jernigan, J. Arons, E. H. Morgan, and W. Zhang. GRO J1744-28 and Scorpius X-1: First Evidence for Photon Bubble Oscillations and Turbulence. *ApJ*, 469:L119+, October 1996.

D. E. Knuth. *Seminumerical Algorithms.* Addition Wesley, Reading, MA, 3rd edition, 1997.

A. S. Kompaneets. The Establishment of Thermal Equilibrium between Quanta and Electrons. *Soviet Physics JETP*, 4:730–737, 1957.

E. Körding, H. Falcke, and S. Markoff. Population X: Are the super-Eddington X-ray sources beamed jets in microblazars or intermediate mass black holes? *A&A*, 382: L13–L16, January 2002.

H. Krawczynski, S. B. Hughes, D. Horan, F. Aharonian, M. F. Aller, H. Aller, P. Boltwood, J. Buckley, P. Coppi, G. Fossati, N. Götting, J. Holder, D. Horns, O. M. Kurtanidze, A. P. Marscher, M. Nikolashvili, R. A. Remillard, A. Sadun, and M. Schröder. Multiwavelength Observations of Strong Flares from the TeV Blazar 1ES 1959+650. *ApJ*, 601:151–164, January 2004.

K. D. Kuntz, R. A. Gruendl, Y.-H. Chu, C.-H. R. Chen, M. Still, K. Mukai, and R. F. Mushotzky. The Optical Counterpart of M101 ULX-1. *ApJ*, 620:L31–L34, February 2005.

K. M. Lanzetta, D. A. Turnshek, and J. Sandoval. Ultraviolet spectra of QSOs, BL Lacertae objects, and Seyfert galaxies. *ApJS*, 84:109–184, February 1993.

K. M. Leighly, J. P. Halpern, E. B. Jenkins, D. Grupe, J. Choi, and K. B. Prescott. The Intrinsically X-ray Weak Quasar PHL 1811. I. X-ray Observations and Spectral Energy Distribution. *ArXiv Astrophysics e-prints*, November 2006.

A. A. Leir and S. van den Bergh. Data on 1889 Abell's rich clusters of galaxies. *ApJS*, 34:381–+, July 1977.

E. P. Liang and C. D. Dermer. Interpretation of the gamma-ray bump from Cygnus X-1. *ApJ*, 325:L39–L42, February 1988.

F. K. Liu, G. Z. Xie, and J. M. Bai. A historical light curve of ON 231 and its periodic analysis. *A&A*, 295:1–10, March 1995.

J.-F. Liu, J. N. Bregman, and P. Seitzer. The Optical Counterpart of an Ultraluminous X-Ray Object in M81. *ApJ*, 580:L31–L34, November 2002.

J.-F. Liu, J. N. Bregman, and P. Seitzer. The Optical Counterpart of an Ultraluminous X-Ray Source in NGC 5204. *ApJ*, 602:249–256, February 2004.

Q. Z. Liu and I. F. Mirabel. A catalogue of ultraluminous X-ray sources in external galaxies. *A&A*, 429:1125–1129, January 2005.

Y. Lu and Q. Yu. The relationship between X-ray variability and the central black hole mass. *MNRAS*, 324:653–658, June 2001.

J. Machalski. Radio and optical properties of the GB/GB2 quasar sample. I - Spectroscopy of bright QSO and BL Lac candidates. *Acta Astronomica*, 41:39–47, 1991.

N. Madhusudhan, S. Justham, L. Nelson, B. Paxton, E. Pfahl, P. Podsiadlowski, and S. Rappaport. Models of Ultraluminous X-Ray Sources with Intermediate-Mass Black Holes. *ApJ*, 640:918–922, April 2006.

R. Mahadevan, R. Narayan, and I. Yi. Harmony in Electrons: Cyclotron and Synchrotron Emission by Thermal Electrons in a Magnetic Field. *ApJ*, 465:327–+, July 1996.

K. Makishima, A. Kubota, T. Mizuno, T. Ohnishi, M. Tashiro, Y. Aruga, K. Asai, T. Dotani, K. Mitsuda, Y. Ueda, S. Uno, K. Yamaoka, K. Ebisawa, Y. Kohmura, and K. Okada. The Nature of Ultraluminous Compact X-Ray Sources in Nearby Spiral Galaxies. *ApJ*, 535:632–643, June 2000.

M. J. M. Marcha, I. W. A. Browne, C. D. Impey, and P. S. Smith. Optical spectroscopy and polarization of a new sample of optically bright flat radio spectrum sources. *MNRAS*, 281:425–448, July 1996.

A. Markowitz, R. Edelson, S. Vaughan, P. Uttley, I. M. George, R. E. Griffiths, S. Kaspi, A. Lawrence, I. McHardy, K. Nandra, K. Pounds, J. Reeves, N. Schurch, and R. Warwick. X-Ray Fluctuation Power Spectral Densities of Seyfert 1 Galaxies. *ApJ*, 593:96–114, August 2003.

H. Matsumoto, T. G. Tsuru, K. Koyama, H. Awaki, C. R. Canizares, N. Kawai, S. Matsushita, and R. Kawabe. Discovery of a Luminous, Variable, Off-Center Source in the Nucleus of M82 with the Chandra High-Resolution Camera. *ApJ*, 547:L25–L28, January 2001.

A. Merloni, J. Malzac, A. C. Fabian, and R. R. Ross. On the X-ray spectra of luminous, inhomogeneous accretion flows. *MNRAS*, 370:1699–1712, August 2006.

J. S. Miller, H. B. French, and S. A. Hawley. Optical spectra of BL Lacertae objects. In A. M. Wolfe, editor, *Pittsburgh Conference on BL Lac Objects, Pittsburgh, Pa., April 24-26, 1978, Proceedings. (A79-30026 11-90) Pittsburgh, Pa., University of Pittsburgh, 1978, p. 176-187; Discussion, p. 187-191.*, pages 176–187, 1978.

P. Mucciarelli, L. Zampieri, R. Falomo, R. Turolla, and A. Treves. VLT Observations of the Ultraluminous X-Ray Source NGC 1313 X-2. *ApJ*, 633:L101–L104, November 2005.

S. Nayakshin and F. Melia. Self-consistent Fokker-Planck Treatment of Particle Distributions in Astrophysical Plasmas. *ApJS*, 114:269–288, February 1998.

R. Nesci, E. Massaro, T. Movsessian, and G. Ohanian. Spectroscopic observations of ON 231 (W Com) in a high luminosity state. *Memorie della Societa Astronomica Italiana*, 72:145–146, 2001.

R. Nesci, E. Massaro, C. Rossi, S. Sclavi, M. Maesano, and F. Montagni. The Long-Term Optical Variability of the BL Lacertae Object S5 0716+714: Evidence for a Precessing Jet. *AJ*, 130:1466–1471, October 2005.

M. Nikolajuk, I. E. Papadakis, and B. Czerny. Black hole mass estimation from X-ray variability measurements in active galactic nuclei. *MNRAS*, 350:L26–L30, May 2004.

K. Nilsson, T. Pursimo, J. Heidt, L. O. Takalo, A. Sillanpää, and W. Brinkmann. R-band imaging of the host galaxies of RGB BL Lacertae objects. *A&A*, 400:95–118, March 2003.

P. M. O'Neill, K. Nandra, I. E. Papadakis, and T. J. Turner. The relationship between X-ray variability amplitude and black hole mass in active galactic nuclei. *MNRAS*, 358:1405–1416, April 2005.

M. W. Pakull and L. Mirioni. Bubble Nebulae around Ultraluminous X-Ray Sources. In J. Arthur and W. J. Henney, editors, *Revista Mexicana de Astronomia y Astrofisica Conference Series*, pages 197–199, January 2003.

D. Petry, M. Böttcher, V. Connaughton, A. Lahteenmaki, T. Pursimo, C. M. Raiteri, F. Schröder, A. Sillanpää, G. Sobrito, L. Takalo, H. Teräsranta, G. Tosti, and M. Villata. Multiwavelength Observations of Markarian 501 during the 1997 High State. *ApJ*, 536:742–755, June 2000.

S. N. Phillips and P. Podsiadlowski. Irradiation pressure effects in close binary systems. *MNRAS*, 337:431–444, December 2002.

M. Planck. Über einen Satz der statistichen Dynamik und eine Erweiterung in der Quantumtheorie. *Sitzungberichte der Preussischen Akadademie der Wissenschaften*, 24:324–341, May 1917.

B. M. Poggianti. K and evolutionary corrections from UV to IR. *A&AS*, 122:399–407, May 1997.

L. A. Pozdniakov, I. M. Sobol, and R. A. Siuniaev. Comptonization and the shaping of X-ray source spectra - Monte Carlo calculations. *Astrophysics and Space Physics Reviews*, 2:189–331, 1983.

W. Press, S. Teukolsky, W. Vetterling, and B. Flannery. *Numerical Recipes in Fortran.* Cambridge University Press, Cambridge, 2nd edition, 2001.

C. M. Raiteri et al. The WEBT campaign to observe AO 0235+16 in the 2003-2004 observing season. Results from radio-to-optical monitoring and XMM-Newton observations. *A&A*, 438:39–53, July 2005.

T. A. Rector and J. T. Stocke. The Properties of the Radio-Selected 1 Jy Sample of BL Lacertae Objects. *AJ*, 122:565–584, August 2001.

R. A. Remillard, I. R. Tuohy, R. J. V. Brissenden, D. A. H. Buckley, D. A. Schwartz, E. D. Feigelson, and S. Tapia. Two X-ray-selected BL Lacertae objects observed with the HEAO 1 scanning modulation collimator. *ApJ*, 345:140–147, October 1989.

Y. Rephaeli and D. Gruber. RXTE view of the starburst galaxies M 82 and NGC 253. *A&A*, 389:752–760, July 2002.

T. P. Roberts, R. E. Kilgard, R. S. Warwick, M. R. Goad, and M. J. Ward. Chandra monitoring observations of the ultraluminous X-ray source NGC 5204 X-1. *MNRAS*, 371:1877–1890, October 2006.

G. B. Rybicki and A. P. Lightman. *Radiative Processes in Astrophysics.* New York, Wiley-Interscience, 1979. 393 p., 1979.

K. Saito, K. Yamaoka, M. Fukuyama, T. G. Miyakawa, A. Yoshida, and J. Homan. RXTE spectra of the Galactic microquasar GRO J1655-40 during the 2005 outburst. In *VI Microquasar Workshop: Microquasars and Beyond*, 2006.

B. Sbarufatti, A. Treves, and R. Falomo. Imaging Redshifts of BL Lacertae Objects. *ApJ*, 635:173–179, December 2005.

B. Sbarufatti, A. Treves, R. Falomo, J. Heidt, J. Kotilainen, and R. Scarpa. ESO Very Large Telescope Optical Spectroscopy of BL Lacertae Objects. II. New Redshifts, Featureless Objects, and Classification Assessments. *AJ*, 132:1–19, July 2006.

R. A. Scalzo, L. M. Boone, D. Bramel, J. Carson, C. E. Covault, P. Fortin, G. Gauthier, D. M. Gingrich, D. Hanna, A. Jarvis, J. Kildea, T. Lindner, C. Mueller, R. Mukherjee, R. A. Ong, K. J. Ragan, D. A. Williams, and J. Zweerink. High-Energy Gamma-Ray Observations of W Comae with the Solar Tower Atmospheric Cerenkov Effect Experiment (STACEE). *ApJ*, 607:778–787, June 2004.

R. Schlickeiser. A viable mechanism to establish relativistic thermal particle distribution functions in cosmic sources. *A&A*, 143:431–434, February 1985.

N. I. Shakura and R. A. Sunyaev. Black holes in binary systems. Observational appearance. *A&A*, 24:337–355, 1973.

N. J. Shaviv. The Porous Atmosphere of η Carinae. *ApJ*, 532:L137–L140, April 2000.

R. Soria, M. Cropper, M. Pakull, R. Mushotzky, and K. Wu. The star-forming environment of an ultraluminous X-ray source in NGC4559: an optical study. *MNRAS*, 356:12–28, January 2005.

P. Sreekumar, D. L. Bertsch, B. L. Dingus, J. A. Esposito, C. E. Fichtel, J. Fierro, R. C. Hartman, S. D. Hunter, G. Kanbach, D. A. Kniffen, Y. C. Lin, H. A. Mayer-Hasselwander, J. R. Mattox, P. F. Michelson, C. von Montigny, R. Mukherjee, P. L.

Nolan, E. Schneid, D. J. Thompson, and T. D. Willis. EGRET Observations of the North Galactic Pole Region. *ApJ*, 464:628–+, June 1996.

C. S. Stalin, Gopal-Krishna, R. Sagar, P. J. Wiita, V. Mohan, and A. K. Pandey. Multiband optical monitoring of the blazars S5 0716+714 and BL Lacertae. *MNRAS*, 366:1337–1345, March 2006.

A.-M. Stobbart, T. P. Roberts, and J. Wilms. XMM-Newton observations of the brightest ultraluminous X-ray sources. *MNRAS*, 368:397–413, May 2006.

T. E. Strohmayer and R. F. Mushotzky. Discovery of X-Ray Quasi-periodic Oscillations from an Ultraluminous X-Ray Source in M82: Evidence against Beaming. *ApJ*, 586:L61–L64, March 2003.

M. Sugiho, J. Kotoku, K. Makishima, A. Kubota, T. Mizuno, Y. Fukazawa, and M. Tashiro. A Possible X-Ray Periodicity at Several Tens of Hours of an Ultraluminous Compact X-Ray Source in IC 342. *ApJ*, 561:L73–L76, November 2001.

R. A. Sunyaev and Y. B. Zeldovich. The Interaction of Matter and Radiation in the Hot Model of the Universe. *Ap&SS*, 7:20–+, 1970.

Y. Terashima and A. S. Wilson. The Luminous X-Ray Source Population in M51 Observed with Chandra. *ApJ*, 601:735–758, February 2004.

D. J. Thompson, D. L. Bertsch, B. L. Dingus, J. A. Esposito, A. Etienne, C. E. Fichtel, D. P. Friedlander, R. C. Hartman, S. D. Hunter, D. J. Kendig, J. R.

Mattox, L. M. McDonald, C. von Montigny, R. Mukherjee, P. V. Ramanamurthy, P. Sreekumar, J. M. Fierro, Y. C. Lin, P. F. Michelson, P. L. Nolan, S. K. Shriver, T. D. Willis, G. Kanbach, H. A. Mayer-Hasselwander, M. Merck, H.-D. Radecke, D. A. Kniffen, and E. J. Schneid. The Second EGRET Catalog of High-Energy Gamma-Ray Sources. *ApJS*, 101:259–+, December 1995.

N. J. Turner, O. M. Blaes, A. Socrates, M. C. Begelman, and S. W. Davis. The Effects of Photon Bubble Instability in Radiation-dominated Accretion Disks. *ApJ*, 624: 267–288, May 2005.

C. M. Urry, R. Scarpa, M. O'Dowd, R. Falomo, J. E. Pesce, and A. Treves. The Hubble Space Telescope Survey of BL Lacertae Objects. II. Host Galaxies. *ApJ*, 532:816–829, April 2000.

M. Villata et al. The WEBT BL Lacertae Campaign 2001 and its extension. Optical light curves and colour analysis 1994-2002. *A&A*, 421:103–114, July 2004.

C. Warner, F. Hamann, and M. Dietrich. Active Galactic Nucleus Emission-Line Properties Versus the Eddington Ratio. *ApJ*, 608:136–148, June 2004.

D. Weistrop, P. Hintzen, D. B. Shaffer, and W. Romanishin. Optical and radio observations for the BL Lacertae objects 1219 + 28, 0851 + 202, and 1400 + 162. *ApJ*, 292:614–619, May 1985.

B. J. Wills and D. Wills. C 66A: a Bright New Quasi-Stellar Object. *ApJ*, 190:L97+, June 1974.

L. M. Winter, R. F. Mushotzky, and C. S. Reynolds. XMM-Newton Archival Study of the Ultraluminous X-Ray Population in Nearby Galaxies. *ApJ*, 649:730–752, October 2006a.

L. M. Winter, R. F. Mushotzky, and C. S. Reynolds. XMM-Newton Archival Study of the Ultraluminous X-Ray Population in Nearby Galaxies. *ApJ*, 649:730–752, October 2006b.

L. Wisotzki. Quasar spectra and the K correction. *A&A*, 353:861–866, January 2000.

B. Wolfe and F. Melia. Covariant Kinetic Theory with an Application to the Coma Cluster. *ApJ*, 638:125–137, February 2006.

H. Wu, S. J. Xue, X. Y. Xia, Z. G. Deng, and S. Mao. The Nature of Ultraluminous X-Ray Sources in NGC 4565. *ApJ*, 576:738–744, September 2002.

R. Wurtz, J. T. Stocke, and H. K. C. Yee. The Canada-France-Hawaii Telescope Imaging Survey of BL Lacertae Objects. I. Properties of the Host Galaxies. *ApJS*, 103:109–+, March 1996.

A. A. Zdziarski and M. Gierliński. Radiative Processes, Spectral States and Variability of Black-Hole Binaries. *Progress of Theoretical Physics Supplement*, 155:99–119, 2004.

Appendix A

Radiation Pressure Gradient

In this appendix I will derive Eqn. 1.5.

The radiation transfer equation for a spherical gas cloud can be written as

$$-\frac{\cos\theta}{\kappa\rho}\frac{dI_\lambda}{dR} = I_\lambda - S_\lambda \tag{A.1}$$

where I_λ is the intensity, S_λ is the source function, ρ is the mass density of the accreting gas, κ is the opacity, R is the radial coordinate and θ is the angle between R and the direction of a photon's travel. One can multiply both sides by $\cos\theta$ and integrate over all wavelengths and solid angles to get:

$$-\frac{1}{\kappa\rho}\frac{d}{dR}\int I_\lambda\ \cos^2\theta\ d\lambda\ d\Omega = \int I_\lambda\ \cos\theta\ d\lambda\ d\Omega - \int S_\lambda\ \cos\theta\ d\lambda\ d\Omega. \tag{A.2}$$

For a spherical distribution, the integral on the left side of Eqn. A.2 is equal to cP_{rad}, where P_{rad} is the radiation pressure. The first integral on the right hand side is the radiative flux, $L/4\pi R^2$, while the second is simply 0. Thus,

$$-\frac{c}{\kappa\rho}\frac{dP_{rad}}{dR} = \frac{L}{4\pi R^2}, \tag{A.3}$$

or

$$-\frac{dP_{rad}}{dR} = \frac{\kappa\rho}{c}\frac{L}{4\pi R^2} \tag{A.4}$$

which is Eqn. 1.5.

Appendix B

Sample Simulation Input Files

This appendix contains example input files for the MC/FP code. Below is a sample of the main input file, “input.dat”. It has been slightly modified to fit on the page.

```
      NUMBER OF Z BOUNDARIES                          nz = 4
      NUMBER OF R BOUNDARIES                          nr = 5
      Upper z boundary [cm]                        z(nz) = 2.22e4
    Lower r boundary [cm]                           rmin = 2.95d9
    Upper r boundary [cm]                          r(nr) = 2.95200d9
    Let upper surface source be a star?
           (1=star, 0=no star)               star_switch = 0
    Time to stop simulation [s]:                   tstop =  6.e-3
    Maximum time step [s]:                         dtmax = 8.d-1
    Number of time steps for boundary
           temperature inputs:                      ntime = 1
    Beginning of time step 1 [s]:                   t0(1) = 1.d0
    End of time step 1 [s]:                         t1(1) = 1.d0
 Boundary temp. of the upper boundary,
           radial zone  1, time 1:              tbbu( 1,1) = 0.283d0
 Boundary temp. of the lower boundary,
           radial zone  1, time 1:              tbbl( 1,1) = 0.283d0
 Boundary temp. of the upper boundary,
           radial zone  2, time 1:              tbbu( 2,1) = 0.283d0
 Boundary temp. of the lower boundary,
           radial zone  2, time 1:              tbbl( 2,1) = 0.283d0
 Boundary temp. of the upper boundary,
           radial zone  3, time 1:              tbbu( 3,1) = 0.283d0
 Boundary temp. of the lower boundary,
           radial zone  3, time 1:              tbbl( 3,1) = 0.283d0
 Boundary temp. of the upper boundary,
           radial zone  4, time 1:              tbbu( 4,1) = 0.283d0
 Boundary temp. of the lower boundary,
           radial zone  4, time 1:              tbbl( 4,1) = 0.283d0
 Boundary temp. of the upper boundary,
```

```
          radial zone  5, time 1:              tbbu( 5,1) = 0.283d0
Boundary temp. of the lower boundary,
          radial zone  5, time 1:              tbbl( 5,1) = 0.283d0
BOUNDARY TEMPERATURE OF THE INNER BOUNDARY,
          vert. zone 1, time 1:                 tbbi(1,1) = 0.d0
BOUNDARY TEMPERATURE OF THE OUTER BOUNDARY,
          vert. zone 1, time 1:                 tbbo(1,1) = 0.d0
BOUNDARY TEMPERATURE OF THE INNER BOUNDARY,
          vert. zone 2, time 1:                 tbbi(2,1) = 0.d0
BOUNDARY TEMPERATURE OF THE OUTER BOUNDARY,
          vert. zone 2, time 1:                 tbbo(2,1) = 0.e0
BOUNDARY TEMPERATURE OF THE INNER BOUNDARY,
          vert. zone 3, time 1:                 tbbi(3,1) = 0.e0
BOUNDARY TEMPERATURE OF THE OUTER BOUNDARY,
          vert. zone 3, time 1:                 tbbo(3,1) = 0.e0
BOUNDARY TEMPERATURE OF THE INNER BOUNDARY,
          vert. zone 4, time 1:                 tbbi(4,1) = 0.e0
BOUNDARY TEMPERATURE OF THE OUTER BOUNDARY,
          vert. zone 4, time 1:                 tbbo(4,1) = 0.e0
Spectra incident on upper and lower boundaries?
          (0=no,1=yes)                        spec_switch = 0
Number of photon regions                           nphreg = 3
Minimum Energy of the photon in region 1        Ephmin(1) = 1.d-3
Maximum Energy of the photon in region 1        Ephmax(1) = 1.d0
Number of photon energy bins in region 1       nphbins(1) = 25
Minimum Energy of the photon in region 2        Ephmin(2) = 1.d0
Maximum Energy of the photon in region 2        Ephmax(2) = 2.d1
Number of photon energy bins in region 2       nphbins(2) = 40
Minimum Energy of the photon in region 3        Ephmin(1) = 2.d1
Maximum Energy of the photon in region 3        Ephmax(1) = 1.d3
Number of photon energy bins in region 3       nphbins(1) = 30
Observation angle (number of mu-bins)                 nmu = 2
Number of energy bins in for light curves          nph_lc = 5
Lower boundary of Light Curve Energy Bin        Elcmin(1) = 0.1
Upper boundary of the Light Curve Energy Bin    Elcmax(1) = 1.d0
Lower boundary of Light Curve Energy Bin        Elcmin(2) = 1.d0
Upper boundary of the Light Curve Energy Bin    Elcmax(2) = 3.d0
Lower boundary of Light Curve Energy Bin        Elcmin(3) = 3.d0
Upper boundary of the Light Curve Energy Bin    Elcmax(3) = 1.d1
Lower boundary of Light Curve Energy Bin        Elcmin(4) = 1.d1
Upper boundary of the Light Curve Energy Bin    Elcmax(4) = 5.d1
Lower boundary of Light Curve Energy Bin        Elcmin(5) = 5.d1
```

```
Upper boundary of the Light Curve Energy Bin    Elcmax(5) = 5.d2
File name for time-integrated energy spectra:      spname = sp/
                                                    spbM10LDR20.dat
File name for time-integrated photon spectra:      phname = ph/
                                                    phbM10LDR20.dat
File name for light curves in
          angular bin no. 1:                    lcname(1) = lc/
                                                 lcbM10LDR20_01.dat
File name for census file 1:                    census(1) =
                                                        census1.dat
File name for census file 2:                    census(2) =
                                                        census2.dat
File name for event file:                       eventfile =
                                                    evbM10LDR20.dat
File name for electron temperature history:     temp_file = temp/
                                                 temp_bM10LDR20.dat
Particle number per photon cycle:                     nst = 600000
Number of initial calls to random number generator  rseed = 9858
Type of rand. number gen.
          (1 = lag. fib., 2 = lin. cong.)     rand_switch = 2
Compton refl. sentinel
       (0 = none, 1 = lower, 2 = outer, 3 = both) cr_sent = 0
Upper Boundary Reflection Sentinel
          (0 = none, 1 = refl. )               upper_sent = 0
Disk heating on (1) / off (0)                 dh_sentinel = 0
Pair processes on (1) / off (0)               pair_switch = 0
Constant temperature (electron spectrum)
          switch on (1) / off (0)                 T_const = 0
Coronal heating flare on (1) / off (0)        cf_sentinel = 0
Center of coronal heating flare, radius [cm]:     r_flare = 0.d0
Center of coronal heating flare, height [cm]:     z_flare = 0.d0
Center of coronal heating flare, time [s]:        t_flare = 0.d0
Radial width of flaring region [cm]:              sigma_r = 0.d0
Vertical width of flaring region [cm]:            sigma_z = 0.d0
Time width of flaring region [s]:                 sigma_t = 0.d0
Flare amplitude: (delta B / B_0)^2_max;
          (delta T_p)/T_p:                      flare_amp = 0.d0
```

The file first states the number of vertical radial zones. Then it gives the dimensions of the simulation region, in cm. It is possible to use the the upper boundary source to simulate a star, if the star_switch is set to 1. In this case, the rays from the upper source will be parallel (instead of randomly distributed over a solid angle of 2π), and one must specify the radius and distance to the star, in cm. TSTOP is the time, in that the simulation will stop, and DTMAX is the maximum possible time step (both in seconds). It is possible to specify different "time regions", where the boundary surface sources will vary. The number of these time regions is specified with NTIME. One then specifies what time, in seconds, a time region will begin or end. The boundary sources are a planck spectrum, the temperatures of which specified next, in keV. If the temperature is less than 0, then rather than using a planck spectrum, the code will read in the spectrum from a file. The file must be specified after the temperature.

While the code runs, it creates several output files: the spectrum and light curve of the escaped photons; and the temperature of zones, averaged vertically. If the SPEC_SWITCH is set to 1, however, instead of calculating the photons that escape, it will calculate the photons incident on the upper and lower boundaries, and use this as the spectrum file. The file next specifies the number and energy ranges of the bins for the spectrum file, followed by number of angular bins and the number of bins and energy ranges for the light curve files. Then the names of the energy spectrum, photon spectrum, light curve, census, and temperature files are given. The maximum number of photons the code will create in one time step is given next (NST). Note that the total number of photons in the simulation at one time cannot exceed ten times this number.

The file next specifies the seed for the random number generator, followed by a switch which tells it which random number generator to use (see § 2.4.1). Following this are switches that control reflection; CR_SENT controls the reflection of the lower boundary, while UPPER_SENT controls the reflection of the upper boundary. If CR_SENT is set to 1 there will be Compton reflection at the lower boundary of the simulation; if it is set to 2, it will be Compton reflected as if there is a disk extending beyond the simulation volume; if it is set to 3, it will reflect as both an inner and outer disk; if it is set to 4, there will be mirror reflection in the inner disk only; finally, if it is set to 0, there will be no reflection on the lower boundary. For the upper boundary, only mirror reflection is available. DH_SENTINEL controls whether the lower boundary will be heated by reflection off of it. Creation and destruction of electron-positron pairs can be turned on and off with the PAIR_SWITCH. T_CONST controls whether the electron distribution will remain a constant, or whether it will evolve with the Fokker-Planck calculation.

The rest of the parameters are regarding an increase in proton temperature (proton temperature usually being constant) somewhere in the simulation volume, in order to represent a coronal flare. The flare can be turned on or off with CF_SENTINEL. The central location of the flare in vertical, radial and time is specified next. The flare will take the shape of a Gaussian in the vertical, radial, and time direction; the σ Gaussian parameters for those dimensions are specified next. Finally, the magnitude of the flare is specified.

Each zone has its own input file, with a name based on the vertical and radial number of that zone. For example, the third vertical and fourth radial zone would have an input file named "input_03_04.dat". A sample of such a file is below:

```
1. Electron temperature in zone [keV]       tea = 1.000000e+02
2. Proton temperature in zone [keV]         tna = 2.348873e+04
3. Particle density in zone [cm^(-3)]       n_e = 8.041191e+18
4. Magn. field sent. (0 = spec.,
   1 = ep. w. el., 2 = ep. w. pr.)    ep_switch = 1
5. Magnetic field [G]                   B_field = 1.000000e+04
6. Maxwellian fraction in zone            amxwl = 1.000000e+00
7. Low-energy cut-off of nonthermal
   electron population:                    gmin = 1.000000e+00
8. High-energy cut-off of nonthermal
   electron population:                    gmax = 1.000000e+04
9. Non-thermal electron
   spectral index:                        p_nth = 2.500000e+00
10. Turbulence sp.index             q_turb(j,k) = 1.666667e+00
11. Turbulence Level
    (deltaB/B0)^2                turb_lev (j,k) = 1.000000e-20
```

For each zone, these files specifie the (initial) electron temperature, proton temperature, and electron density. The proton density is assumed to be the same as the electron density, although the electron density can vary over time if pair processes are turned on, as electrons and positrons can then be created and destroyed. The magnetic field can be calculated by assuming equipartition with the electrons or protons; or it can be specified in this file. The fraction of the electrons that are represented by a thermal distribution is specified with AMXWL; GMIN and GMAX specify the boundaries (in terms of γ) of the nonthermal distribution. P_NTH specifies the spectral index of the nonthermal distribution. Finally, the turbulence spectral index and the (time dependent) magnetic field fluctuations are specified. The parameters that can evolve with time, if the FP routine is used, are TEA, B_FIELD, (if electron equipartition is used), and AMXWL.

Appendix C

Photon Bubble Simulation Results

Here I list all the of the simulated spectra at all radii, and the total spectra for all of the simulations.

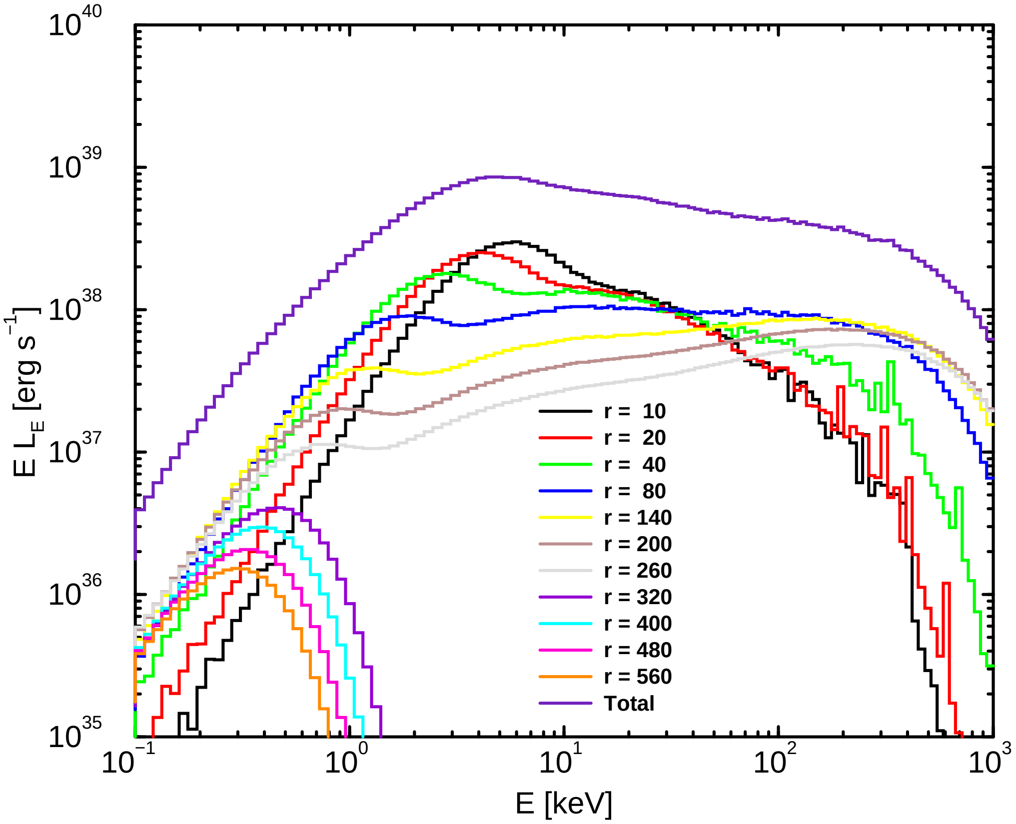

Figure C.1: The spectra at different radii and the total spectrum for Simulation 1 ($\dot{m} = 200$, $\alpha = 0.01$).

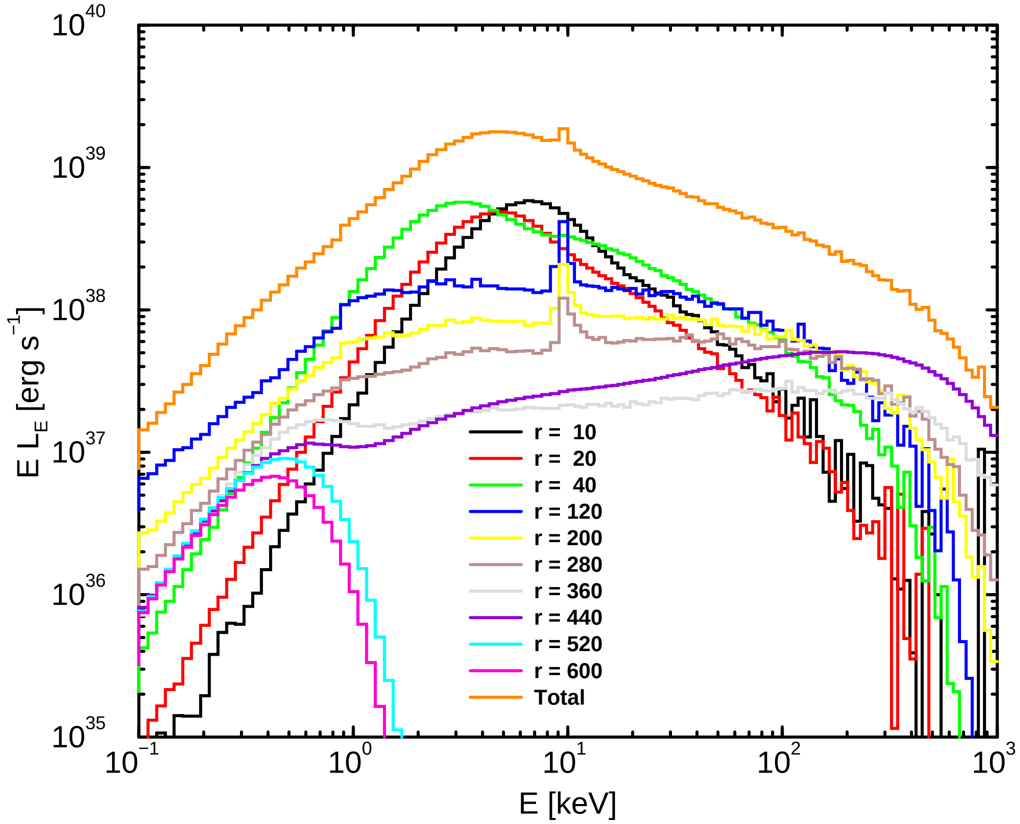

Figure C.2: The spectra at different radii and the total spectrum for Simulation 2 ($\dot{m} = 400$, $\alpha = 0.01$).

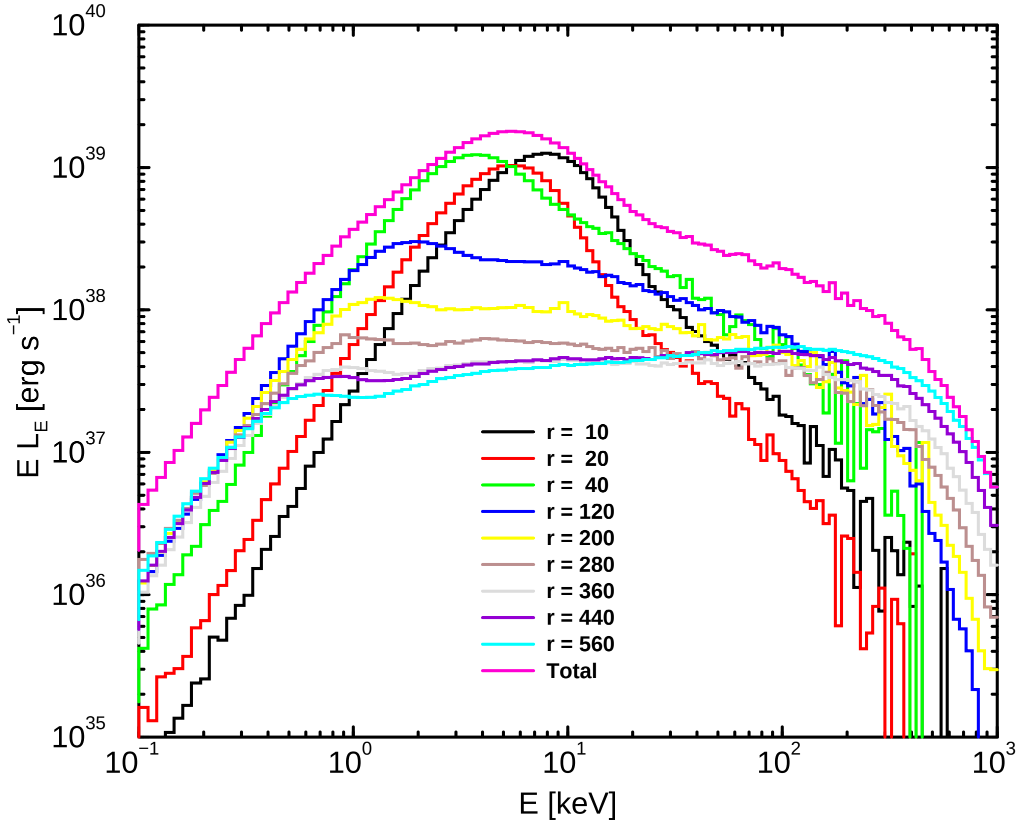

Figure C.3: The spectra at different radii and the total spectrum for Simulation 3 ($\dot{m} = 900$, $\alpha = 0.01$).

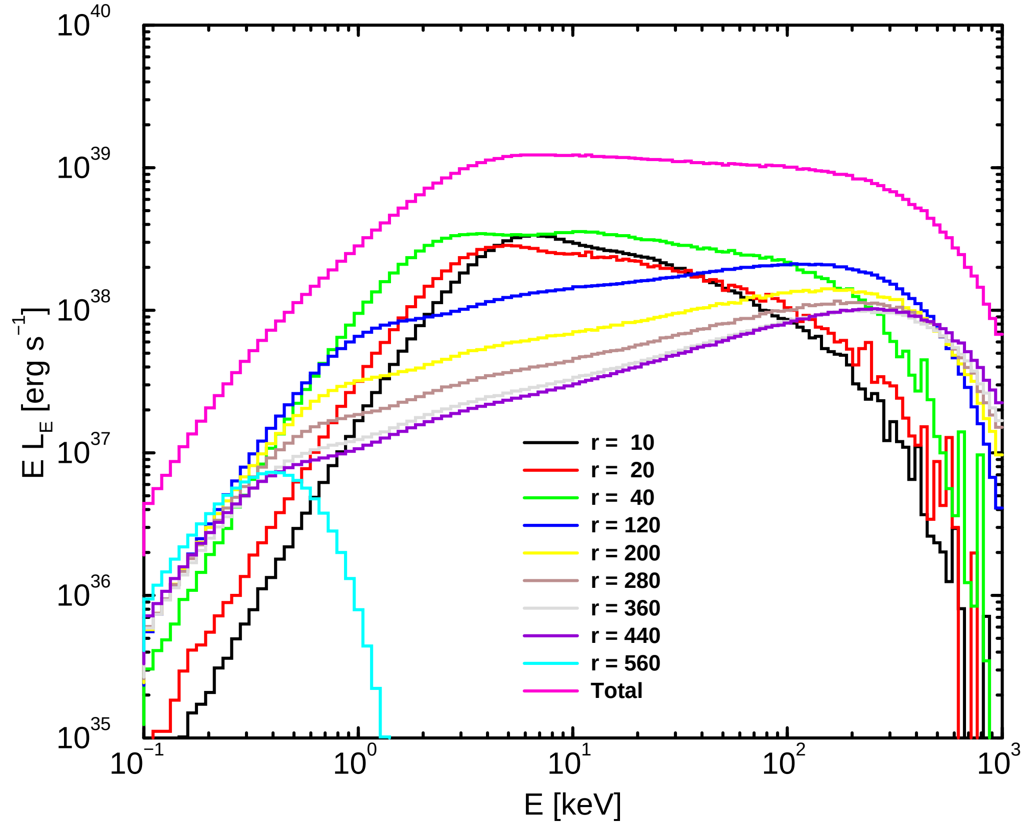

Figure C.4: The spectra at different radii and the total spectrum for Simulation 4 ($\dot{m} = 200$, $\alpha = 0.1$).

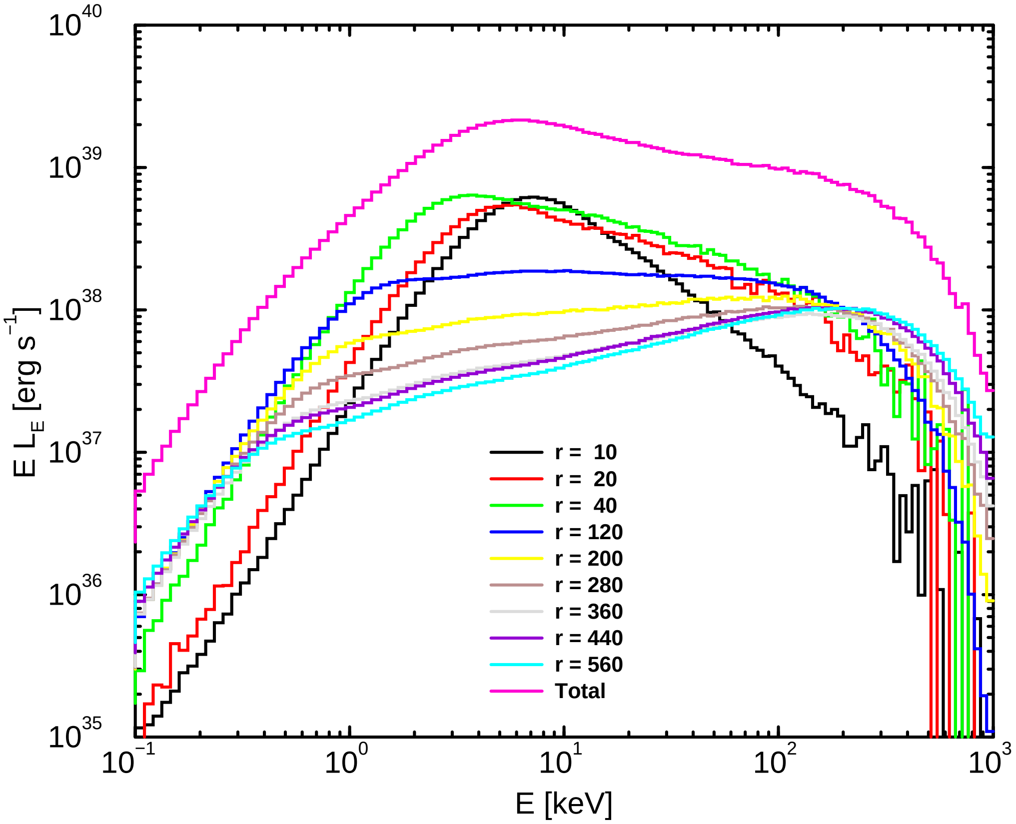

Figure C.5: The spectra at different radii and the total spectrum for Simulation 5 ($\dot{m} = 400$, $\alpha = 0.1$).

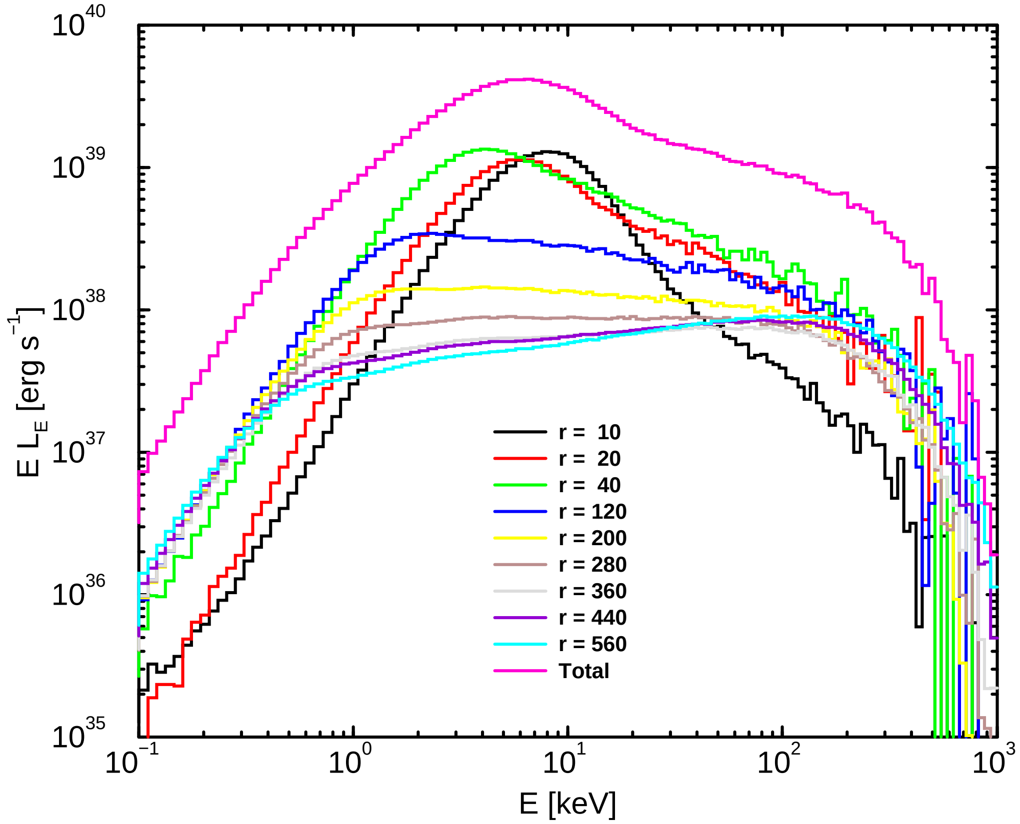

Figure C.6: The spectra at different radii and the total spectrum for Simulation 6 ($\dot{m} = 900$, $\alpha = 0.1$).

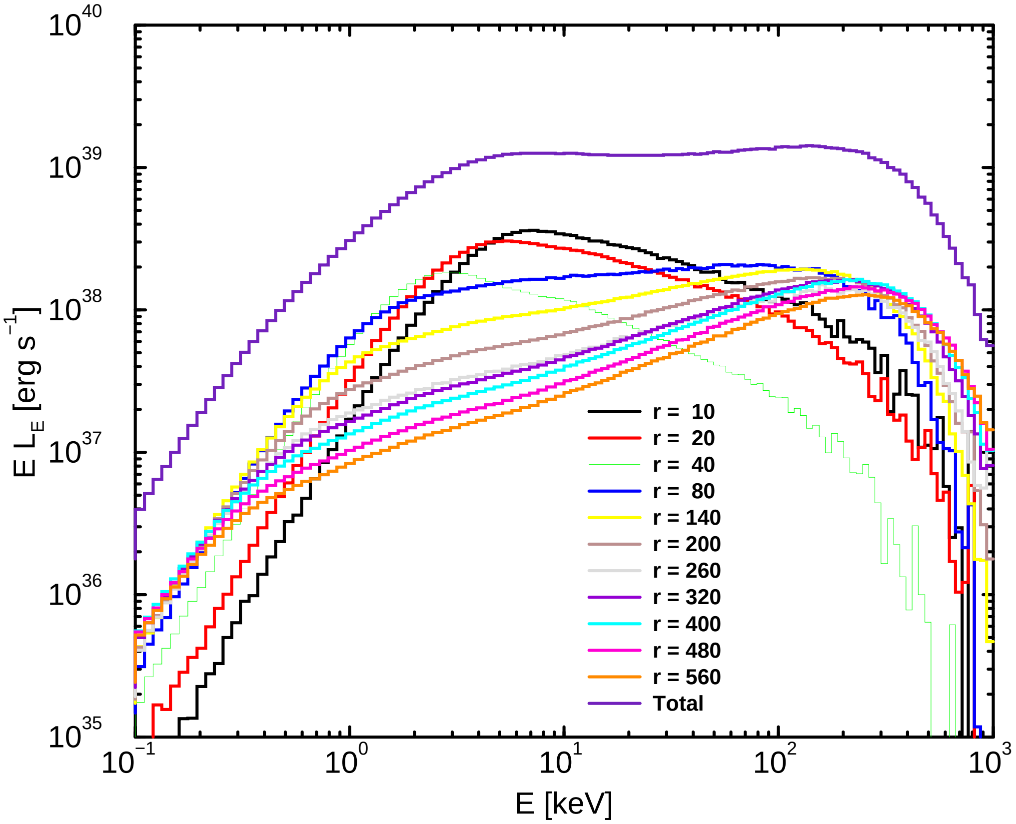

Figure C.7: The spectra at different radii and the total spectrum for Simulation 7 ($\dot{m} = 200$, $\alpha = 0.5$).

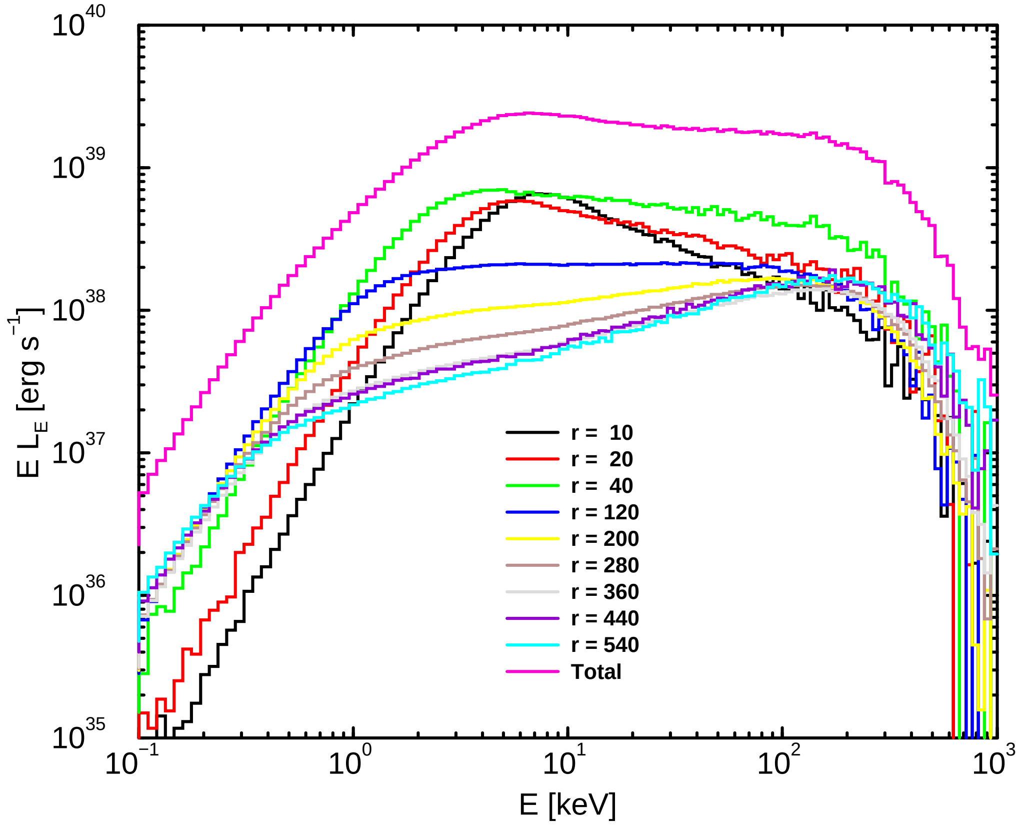

Figure C.8: The spectra at different radii and the total spectrum for Simulation 8 ($\dot{m} = 400$, $\alpha = 0.5$).

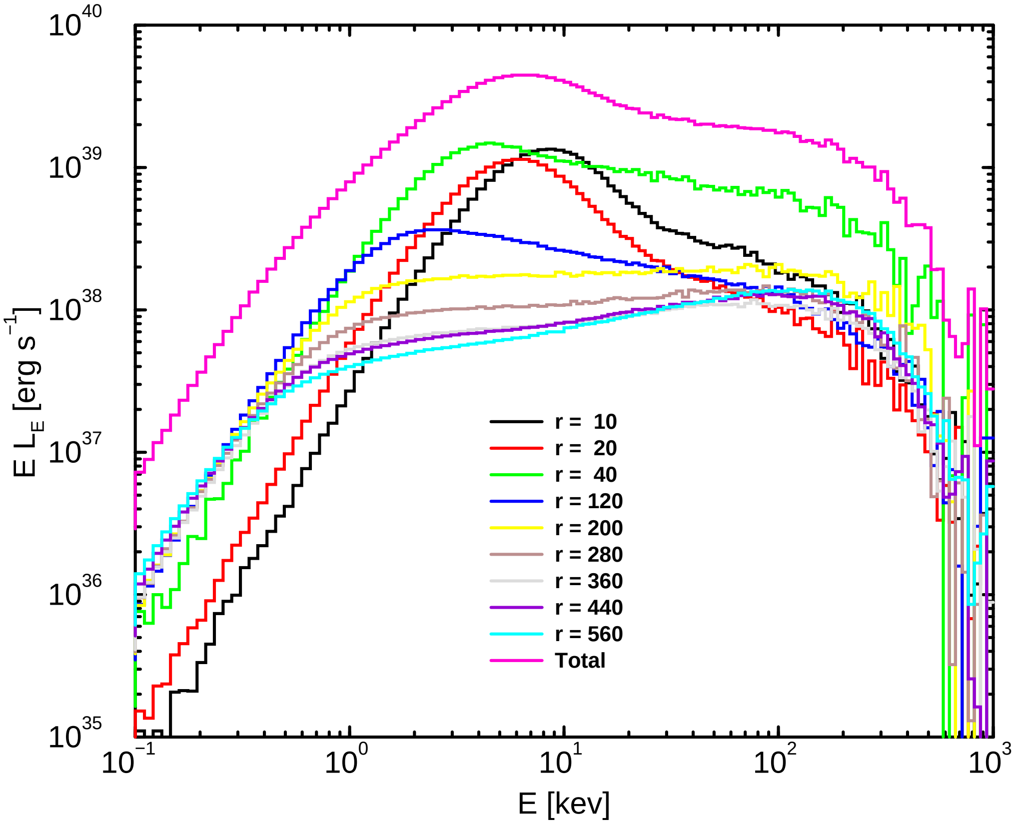

Figure C.9: The spectra at different radii and the total spectrum for Simulation 9 ($\dot{m} = 900$, $\alpha = 0.5$).